Radiation Monte Carlo approcah dedicated to the coupling with LES reactive simulation.

Jin Zhang

École Centrale Paris

THÈSE

présentée par

Jin ZHANG

pour l'obtention du

GRADE de DOCTEUR

Formation doctorale : **Energétique**

Laboratoire d'accueil : **Laboratoire d'Energétique Moléculaire et Macroscopique, Combustion (EM2C) du CNRS et de l'ECP**

Radiation Monte Carlo Approach dedicated to the coupling with LES reactive simulation

Soutenue le 31 Janvier 2011

Composition du jury :

M.	**Gokalp**	**I.**	**Président**
MMe.	**Eihafi**	**M.**	**Rapporteur**
M.	**Dupoirieux**	**F.**	**Rapporteur**
M.	**Gicquel**	**O.**	**Examinateur**
M.	**Veynante**	**D.**	**Examinateur**

Ecole Centrale des Arts et Manufactures
Grand Etablissement sous tutelle
du Ministère de l'Education Nationale
Grande Voie des Vignes
92295 CHATENAY MALABRY Cedex
Tél. : 33 (1) 41 13 10 00 (standard)
Télex : 634 991 F EC PARIS

Laboratoire d'Energétique Moléculaire et Macroscopique, Combustion (E.M2.C.)
UPR 288, CNRS et ...cole Centrale Paris
Tél. : 33 (1) 41 13 10 31
Télécopie : 33 (1) 47 02 80 35

2011 - 12

Acknowledgements

J'adresse tout à bord un très grand merci à Messieurs Olivier Gicquel et Denis Veynante, qui m'ont accueilli au laboratoire EM2C pour effectuer ces travaux présentés et m'ont encadré pendant ma thèse, pour m'avoir fait profiter leurs connaissances scientifiques et leurs méthodes de recherches, pour leurs patiences, leurs disponibilités, leurs conseils pertinents, et surtout leurs soutiens à la fin de ma thèse.

Je remercie vivement Monsieur Jean Taine, professeur de l'Ecole Centrale Paris, qui m'a fait bénéficier de ses riches connaissances en transfert radiatif.

Je tiens à remercier sincèrement Madame Mouna EI Hafi, professeur de l'École des Mines d'Albi Carmaux, du Centre Energétique - Environnement, ainsi que Monsieur Francis Dupoirieux, ingénieur de recherche à l'ONERA, qui ont accepté de juger ce travail et d'en être les rapporteurs. Je remercie également à Monsieur Iskender Gökalp, directeur du Laboratoire CNRS de combustion et systèmes réactifs (LCSR) d'Orléans, qui m'a fait l'honneur d'avoir été président de mon jury de thèse.

Je remercie particulièrement Monsieur Lionel Tessé, ingénieur de recherche à l'ONERA, qui m'a beaucoup aidé dans la compréhension du code ASTRE et l'interprétation du principe réciproque de la méthode Monte Carlo.

Je remercie également Monsieur Gilles Grausseau, chercheur de l'IDRIS, qui m'a aidé à résoudre les problèmes informatiques quand j'ai fait les calculs parallèles chez IDRIS.

Je souhaite aussi remercier à Rogério Gonçalves Dos Santos, docteur du laboratoire EM2C, ainsi que Kim Junhong, post-doc du laboratoire EM2C, avec qui j'ai travaillé sur le couplage combustion et rayonnement.

Je remercie à l'ensemble du personnel scientifique et administratif du laboratoire EM2C pour une très bonne ambiance.

Mes remerciements vont également à tous les thésards, docteurs et postdocs de notre laboratoire, pour les échanges fructueux que j'ai eus avec eux au cours de la thèse, spécialement pour Laetitia Pons, Jean-Michel Lamet, Nicolas Kahhali, Nicolas Tran et Yann Chalopin avec lesquels j'ai partagé le bureau.

Je souhaite enfin exprimer mes grands remerciements à mes parents qui ont toujours su me soutenir et m'encourager au cours de ma thèse.

Abstract

Radiative transfer plays an important role in turbulent combustion and should be incorporated in numerical simulations. However, as combustion and radiation are characterized by different time scales and different spatial and chemical treatments, and the complexity of the turbulent combustion flow, radiation effect is often neglected or roughly modelled. Coupling a large eddy simulation combustion solver and a radiation solver through a dedicated language CORBA is investigated. Four formulations of Monte Carlo method (Forward Method, Emission Reciprocity Method, Absorption Reciprocity Method and Optimized Reciprocity Method) employed to resolve RTE have been compared in a one-dimensional flame test case using three-dimensional calculation grids with absorbing and emitting medium in order to validate the Monte Carlo radiative solver and to choose the most efficient model for coupling. In order to improve the performance of Monte Carlo solver, two techniques have been developed. After that, a new code dedicated to adapt the coupling work has been proposed. Then results obtained using two different RTE solvers (Reciprocity Monte Carlo method and Discrete Ordinate Method) applied to a three-dimensional turbulent reacting flow stabilized downstream of a triangular flame holder with a correlated-k distribution model describing the real gas medium spectral radiative properties are compared not only in terms of physical behavior of the flame but also in computational performance (storage requirement, CPU time and parallelization efficiency). Finally, the impact of boundary conditions taking into account the actual wall emissivity and temperature has been discussed.

Résumé

Le transfert radiatif joue un rôle important en combustion turbulente et doit donc être pris en compte dans les simulations numériques. Toutefois, à cause du fait que la combustion et le rayonnement sont deux phénomènes physiques très différents caractérisés par des échelles de temps et d'espace également différentes, et la complexité des écoulements turbulents, l'effet du rayonnement est souvent négligé ou modélisé par des modèles très simples. Le couplage entre la combustion (LES) et le rayonnement avec l'environnement CORBA a été étudié. Dans le présent travail, quatre formulations de la méthode de Monte Carlo (méthode classique et méthode réciproque) dédiées à la résolution de l'équation de transfert radiatif ont été comparées sur un cas test de flamme 1D où l'on tient compte de l'absorption et de l'émission du milieu en utilisant un maillage 3D. Le but de ce cas test est de valider le solveur Monte Carlo et de choisir la méthode la plus efficace pour réaliser le couplage. Afin d'améliorer la performance du code de Monte Carlo, deux techniques ont été développées. De plus, un nouveau code dédié au couplage a été proposé. Ensuite, deux solveurs radiatifs (Emission Reciprocity Monte Carlo Method et Discrete Ordinate Method), appliqués à une flamme turbulente stabilisée en aval d'un dièdre avec un modèle CK de propriétés radiatives, sont comparés non seulement en termes de description physique de la flamme, mais aussi en terme de performances de calcul (stockage, temps CPU et efficacité de la parallélisation). Enfin, l'impact de la condition limite a été discuté en prenant en compte l'émissivité et la température de paroi.

Contents

Chapter 1

Introduction

Table of contents

1.1 Thesis background and application

From an environmental point of view, nowadays the air pollution problem becomes more and more serious and attracts the whole world's attention. As one of the main contributors of that, combustion processes are required to be better controlled to reduce the emission of the polluting products such as COx, NOx, soots etc. On the other hand, from an economical point of view, improving the combustion efficiency and performance is always the principal challenge that some related industries have to face, not only aeronautics but also for some energy industries. As a result of these two points, a high level knowledge about combustion processes and efficient tools to describe and resolve combustion systems as best as possible are then urgently required.

As combustion is a complex sequence which mixes chemical kinetics, thermodynamics and fluid dynamics, so its resolving and improvements need a better understanding and modeling of all the physical processes controlling a flame, such as turbulence, molecular physics and radiative heat transfer.

This thesis will be focused on the impact of the radiative heat transfer on turbulent combustion. The objective is to develop an efficient numerical tool of radiation simulation and to analyze the impact of the radiative heat transfer on turbulent combustion.

Reaction rates relevant to pollution products are known to be sensitive to the combustion temperature. So it is necessary to precisely estimate the local temperature, taking into account its fluctuations in the chemical kinetics calculations. Being a source term of the energy equation (volume radiative power), radiative heat transfer should be rigorously modeled to determine the temperature field with a high level of precision. The influence of the radiation on the combustion temperature and the polluted emission such as NOx and soots have been pointed out by some existing studies (De Lataillade 2001; Sivathanu and Gore 1994; Daguse 1996; Kaplan et al. 1994; Hall and Vranos 1994). Furthermore, radiative heat transfer plays a crucial role in the control of the charge heating in furnaces, in thermal heat losses and wall heat fluxes and in the control of the propagation of large scale fires. For example, Fig. 1.1, extracted from Goncalves Dos Santos et al. (2008), displaying a 2D flame structure and temperature (instantaneous field) and 1D cut temperature profiles from an average field, shows that on the one hand radiative heat transfer modifies the flame front structure with the maximum temperature decreased by heat losses and temperature gradients smoothed, and on the other hand the standard deviation is larger when radiation is taken into account which means that radiation modifies the flame dynamics. The experimental setup used for this test is detailed in Chapter 5.

However, the fact that combustion and radiative heat transfer are two phenomena physically different makes the coupling difficult. Usually combustion is focused on the balance

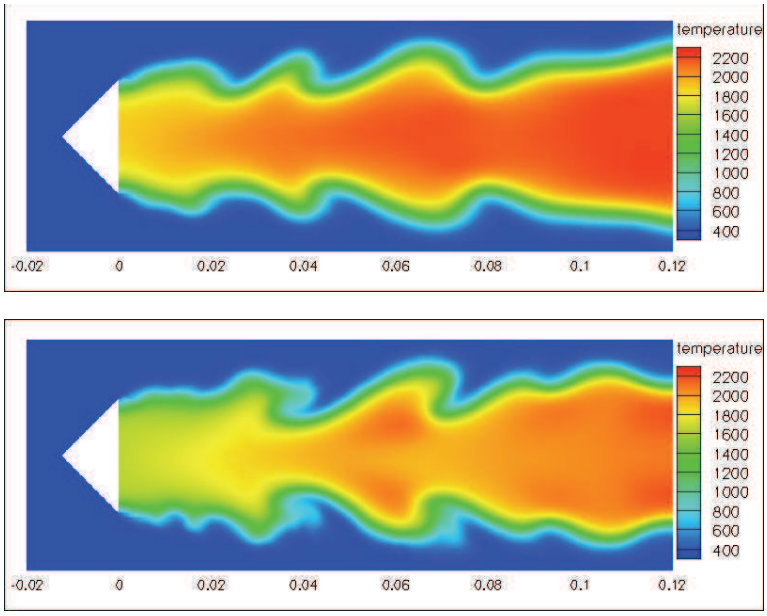

(a) Instantaneous resolved temperature fields without (top) and with (bottom) radiative heat transfer. Spatial coordinates are given in m

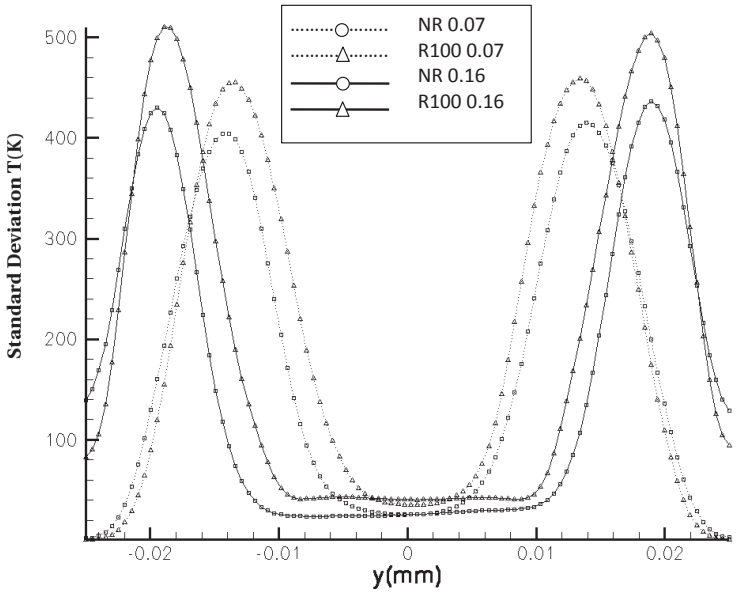

(b) Transverse profiles of the temperature standard deviation at two downstream locations from the flame holder $x = 7\ cm$ and $x = 16\ cm$ without (NR) and with (NR100) radiative heat transfer.

Figure 1.1 – *An example showing the influence of the radiation on the combustion temperature and the turbulent flame structure, a premixed propane/air flow is injected into a rectangular combustion chamber and a V-shape turbulent flame is stabilized behind the flame holder, the upstream mean velocity is about* $5m.s^{-1}$ *and the equivalence ratio* $\phi = 1$ *is chosen (Goncalves Dos Santos et al. 2008).*

over small volumes (finite volume framework) and radiative heat transfer involves long distances interaction as shown in Fig. 1.2. Therefore, two different numerical tools are

needed. Furthermore, solving Reynolds averaged Navier-Stokes (RANS) equations only

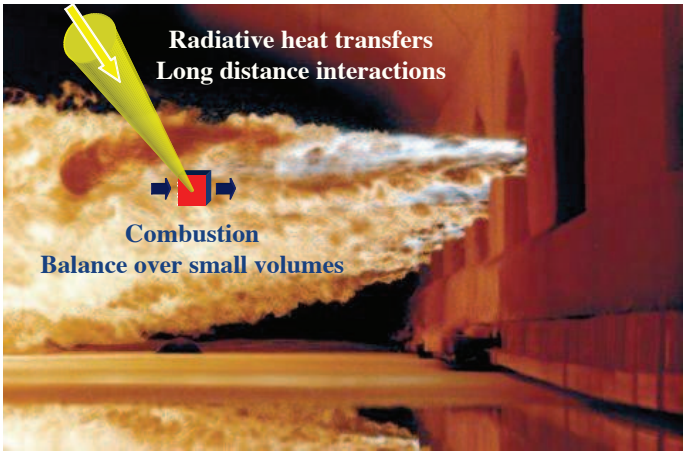

Figure 1.2 – *Different scales of combustion and radiation in their numerical simulations*

gives access to some mean quantities such as mean temperature or mean species fractions at a given location, although if the probability density functions (PDF) model describing one-point statistics is involved, the local fluctuations of temperature and composition may be modeled. But unfortunately, radiative heat transfer is controlled by the distribution of cold and hot gases along optical paths, and radiative power is highly nonlinear and varies directly with the fourth power of the local instantaneous temperature, which requires information on spatial correlations usually not available in RANS. Then other Navier-Stokes solving methods which asks for more CPU time like LES or DNS should be applied here. On the other hand, most of the radiative transfer equation resolution approaches such as Ray-tracing technique, Discrete Ordinate Method and Monte Carlo Simulation are always very expensive in terms of CPU time requirement and memory storage. Consequently, the challenge is to find a compromise between taking into account the radiative heat transfer as precisely as possible and reducing the computational requirement in terms of CPU time and memory.

After referring to some existing researches about combustion numerical simulations including radiation and other physical phenomena such as turbulence and chemistry with different levels of simplifications and assumptions because of limited computational resources (bibliography being presented in Section. 2.2.2), a numerical approach developed in the Phd. thesis of Goncalves Dos Santos (2008) will be used here to couple turbulent combustion and radiative heat transfer considering the turbulence/radiation interaction (TRI), non-gray medium with detailed radiative gases properties modeled and "industrial" configurations (three dimensional heavy mesh), furthermore taking into account the computational resources limits. This approach is based on two independent solvers linked through a specialized framework, CORBA - Common Object Request Broker Architecture (Henning and Vinoski 1999), dedicated to couple two solvers and taking advantages of different characteristic time of each phenomenon. Fig. 1.3 displays the coupling principe:

- CORBA allows construction of applications constituted of software modules that exchange information over a network. It works through internet protocols and distant machines or/and different platforms can be used.
- A client / server ideology is retained: the combustion code (client) asks for informa-

tion (radiative flux and energy source terms) and the radiation code (server) sends the information back. Then the combustion code also sends its output data (thermodynamic data such as temperature and mass fraction) to the radiation code.

- The combustion code used here is AVBP code and the radiation code can be Discrete Ordinate Method (DOM) code or Monte Carlo Method code.

By using this tool, Goncalves Dos Santos has coupled a LES solver AVBP developed by CERFACS and IFP (Schoenfeld 2008) with a three-dimensional discrete ordinate method (DOM) solver (Goncalves Dos Santos 2008).

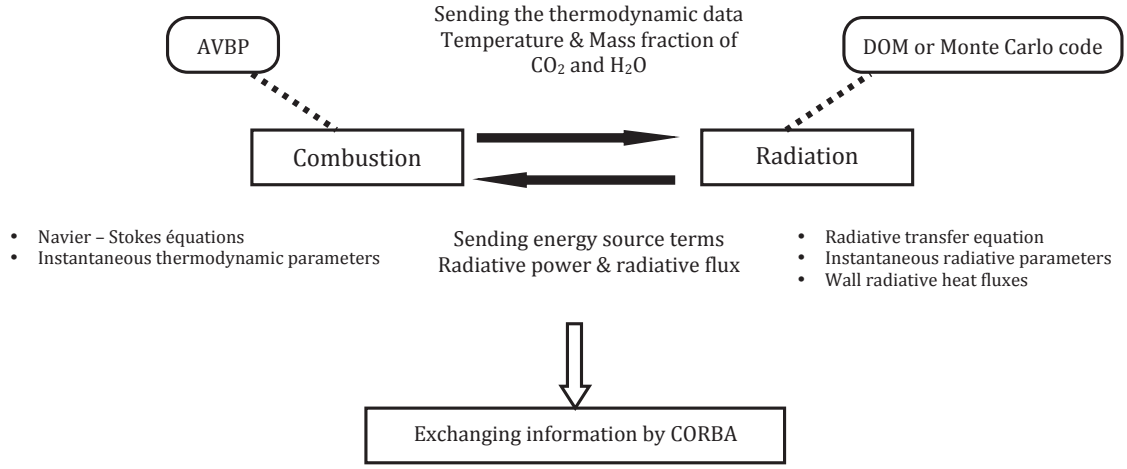

Figure 1.3 – *Coupling principe between two parallel solvers dedicated to turbulent combustion (AVBP) and radiative heat transfer (DOM or Monte Carlo Method) by using CORBA framework*

In the precedent paragraph, the numerical coupling tool (CORBA) has been described. In this part, the two numerical solvers respectively for turbulent combustion and radiation will be briefly presented. On the one hand, a stochastic Monte Carlo method is used to solve radiative transfer. Compared with deterministic methods such as DOM, SHM - Spherical Harmonics Method (Mazumder and Modest 1999), Monte Carlo does not need some simplifying assumptions, i.e. optically thin fluctuation assumption (OTFA) and gas radiative properties assumptions (i.e. reducing the spectral bands number). Therefore, a much more precise result will be obtained with Monte Carlo. More details about the advantages of this method will be presented in Chapter 3.3.3. On the other hand, AVBP code is retained as the LES solver.

In the first part of this thesis, a code called ASTRE (Approche Statistiques des Transferts Radiatifs dans les Ecoulements), developed by Tessé during his Phd. thesis (Tesse 2001), is used here as Monte Carlo solver. ASTRE can deal with complex three-dimensional geometries taking into account the non-isothermal and heterogeneous non-gray medium, a detailed spectral discretization of the radiative gases properties and a diverse direction presentation of the particles, turbulence/radiation interaction and radiative non-isotope diffusion of the particles. Furthermore, this code uses three reciprocal Monte Carlo formulations and one forward Monte Carlo formulation at the same time (Tesse et al. 2002). The first task of this thesis is to compare these four formulations on a one-dimensional flame application to

find the most suitable formulation for coupling in terms of the precision and computational requirements.

After several tests, we found that when ASTRE code is applied to a complex geometry (i.e. a mesh with 3.4 million cells), if a detailed radiative gases properties model is needed (i.e. Correlated-k model with 1022 spectral bands), the memory storage required might become very huge (detailed figure will be presented in Chapter 4) and might not be acceptable by usual scientific computers. As a result of that, two techniques have been developed to improve the performance of ASTRE code in terms of computational CPU time and storage requirements to facilitate the coupling work when applied to a complex real industrial geometry and taking into account a detailed radiative gases properties such as correlated-k model. Then, a new parallel code based on ASTRE and dedicated only to the coupling with turbulent combustion has been developed. It can be considered as a subroutine of ASTRE which is easier to be coupled with other codes.

Boundary conditions are often simplified in radiation/combustion interaction problems. But in fact, their influence on wall radiative fluxes and radiative power in the medium cannot be neglected. So the impact of boundary conditions will be discussed at the end of this thesis taking into account the effects of actual wall emissivity, temperature and convection phenomena.

1.2 Thesis structure

This manuscript emphasizes the specific problems linked to the development of an efficient Monte Carlo solver, requiring less computational resources and to be applied easily to industrial configurations, for Large Eddy Simulation of turbulent combustion including radiative heat transfer. The scope of this thesis is listed below:

- **Chapter 2**: Basic presentation and comparison of different turbulent combustion modeling methods, explaining LES model is chosen for this work and presentation of turbulent combustion solver being used here - AVBP code.
- **Chapter 3**: Basic concepts of radiative heat transfer and a brief presentation about the different methods for radiative transfer equation resolution, particularly focused on the Monte Carlo method and explaining its advantages, finally emphasizing the Monte Carlo numerical scheme being used in this thesis.
- **Chapter 4**: Emission Reciprocal Monte Carlo Method (ERM) has been validated applied on a 1D flame by using ASTRE and chosen as the most suitable model for coupling. Two techniques have been developed to improve the performance of ASTRE code, which are respectively "Grid merge" method and "near/far-range-interaction" model. Finally, a new code only using ERM model dedicated to the coupling had been developed from ASTRE.
- **Chapter 5**: Discrete Ordinate Method (DOM) and Monte Carlo Method applied to a three-dimentional flame have been compared in terms of physical behavior and computational performances.
- **Chapter 6**: The influence of boundary conditions has been discussed taking into account the impact of wall emissivities and wall convection phenomena.

Chapter 2

Numerical simulation of turbulent combustion

Table of contents

In this chapter, the basic balance equations used in turbulent combustion studies are firstly introduced, then a comparison between the different numerical methods is presented to evidence the choice of LES method for the study. Finally, the numerical tool - AVBP - used here is briefly described.

2.1 Conservation equations of turbulent combustion

The basic instantaneous local balance equations to describe combustion can be summarized using the classical lettering as below (Barrere and Prud'homme 1973; Williams 1985; Kuo 1986; Poinsot and Veynante 2005):

Mass conservation (j=1,2,3):

$$\frac{\partial \rho}{\partial t} + \frac{\partial \rho u_j}{\partial x_j} = 0 \tag{2.1}$$

where ρ is the density of the mixture, u_j is the j component of the velocity vector u.

Momentum conservation (i=1,2,3):

$$\frac{\partial \rho u_i}{\partial t} + \frac{\partial \rho u_j u_i}{\partial x_j} = -\frac{\partial p}{\partial x_i} + \frac{\partial \tau_{ij}}{\partial x_j} + F_i \tag{2.2}$$

where τ_{ij} is the viscous tensor and F_i is a body force (such as gravity, etc). For Newtonian fluids, according to the Newton law, the viscous tensor is written as:

$$\tau_{ij} = \mu_l \left(\frac{\partial u_i}{\partial x_j} + \frac{\partial u_j}{\partial x_i} \right) - \frac{2}{3} \mu_l \delta_{ij} \left(\frac{\partial u_k}{\partial x_k} \right) \tag{2.3}$$

where μ_l is the shear viscosity and δ_{ij} is the Kronecker symbol.

Species conservation (N species with $k = 1, \cdots, N$):

$$\frac{\partial \rho Y_k}{\partial t} + \frac{\partial \rho u_j Y_k}{\partial x_j} = -\frac{\partial J_j^k}{\partial x_i} + \dot{\omega_k} \tag{2.4}$$

where J_j^k is the molecular diffusive flux of species k in direction j and $\dot{\omega_k}$ is the mass reaction rate of the species k per unit volume. These species molecular diffusivities J_j^k can be described using the Fick's law as:

$$J_j^k = -\frac{\mu_l}{Sc_k} \frac{\partial Y_k}{\partial x_j} \tag{2.5}$$

where Sc_k, the Schmidt number of the species k, is defined as:

$$Sc_k = \frac{\mu_l}{\rho D_k} \tag{2.6}$$

D_k is the molecular diffusivity of the species k relatively to the major species.

Total enthalpy ($h_t = h + u_i u_i/2$)

$$\frac{\partial \rho h_t}{\partial t} + \frac{\partial \rho u_j h_t}{\partial x_j} = \frac{\partial p}{\partial t} + \frac{\partial}{\partial x_j}(J_j^h + u_i \tau_{ij}) + u_j F_j \tag{2.7}$$

where $u_i \tau_{ij}$ and $u_j F_j$ are respectively the power due to the viscous and body forces. The enthalpy diffusion J_j^h can be described as:

$$J_j^h = -\frac{\mu_l}{Pr}\left[\frac{\partial h}{\partial x_j} + \sum_{k=1}^{n}\left(\frac{P_r}{Sc_k} - 1\right) h_k \frac{\partial Y_k}{\partial x_j}\right] + Q_r \tag{2.8}$$

The Prandtl number P_r contains the diffusive transport of the momentum and temperature. In this expression, the Dufour effect (enthalpy diffusion under mass fraction gradients) is neglected. The Lewis number Le_k of the species k representing the ratio between the thermal and mass diffusivities can be introduced as:

$$Le_k = \frac{Sc_k}{P_r} \tag{2.9}$$

Q_r is the radiative power, it can be neglected or estimated from simplified radiative models. Another possibility is to be calculated by a dedicated radiative solver using more accurate models as in the present thesis.

2.2 Choosing LES among different numerical approaches of turbulent combustion

In this section, three numerical methods used to resolve the turbulent combustion problems are firstly introduced and compared. Then references focusing on the combining turbulent combustion and radiation studies are discussed. Based on the two previous parts, finally combustion solver with LES model is chosen to be used for this thesis.

2.2.1 Comparison of three turbulent numerical methods

In order to solve the balance equations mentioned above, some numerical methods have been developed. The principle of three turbulent numerical methods can be illustrated by the turbulent kinetic energy spectrum in figure 2.1.

Direct Numerical Simulation (DNS) offers the full numerical solution of the instantaneous balance equations for all of the spatial frequencies in the spectrum. All turbulence scales are explicitly determined without any model for turbulent motions (Poinsot and Veynante 2005). However, limited by the computational performance, this method can only be used

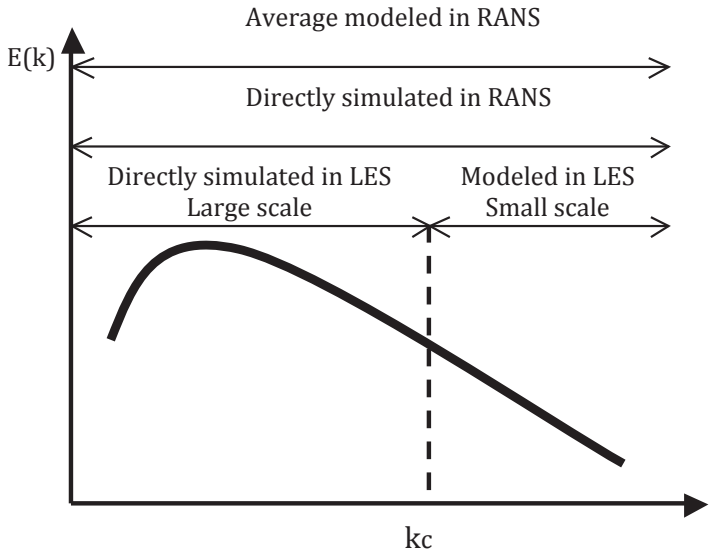

Figure 2.1 – *Turbulence kinetic energy spectrum plotted as a function of the inverse length scale (proportional to the wave number). RANS, LES and DNS are summarized in terms of spatial frequency ranges*

for some very simplified cases (Poinsot 1996; Poinsot et al. 1996; Vervisch and Poinsot 1998), where time and length scale ranges present in the flow are very limited (small Reynolds numbers).

Reynolds-average Navier-Stokes (RANS) methods describe the mean flow field by averaging the balance equations. The local fluctuations and turbulent structures are integrated and presented as mean quantities form (such as mean temperature, mean mass fraction of CO_2 and H_2O) directly linked to the probability to find hot burnt gases at a given location (Poinsot and Veynante 2005). So the averaging operator in RANS is "temporal" (average in time) not "spatial". However, for combining turbulent combustion and radiation studies, radiative transfer is controlled by the instantaneous distribution of cold and hot gases along optical paths which can not be directly extracted from mean flow characteristics. Probability density functions (PDF) may be introduced to overcome this problem, but PDF based methods can hardly take into account the spatial correlations which is crucial in radiative transfer. This turbulence-radiation interaction problem has been addressed by several authors (Giordano and Lentini 2001; Coelho et al. 2003; Li and Modest 2003).

Large Eddy Simulation (LES) resolves explicitly the large flow structures (a cut-off scale is needed here, it can be chosen as the computational mesh size in some practical cases) and the effects of the structures smaller than the cut-off length scale are modeled. The major difference between RANS and LES comes from the operator employed in the derivation (Goncalves Dos Santos 2008). As mentioned in the previous paragraph, in RANS, the averaging operator is applied over a set of realizations during a time scale. In LES, the operator is a spatial filter localized at a given size Δ, which is independent on time and applied to a single realization of the studied flow. So in the combining radiation and combustion studies, Large Eddy Simulation (LES) can give access to the instantaneous spatial distribution of fresh and burnt gases at the resolved scale levels (DNS also has this advantage).

A few words about LES equations. In LES, the quantities Q are filtered in the spectral space (cut-off filter) or in the physical space (weighted average in a given volume, box filter or Gaussian filter),the filter operation is defined as:

$$\bar{Q}(x) = \int Q(x^*)F(x - x^*)dx^* \tag{2.10}$$

where F is the LES filter:

$$\int F(x)dx = 1 \tag{2.11}$$

In reactive flows, a mass-weighted Favre filtering is introduced as (Poinsot and Veynante 2005):

$$\bar{\rho}\tilde{Q}(x) = \int \rho Q(x^*)F(x - x^*)dx^* \tag{2.12}$$

Then the instantaneous balance equations in Chapter 2.1 can be filtered to derived balance equations for the filtered quantities $\bar{Q}$ or $\tilde{Q}$. Furthermore, any quantity Q may be decomposed into a filtered component $\bar{Q}$ and a "fluctuating" component Q' written as:

$$Q = \bar{Q} + Q' \tag{2.13}$$

where Q' represents the instantaneous fluctuations relative to the resolved field. More details about the LES filtered balance equations can be found in Poinsot and Veynante (2005).

2.2.2 Bibliography for combining combustion and radiation study

In combining combustion and radiation study domain, some researches have been realized.

Laminar flame

Some studies focus on the laminar flame or neglect the effects of turbulent fluctuations for turbulent flame in order to understand the interactions between radiation and chemistry in combustion. De Lataillade (2001) has calculated a 1D counter flow laminar diffusion flame of methane by using a radiative Monte Carlo method with soot particles and radiative gases properties modeled by a statistical narrow band model formulated in k-distribution. Sivathanu and Gore (1994) have pointed out the strong coupling between soot formation and radiation in laminar acetylene diffusion flames by a ray-tracing radiative method with gray soot particles assumption. Liu et al. (2004) have performed a detailed calculation of an axisymmetric coflow laminar methane/air diffusion flame by using the Discrete Ordinate Method (DOM) and different implementations of the SNBCK-based band models with detailed gas-phase chemistry and soot modeled by an acetylene-based semi-empirical two-equation model. Zhu and Gore (2005) have simulated a one-dimension opposed-flow laminar methane/air diffusion flames with detailed gas chemistry and global soot kinetics using the Sandia OPPDIF code.

Turbulent flame

In turbulent flames, turbulence/radiation interactions, called TRI has to be considered. TRI arises from highly nonlinear coupling between temperature and composition fluctuations in both non-reacting and reacting turbulent flows. Faeth and Gore have concluded that TRI effect on the radiative transfer is very important (about 50-300% of the value without TRI effect), especially in turbulent diffusion flame of ethylene, acetylene and hydrogen (Gore et al. 1987; Gore and Faeth 1988; Kounalakis et al. 1988). As mentioned in precedent section, RANS modeling approaches are not well suited to dealing with TRI, then statistical approaches such as probability density function (PDF) methods are needed (Coelho et al. 2003; Li and Modest 2002). Adams and Smith (1995) have used a Discrete Ordinate Method (DOM) associated with the optically thin fluctuation assumption (OTFA or called self-absorption neglected) in an industrial furnace, assumed to be a gray medium. And the fluctuations of the thermo-physical properties have been deduced from a 2D PDF of the mixture ratio and of the total enthalpy.

DNS was combined with DOM (Discrete Ordinate Method) to investigate two dimension sooting flames for fires (Yoo et al. 2005). Wu et al. (2005) have implemented a photon Monte Carlo method for the solution of the radiative transfer equation in a turbulent combustion DNS code to study the turbulence-radiation interaction. However DNS computations still remain out of reach of practical industrial configurations in terms of CPU cost. Then LES appears as a very efficient alternative tool to deal with turbulent combustion radiation interaction. Indeed this approach can be expected to provide a more accurate representation of one-point statistics and spatial correlations, a key point when dealing with radiation. The combination of LES and DOM has been performed by several authors including the consideration of soot formation and radiation (Desjardin and Frankel 1999; Jones and Paul 2005). Additionally, Gonçalves Dos Sandos has performed a simulation coupling LES and DOM solvers through a specialized framework CORBA (Goncalves Dos Santos 2008; Goncalves Dos Santos et al. 2008). His results will be used later on in this thesis.

To conclude, combining work of turbulent combustion solvers (DNS, RANS, LES) and radiative transfer solvers (DOM, Monte Carlo, etc.) has been widely performed by using different combination couple. However, due to the computational resource limit, The coupling work between LES and Monte Carlo, which can give a satisfying results in terms of precision, has not been really realized, especially for the complex configurations. That is the reason why this thesis will focus on this coupling and show its feasibility.

2.3 AVBP code

2.3.1 Introduction

The LES solver used in this work is AVBP code (Selle et al. 2004) developed by CERFACS and IFP and dedicated to compute reactive flows. It can resolve three dimensional compressible equations on structured and unstructured meshes. This solver is based on the finite volume or finite element methods with artificial viscosity sensor and explicit time integration.

The numerical schemes implemented "Lax-Wendroff scheme" (Hirsch 1989) is used for this thesis. It uses a second order Runge-Kutta time integration and central second order

spatial discretization. Compared with the other scheme of AVBP - TTGC scheme (Colin and Rudgyard 2000), Lax-Wendroff scheme is more feasible to be used for reacting flows and runs almost two times faster.

The NSCBC (Poinsot and Lele 1992) and wall law boundary conditions (Schmitt 2005) are used here. This code is parallelized by domain splitting using MPI library, a convenient approach for small volumes solving.

Finally, one of the reasons to choose this code for coupling is that its efficiency well adapted to the massive computation.

2.3.2 Thickened Flame model for LES

A difficult problem encountered for Large Eddy Simulation of premixed flames is that the thickness $\delta_L^0$of a premixed flame (usually between 0.1 mm to 1 mm) is generally smaller than the standard computational mesh size Δ used for LES. Therefore, some models should be applied to resolve the flame fronts on a LES mesh (Poinsot and Veynante 2005).

The Thickened Flame model (TFLES) is used in this thesis to describe the premixed combustion. In this model, an artificial factor F has been introduced to thicken the flame front in order to resolve the front structure on LES numerical mesh. It is shown that multiplying species and heat diffusion coefficients by a factor F (i.e. the molecular diffusivity of the species D becomes FD) and decreasing the exponential constant by the same factor F (A is replaced by A/F, where A is the exponential constant for the reaction rate $\dot{\omega}$) provides a flame propagating at the same laminar flame speed as the non-thickened flame, with its thickness increasing as $F\delta_l^0$ (Butler and O'Rourke 1977; Colin et al. 2000).

Additionally, this factor F will change the Damkohler number D_a which characterizes the ratio between the turbulent (τ_t) and the chemical (τ_c) time scales:

$$D_a = \frac{\tau_t}{\tau_c} \tag{2.14}$$

the turbulent scale can be estimated from turbulent integral scale characteristics ($\tau_t = l_t/u'$, where l_t is the turbulence integral length scale and u' is the velocity fluctuation related to the square root of the turbulent kinetic energy) and the chemical time scale τ_c may be estimated as the ratio of the thickness δ_L and the propagation speed S_L of the laminar flame. So the Damkohler number D_a becomes:

$$D_a = \frac{\tau_t}{\tau_c} = \frac{l_t}{\delta_L}\frac{S_L}{u'} \tag{2.15}$$

If the thickness δ is multiplied by the factor F, D_a will be divided by F. This low Damkohler number corresponds to a slow chemical reaction. Reactants and products are mixed by turbulent structures before reaction (Poinsot and Veynante 2005). This point might impact the results of coupling work between combustion and radiation.

Later in the chapter 4, the impact of TFLES model with different artificial factors on the radiative results will be discussed.

Chapter 3

Numerical simulation of radiative heat transfer

Table of contents

3.1 Some basic concepts of radiative transfer applied in the turbulent combustion

A flame is a medium that can absorb, emit and scatter radiation to transfer energy, and may also contain solid or liquid particles. Two difficulties could arise in studying radiation problems in combusting medium. Firstly, absorption, emission and scattering of energy occur not only at system boundaries, but at all locations in the medium. Then the temperature, radiation intensity and physical properties at every point will be required to describe energy exchanges in detail. The second difficulty is that spectral effects are often much more pronounced in gases than for solid surfaces, and a detailed spectrally dependent analysis may be required.

In this chapter, firstly, some fundamental concepts are introduced for radiant intensity within a medium, and for the effects of absorption, emission, and scattering on radiant propagation. Then the radiative transfer equation is formulated and some of its solution methods are described briefly. Finally, Monte Carlo method is detailed, together with the numerical scheme used in this thesis.

3.1.1 Radiation monochromatic intensity

The radiation monochromatic intensity $L_\nu(\vec{r},\vec{\Delta})$ $(W \cdot m^{-2} \cdot sr^{-1} \cdot Hz^{-1})$ is introduced in problems dealing with radiative transfer through absorbing, emitting and scattering medium. It can be defined as the radiation energy crossing through an area per unit time dt, per unit surface dS, per unit solid angle $d\Omega$ for the spectral frequency ν (Modest 2003; Taine et al. 2003):

$$L_\nu(\vec{r},\vec{\Delta}) = \frac{d^5\Phi_\nu(\vec{r},\vec{\Delta})}{d\Omega[dS \cdot (\vec{\Delta}\cdot\vec{n})]d\nu} \tag{3.1}$$

where $d^5\Phi_\nu(\vec{r},\vec{\Delta})$ is the monochromatic energy flux (Watts) from a point of the space $P(\vec{r})$, crossing the surface dS ($\vec{n}$ is the normal direction of the surface dS and $\vec{\Delta}$ is the radiative ray direction) in a solid angle $d\Omega$, see Fig. 3.1.
To resolve the radiative transfer problem is then to determine the radiative monochromatic intensity. In consequence, a radiative transfer equation should be established for a given optical path and a given frequency (Tesse 2001).

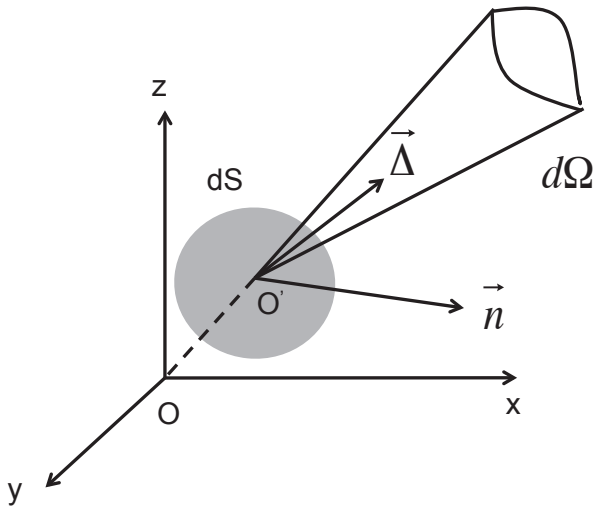

Figure 3.1 – *Radiative intensity*

3.1.2 Energy attenuation by absorption and out-scattering

An optical beam carrying the spectral radiation intensity L'_ν crosses a participating medium of thickness ds as shown in Fig. 3.2, the energy absorbed and scattered by this medium $d^6\Phi'^{a,s-}_\nu(s)$[1] depends on the magnitude of the incident intensity L'_ν, the optical path distance ds and an extinction coefficient β_ν of the medium which is a function of the temperature, pressure, frequency of the incident radiation and characteristics of the medium.

$$d^6\Phi'^{a,s-}_\nu(s) = -\beta_\nu L'_\nu dS ds d\Omega d\nu \tag{3.2}$$

and the extinction coefficient can be represented as:

$$\beta_\nu = \kappa_\nu + \sigma_\nu \tag{3.3}$$

where κ_ν ($\sim m^{-1}$) and σ_ν ($\sim m^{-1}$) are respectively the **absorption** coefficient and the **scattering** coefficient.

Absorption

Considering only the energy attenuated by the absorption, Eq. 3.2 can be written as an integration form over a optical path $s = l$:

$$d^5\Phi'^a_\nu(l) = \exp\left(-\int_0^l \kappa_\nu \mathrm{d}s\right) \cdot d^5\Phi'_\nu(0) \tag{3.4}$$

where $d^5\Phi'_\nu(0)$ is the incident flux at $s = 0$ and $\delta_\nu = \int_0^l \kappa_\nu \mathrm{d}s$ is the **optical thickness** (for the absorption) of the layer of thickness l and is a function of all the values of κ_ν between 0 and l. If $\delta_\nu \gg 1$, the medium is called **optically thick**, which means the mean penetration distance is quite small compared to the characteristic dimension of the medium. For this condition, the thermal energy can be completely absorbed in a short distance, and a volume element within the material is only influenced by the surrounding neighboring elements. If $\delta_\nu \ll 1$, the medium is then called **optically thin**, which means that the

[1]Here $'$ represents a given direction Δ.

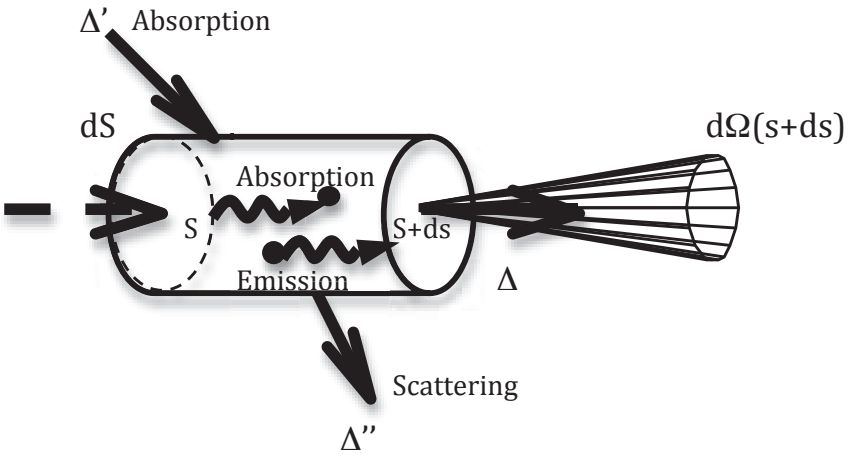

Figure 3.2 – *Radiative energy evolution along an optical path*

mean penetration distance is much larger than the medium dimension. Radiation travels entirely through the material without significant absorption and each element within the medium interacts directly with the medium boundary (Siegel and Howell 1981). In this thesis, without specific comments, the medium will be implicitly considered as "optically thin".

Out-Scattering

The radiation scattering represents the optical path deviation because of the interaction between a photon and another or more other particles during which the photon does not lose its entire energy. If the energy is attenuated by scattering, it will be called "out-scattering". Similar to the absorption, it can be written as:

$$d^5\Phi_\nu'^{s-}(l) = \exp\left(-\int_0^l \sigma_\nu \mathrm{d}s\right) \cdot d^5\Phi_\nu'(0) \tag{3.5}$$

3.1.3 Energy gain by emission and in-scattering

Emission

To maintain the local thermodynamic equilibrium in the computational domain (ex: the volume from S to $S + ds$ presented in Fig. 3.2), all of the medium absorbing an amount of energy can emit at the same time. $d^6\Phi_\nu'^e(s)$ representing the amount of energy emitted over a certain path s that escapes into a given direction can be written as (Taine et al. 2003):

$$d^6\Phi_\nu'^e(s) = \eta_\nu(s) dS ds d\Omega d\nu = \kappa_\nu n^2 L_\nu^\circ(T_s) dS ds d\Omega d\nu \tag{3.6}$$

where $\eta_\nu(s)$ is the monochromatic emission coefficient. Under the local thermodynamic equilibrium assumption, the absorbed flux is equal to the emitted one. So $\eta_\nu(s) = \kappa_\nu n^2 L_\nu^\circ(T_s)$ with n is the simple refractive index. $L_\nu^\circ(T)$ is the blackbody intensity and it depends on temperature T and frequency ν (only the spontaneous emission is taken into account here and the induced emission is neglected).

In particular, a engineering parameter "emissivity" (ε'_ν) has been defined to characterize the radiation emission ability of an isothermal medium compared with the emission from a blackbody at the same temperature[2] (Taine et al. 2003):

$$\varepsilon'_\nu = 1 - \exp(-\kappa_\nu l) = \alpha'_\nu = 1 - \tau'_\nu \tag{3.7}$$

where α'_ν is the absorptivity defining the absorption ability of a medium that determines the fraction of radiant energy traveling along a path that will be absorbed within a given distance and τ'_ν is the transmissivity defining the transmission ability of a medium that determines the fraction of energy at the origin of a path that will be transmitted through a given thickness (Siegel and Howell 1981).

In-scattering

Different from the "out-scattering" mentioned above, the "in-scattering" defines the energy gained by the scattering. The scattered energy produced by an optical path in the direction of u' obtained by another optical path in the direction u can be represented as:

$$d^6\Phi^{s+}_\nu = \frac{\sigma_\nu}{4\pi} ds dS d\Omega d\nu \int_0^{4\pi} P_\nu(\vec{\Delta}' \to \vec{\Delta}) L'_\nu(\vec{\Delta}') d\Omega' \tag{3.8}$$

where a phase function $P_\nu(\vec{\Delta}' \to \vec{\Delta})$ has been introduced to describe the angular distribution of the scattered energy, and the probability of the optical path from the direction $\vec{\Delta}'$ scattered into another direction $\vec{\Delta}$ is $(d\Omega/4\pi)P_\nu(\vec{\Delta}' \to \vec{\Delta})$.

3.2 Radiative transfer equation

As shown in Fig. 3.2, the radiation energy traveling in an optical path from s to $s + ds$ is decreased by absorption and out-scattering and is enhanced by the spontaneous emission and in-scatttering. Using the equations discussed above (Eqs. 3.2, 3.6 and 3.8), a first-order integral-differential equation, radiative transfer equation (RTE) is developed to describe the radiation intensity along a path of ds long in the direction $\vec{\Delta}$.

$$\begin{aligned}\frac{d^6\Phi'_\nu}{ds dS d\Omega d\nu} = & \underbrace{-[\kappa_\nu(s) + \sigma_\nu(s)] L'_\nu(s, \vec{\Delta})}_{\text{attenuation: absorption + out-scattering}} + \underbrace{\kappa_\nu(s) n^2(s, \vec{\Delta}) L^\circ_\nu(T_s)}_{\text{gain by emission}} \\ & + \underbrace{\frac{\sigma_\nu}{4\pi} \int_0^{4\pi} P_\nu(s, \vec{\Delta}' \to \vec{\Delta}) L'_\nu(s, \vec{\Delta}') d\Omega'}_{\text{gain by in-scattering}}\end{aligned} \tag{3.9}$$

With the definition of radiation intensity, Eq. (3.9) can be rewritten as:

$$\begin{aligned}n^2(s, \vec{\Delta}) \frac{d}{ds}\left\{\frac{L'_\nu}{n^2}[s, \vec{\Delta}]\right\} = & -[\kappa_\nu(s) + \sigma_\nu(s)] L'_\nu(s, \vec{\Delta}) + \kappa_\nu(s) n^2(s, \vec{\Delta}) L^\circ_\nu(T_s) \\ & + \frac{\sigma_\nu}{4\pi} \int_0^{4\pi} P_\nu(s, \vec{\Delta}' \to \vec{\Delta}) L'_\nu(s, \vec{\Delta}') d\Omega'\end{aligned} \tag{3.10}$$

[2] In Eq.(3.7), the scattering is not taken into account.

The unsteady time term $\partial/\partial t$ contained in the first term d/ds is generally neglected because radiation propagation can be considered infinitely fast in usual cases.

For no-scatting medium, $\sigma_\nu = 0$, Eq. (3.10) can be integrated in the interval $[0, s]$ and written as (Taine et al. 2003):

$$\begin{aligned}\frac{L'_\nu}{n^2}(s,\vec{\Delta}) &= \frac{L'_\nu}{n^2}(0,\vec{\Delta})\tau_\nu(0\to s) + \int_0^s \kappa_\nu(s')L^0_\nu(T(s'))\tau_\nu(s'\to s)ds' \\ &= \frac{L'_\nu}{n^2}(0,\vec{\Delta})\tau_\nu(0\to s) + \int_0^s L^0_\nu(T(s'))\frac{\partial\tau_\nu(s'\to s)}{\partial s'}ds' \end{aligned} \tag{3.11}$$

where the first term represents the energy transmitted from 0 to s based on the incident intensity at $s = 0$ and the second term represents the energy emitted by each element s' between 0 and s and the transmission of this energy from s' to s. $\tau_\nu(s' \to s)$ is the monochromatic transmissivity from s' to s:

$$\tau_\nu(s'\to s) = \exp\quad\left[\int_{s'}^{s} -\kappa_\nu(s'')ds''\right] \tag{3.12}$$

and $\int_{s'}^{s}\kappa_\nu(s'')ds''$ represents the optical thickness between s' and s.

Radiative heat flux

In general, the radiative heat flux Φ^R is one of the most useful radiation quantities in engineering applications. Considering the radiative energy conservation in a volume element V with the closure G around as shown in Fig. 3.3, the radiative volume power $P^R(G)(W/m^3)$ and the surface radiative flux ϕ^R (W/m^2) can be represented as (Tesse 2001):

$$\underbrace{\int}_{\text{volume}} P^R(G)dV + \underbrace{\oint}_{\text{surface}} \phi^R(F)dS = 0 \tag{3.13}$$

where dS corresponds to the surface area of the closure G and F is the departure point of the optical path on the closure G. Using the radiation flux vector $\vec{q}^R$ and the divergence of the radiative heat flux $(\vec{\nabla}\cdot\vec{q}^R)$, the integration of the surface radiative flux on G can be written as:

$$\underbrace{\oint}_{\text{surface}} \phi^R(F)dS = \underbrace{\oint}_{\text{surface}} -\vec{n}\cdot\vec{q}^R(F)dS = \underbrace{\int}_{\text{volume}} [\vec{\nabla}\cdot\vec{q}^R]_{s=G}dV \tag{3.14}$$

And $\vec{n}$ is the normal direction of the surface G on the point F. Combining with Eq. (3.13) and Eq. (3.10) and neglecting the scattering, we have:

$$\begin{aligned} P^R(G) &= -[\vec{\nabla}\cdot\vec{q}^R]_{s=G} = -\int_0^\infty \underbrace{\int}_{4\pi}\left[\frac{\partial L_\nu(s,\vec{\Delta})}{\partial s}\right]_{s=G} d\Omega d\nu \\ &= \underbrace{\int_0^\infty \underbrace{\int}_{4\pi}\kappa_\nu(G)L'_\nu(G,\vec{\Delta})d\Omega d\nu}_{\text{absorption}} - \underbrace{4\pi\int_0^\infty \kappa_\nu(G)L^0_\nu(T_G)d\nu}_{\text{emission}} \end{aligned} \tag{3.15}$$

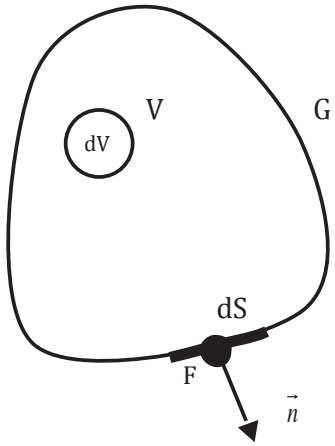

Figure 3.3 – *Flux calculated on a surface dS of the closure G*

In this thesis, this term is calculated by the radiation solver and will be sent to the combustion LES solver as the radiative source term.

Boundary conditions problem

To obtain the solution of Eq. (3.9), the integration constant corresponding to the intensity at the departure point of the optical path must be determined. Because most of these departure points are usually at the boundary of the radiating medium, so the radiation at the boundaries should be taken into account and coupled with the radiation distribution inside the medium (Siegel and Howell 1981). For this reason, the influence of the boundary condition for the radiative problem can not be neglected. However, limited by the computational source and the boundary material property complexities, simplified models usually are used for boundary simulating. A more detailed discussion about the boundary condition problem will be offered in this thesis in Chapter 6.

3.3 RTE resolution methods

Several resolution methods of the radiative transfer equation are presented in this section. Firstly, the ray-tracing method will be shortly introduced, because from a certain point of view, its principle is close to Monte Carlo method which can be considered as its statistical variant. Then the Discrete Ordinate Method (DOM) is briefly presented to prepare the comparison between DOM and Monte Carlo Method in the chapter 5. Finally, a detailed bibliography for the Monte Carlo method retained in this thesis is provided.

The geometrical, directional and spectral complexities of the radiative transfer limit its analytical resolution, so some numerical methods have been proposed to calculate the radiative power and flux. These methods usually use the temperature, molar fraction, volume fraction and other physical properties of the medium as input data. In general, they can be divided into two kinds: deterministic methods like ray tracing method, Pn method and Discrete Ordinate Method and statistical methods like Monte Carlo Method.

3.3.1 Ray-tracing method

Ray-tracing method is one of the most general deterministic methods. More details about this method can be found in the references Taine (2003) and Iacona (2000), only some main characteristics of this method will be presented here.

Computational domain discretization

As shown in Fig. 3.4, a three-dimensional volume can be characterized by N_m points $M_k (k = 1, \cdots, N_m)$ inside the medium and N_p points $P_j (j = 1, \cdots, N_p)$ on its surrounding surface. These points are distributed irregularly but "determined" (different from "randomly" for

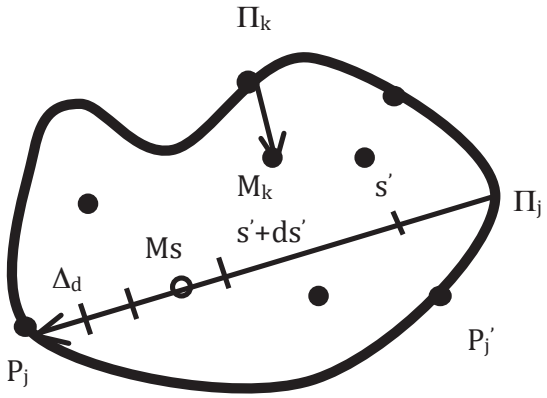

Figure 3.4 – *Ray tracing method*

the points of Monte Carlo method, to be presented later in this chapter).

For each point M_k inside the medium, the absorption coefficient $\kappa_{k\nu}$, the scatter coefficient $\sigma_{k\nu}$ and the phase function $P_{k\nu}(\vec{\Delta}' \rightarrow \vec{\Delta})$ (parameters required by Eq. (3.9)) are estimated from local thermo-physical properties, such as the temperature (T_k), the molar fraction of phase i (x_{ki}), etc. The same principe for each point P_j on the surrounding surface. The temperature T_j and the reflectivity ρ_j of the boundary surface are considered as the input parameters.

Spectral and direction discretization

The objective is to get the radiative flux ϕ_j^R on point P_j and the radiative volume power P_k^R on point M_k independently. These two quantities are determined based on the monochromatic intensity $L'_\nu(P_j, \vec{\Delta})$ and $L'_\nu(M_k, \vec{\Delta})$ for all the points, where $\vec{\Delta}$ corresponds to the discretized optical path direction. The total computational space can be discretized on N_d directions covering 4π steradians (here N_d represents the number of the directions discretized).

Each optical path departure from one point P_j or M_k in a given direction $\vec{\Delta}$ (ex: $\overrightarrow{\Pi_j P_j}$) is then discretized into N_s segments along the path. This discretization is repeated for N_ν frequencies covering the spectral properties.

Furthermore, in numerical simulations, N_{it} iterations are required to resolve this linear equation system (N_{it} depends on the number of unknown parameters in the equation system).

So the number of elements based on the points chosen inside the volume to characterize the discretization of the calculated system is $N_{it}N_\nu N_m N_d N_s$ and for the points on the surrounding surface is $N_{it}N_\nu N_p N_d N_s$ (Taine et al. 2003).

Determination of radiative flux ϕ_j^R and and radiative volume power P_k^R

To simplify the problem, no scattering medium and black body surface is considered here (the case with scattering medium and more details can be found in Taine *et al.*, 2003). The radiative flux ϕ_j^R on point P_j is written as :

$$\phi_j^R = \int_0^\infty \mathrm{d}\nu \int_{2\pi} (L_{j\nu d}^{'i} - L_{j\nu d}^{'p}) \cos\theta \mathrm{d}\Omega \tag{3.16}$$

where the angle θ and the solid angle $d\Omega$ associated with the ray in the direction Δ are shown in Fig. 3.5. $L_{j\nu d}^{'i}$ and $L_{j\nu d}^{'p}$ represent respectively the monochromatic directional incident

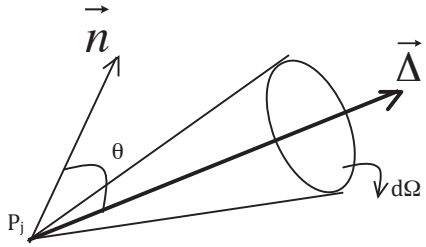

Figure 3.5 – *Ray tracing method - Monochromatic intensity on point P_j*

intensity on P_j and intensity leaving from P_j. They can also be presented as $L_\nu^{'i}(P_j, \vec{\Delta})$ and $L_\nu^{'p}(P_j, \vec{\Delta})$.

$L_{j\nu d}^{'i}$ is obtained by using the intensity leaving from point Π_j located on the surrounding surface in direction $\vec{\Delta}$:

$$L_{j\nu d}^{'i} = L_{\nu d}^{'p}(\Pi_j)\tau_{\nu\Pi_j P_j}^{'} + \int_0^{\Pi_j P_j} n^2 L_\nu^\circ[T(s)] \frac{\partial}{\partial s}\tau_{\nu s P_j}^{'} \mathrm{d}s \tag{3.17}$$

where s is the coordinate of point M_s on optical path $\overrightarrow{\Pi_j P_j}$, $\tau_{\nu\Pi_j P_j}^{'}$ and $\tau_{\nu s P_j}^{'}$ are the local medium transmissivity.

Equation 3.17 is then discretized and the properties associated with a point M_s along the discretized optical path can be interpolated based on the corresponding properties associated with point M_k in the medium (Taine et al. 2003):

$$L_\nu^\circ[T(M_s)] = \sum_k a_k L_\nu^\circ[T(M_k)] \tag{3.18}$$

with the same principe, because point Π_j is not a discretization point, so $L_{\nu d}^{'p}(\Pi_j)$ is obtained by using the interpolation based on the discretization point $P_{j'}$ in the direction $\vec{\Delta}$ with the same frequency:

$$L_{\nu d}^{'p}(\Pi_j) = \sum_{j'} b_{j'} L_{j'\nu d}^{'p} \tag{3.19}$$

where a_k and $b_{j\prime}$ are tabulated (Iacona 2000; Iacona et al. 2002; Lecanu 2005).

The term departure intensity $L'^{p}_{j\nu d}$ leaving from point P_j is calculated as:

$$L'^{p}_{j\nu d} = \varepsilon'_{j\nu d}\ n^2\ L^{\circ}_{\nu}(T_j) + \frac{1}{\pi}\ \int_{2\pi}\ \rho''_{j\nu d' d}\ L'^{i}_{j\nu d'}\ \cos\theta'\ \mathrm{d}\Omega' \tag{3.20}$$

where ε is the emissivity and $\rho''_{j\nu d' d}$ is the reflectivity which characterizes an optical ray entering in $d\Omega'$ (direction $\vec{\Delta}'$) and reflecting in $d\Omega$ (direction $\vec{\Delta}$). If the system is surrounded by the black body wall, the equation system is closed. Additionally, if the boundary is isotropic, Eq. 3.20 is written as:

$$L^{p}_{j\nu} = \varepsilon_{j\nu} n^2 L^{\circ}_{\nu}(T_j) + (1-\varepsilon_{j\nu}) L^{i}_{j\nu} \tag{3.21}$$

With the similar principe as ϕ^{R}_{j}, the radiative power in point M_k (Fig. 3.4) is:

$$P^{R}(M_k) = \int_0^{\infty} \left[\int_0^{4\pi}\ \kappa_{k\nu}\ L'_{k\nu d}\mathrm{d}\Omega - 4\pi\kappa_{k\nu} L^{\circ}_{\nu}(T_k) \right] \mathrm{d}\nu \tag{3.22}$$

where $L'_{k\nu d}$ is incident intensity on point M_k obtained by using the antecedent point located in the surrounding surface.

Compared with other methods

Ray-tracing and Discrete ordinate method:

In ray tracing method, the directional intensity calculation at one point (M_k or P_j) to determine the flux and the radiative power is realized directly on this point itself and it is independent on the results of the computations achieved at its neighboring points. On the other hand, in interpolation methods, such as Discrete Ordinate Method, the calculations performed at one point depends the results of its neighboring points. And another important point for Discrete Ordinate Method is that the number of the discretized directions taken into account has been reduced from ~ 200 to ~ 20 (order of magnitude) by a quadrature technique.

Ray-tracing and Monte Carlo method:

As mentioned above, the ray tracing method is similar to the Monte Carlo method. However the difference between them is that for ray-tracing method, all of the characteristic parameters such as departure points, directions, frequency, are fixed. For Monte Carlo method, they are determined statistically

3.3.2 Discrete ordinate method

Discrete ordinate method (DOM) is one of the most widely used radiation models and it has the reputation to ensure a good compromise between solution accuracy and computational requirement for many practical applications (Coelho 2007).

This method is based on a discrete presentation of the directional variation of the radiative intensity. A solution to the transport problem is found by solving the transfer equation for a set of discrete directions spanning the total solid angle range of 4π. So it is a finite differencing of the directional dependence of the equation of transfer (Modest 2003).

More details about this method can be found in Taine (2003) and Goncalves Dos Santos (2008). Here only some main characteristics are summarized as below:

- The radiative intensity calculation for a given direction is realized portion by portion along the optical path from the departure point using the results obtained on the neighboring points.
- The number of discrete directions is largely reduced by the special quadrature formula. For ray tracing method, at least 200 directions are needed for a converged computation. For DOM, 24 directions can provide a precise results for the combustion application modeled by LES (Goncalves Dos Santos 2008).
- The interpolation technique within a emissive, absorptive and no-diffusive medium can be presented as shown in Fig. 3.6 (Taine et al. 2003). Supposing that, at iteration

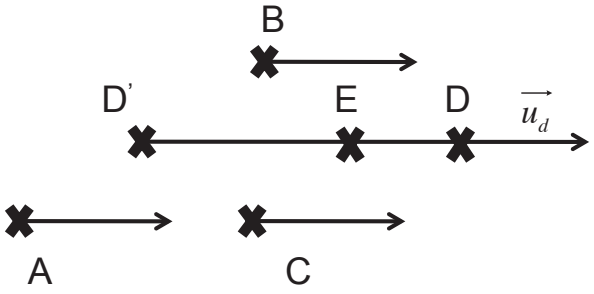

Figure 3.6 – *Interpolation technique of Discrete Ordinate Method*

n, the radiative intensity distribution leaving from all the points on the surrounding surface P_j have been already determined as $L'^{p(n)}_{j\nu d}$, and the intensity at each point M_k within the medium is $L'^{(n)}_{k\nu d}$ (see 3.3.3). For each direction $\vec{u_d}$, the intensity departure from the surrounding surface can be calculated portion by portion.

As shown in Fig. 3.6, supposing that the intensities at points A, B and C are already known, and D' is the antecedent point of D, E is a point in the optical path $\vec{D'D}$, the intensity at point D in the direction $\vec{u_d}$ can be deduced as:

$$L'_{D\nu d} = \tau'_{\nu D'D} L'_{D'\nu d} + (1 - \tau'_{\nu D'D}) L^{\circ}_{\nu}(T_E) \tag{3.23}$$

And with

$$L_{D'\nu d} = sum_{I=A,B,C} a_I L'_{I\nu d} \tag{3.24}$$

At the end of all the iterations, all of the monochromatic incident intensities at P_j can be computed on function of the intensities leaving from point P_j. And then the same principe as 3.3.3 is applied. More details can be found in (Taine et al. 2003).

The shortcomings of this method are that:

- Reducing the number of discrete elements can reduce the complexity of the computation at a certain level, however, the integration of the optical discrete directions will loose precision.
- The special quadrature formula is considered to be valid only for weakly anisotropic media.

3.3.3 Monte-Carlo method

introduction

The Monte Carlo method, as a class of numerical techniques based on the statistical characteristics of physics processes, was originally developed to resolve the mathematic multi-integration problem. And its earlier application in engineering and science was to analyze the potential behavior of nuclear weapons, where experiments were difficult to perform and analytic methods available at that time were not sufficient to provide accurate prediction of behavior (Metropolis et al. 1949). In recent years, with the rapid increase in computer power and the development of massively parallel architectures, this method becomes more and more common.

In the thermal radiative transfer application, the Monte Carlo method directly simulates the physical processes by generating a large number of random optical rays characterized by random departure points, random spectral frequencies and random directions of propagation. According to the statistical theory, these three parameters should be chosen independently according to given distribution functions.

Compared with other methods available to resolve the radiative transfer equation, the principle advantage of the Monte Carlo method is that many complex physical phenomena, such as spectral dependence of surface and participating medium properties, non-isotropic scattering distributions, complex 3D geometries including obstacles, coupling with turbulent temperature and concentration fields, can be taken into account simultaneously without simplifying assumptions (ex: optically thin fluctuation assumption and assumption on gas radiative properties) and without huge increases of CPU time. The second advantage is that the only remaining uncertainty produced in this method is the statistical error, so statistical tests can be used to estimate this uncertainty (in terms of variance or standard deviation) in the results. This method then can be considered as a quasi-exact reference to validate other approaches.

To overcome its disadvantages, such as the huge memory requirement and the slow convergence speed, improve its performance and simplify its implementation, different strategies were proposed. Firstly, some algorithms similar to Monte Carlo method have also been developed, such as the READ (Radiant Energy Absorption Distribution), REM (Radiation Element Method by Ray Emission Model) and DFP (Discrete Probability Function) separately suggested by Yang et al. (1995), Maruyama and Aihara (1997) and Sivathanu and Gore (1993). Secondly, some standard deviation reduction techniques have been employed in some particular cases to reduce the CPU time (Kobiyama 1989; Surzhikov and Howell 1998; Martin and Pomraning 1990). For example, an "energy-partitioning" method proposed by Shamsundar has been found efficient in some cases with ”open” configurations (Shamsundar et al. 1973). In the standard Monte Carlo method, a ray carrying a fixed amount of energy is emitted from one point and ends when its energy is completely absorbed at a certain point in the participating medium or at the wall, or when it escapes from the enclosure. This model of energy distribution is inefficient for the cases with highly reflective walls or in optically thin media, most photon bundles exit the enclosure without any contribution to the statistics (Ju et al. 1999) but consuming CPU time. On the other hand, in the "energy-partitioning" method, the energy carried by a ray is not absorbed at a single point, but is attenuated gradually along its path until its depletion or until it leaves

the enclosure. In this thesis, this "energy-partitioning" technique is used. Furthermore, a reverse Monte Carlo technique (called the emission path method) based on a reciprocity principle, firstly presented by Walters and Buckius, has also many advantages compared to the standard Monte Carlo for certain problems (Walters and Buckius 1992; Walters and Buckius 1994). It is also used in this thesis and will be detailed in the next part.

Reciprocal Monte-Carlo method

This "reverse Monte Carlo" technique is firstly introduced by Walters and Buckius (called emission path method) and it only uses the geometrical features reversed to calculate the radiative flux at a given boundary point of a complex system (Walters and Buckius 1992).

As mentioned in Waters and Buckius (1992 and 1994), the original purpose for developing this "reverse" technique is to improve the computation efficiency of the classical Monte Carlo method (called "forward Monte Carlo method") when only the radiative intensity hitting on a small spot and/or over a small range of solid angles is required, in this case, the probability of the optical paths generated randomly from the source points (located in a large complex configuration), hitting on the small detector, is quite limit. So many optical paths generated cannot reach the detector, which will be a waste of time.

This "reverse Monte Carlo technique" is then improved by many investigators. Cherkaoui (1996), Cherkaoui (1998) and de Lataillade et al. (2002) are the first authors to use the reciprocity principe for one dimensional fields from the point of view of both geometry and exchanged power (EMCM, Exchange Monte Carlo Method)[3]. They have applied this EMCM Monte Carlo method to analyze a wide range of nearly isothermal configurations with specular as well as diffuse surfaces, and the results have shown that, for some particular conditions, computations with EMCM are at least two orders of magnitude faster and the method remains operational for optically thick systems.

For three computational dimensional fields, Tesse et al. (2002) has presented and compared the conventional forward Monte Carlo (FM) with two reciprocal Monte Carlo formulations which are call respectively ERM (emission reciprocity method) and ARM (absorption reciprocity method). These three formulations have been applied to one-dimensional benchmark cases involving gray media or real gas-mixtures, different optical thicknesses and different thermal conditions. For real gas-mixtures, gas radiative properties are treated in a correlated manner by a CK model based on the parameters of Soufiani and Taine (1997).

But in the case involving moderate optical thicknesses and high temperature gradients (radiation combustion gases, for instance), none of the three methods gives the lowest standard deviation in the whole calculation domain. So another more suitable method ORM (optimized reciprocity method) has been developed by Dupoirieux et al. (2006).

Principe

[3]In fact, the reciprocal technique can be applied from the point of view of only the geometry (Walters and Buckius 1992; Walters and Buckius 1994), it means that only the same optical path is used geometrically, but the power exchanged cannot be computed directly from this optical path. In this thesis, both geometry and exchanged power are considered. It means that with the formulations proposed, the power exchanged can be calculated directly from this optical path, even though the power exchanged between the source point and one point along the optical path.

The "reciprocal Monte Carlo method" used in this thesis is also considered as one of the "reverse" techniques, it is firstly proposed by Taine (Taine et al. 2003) and then is validated by Tesse (2001).

The principle is that the optical path is considered in a reverse manner, which means a ray tracing can be used two times, both in the forward direction and in the reverse (reciprocal) direction as shown in Fig. 3.7. The power exchanged between a source cell (cell from which an optical path is built) and each cell crossed by the optical path is directly calculated. It can be presented as[4] (Tesse 2001):

If a ray tracing can propagate from cell i to cell j, then it surely exists another ray tracing propagating from cell j to cell i following the same path. The ratio of the monochromatic energy emitted by cell i and absorbed by cell j to the monochromatic energy emitted by cell j and absorbed by cell i is equal to the ratio of the equilibrium spectral intensities of cell i and j

$$\frac{P^{ea}_{\nu,ij}}{P^{rea}_{\nu,ji}} = \frac{L^0_\nu(T_i)}{L^0_\nu(T_j)} \tag{3.25}$$

where $P^{ea}_{\nu,ij}$ is the monochromatic energy emitted by cell i and absorbed by cell j in the forward direction and $P^{rea}_{\nu,ji}$ is the monochromatic energy emitted by cell j and absorbed by cell i in the reciprocal direction using the same optical path. And their integrations in the frequency spectrum $[0, +\infty]$ are:

$$P^{ea}_{ij} = \int_0^\infty P^{ea}_{\nu,ij} d\nu \tag{3.26}$$

$$P^{rea}_{ji} = \int_0^\infty P^{rea}_{\nu,ji} d\nu \tag{3.27}$$

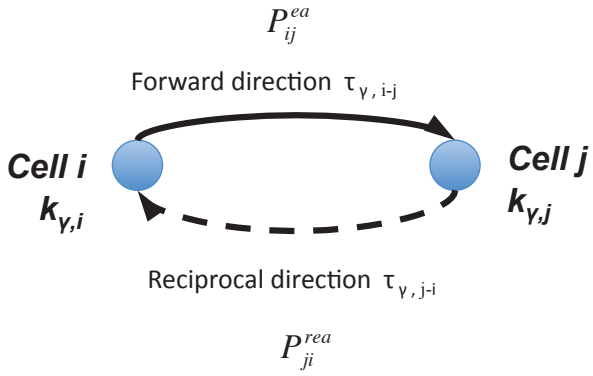

Figure 3.7 – *Principe of the Reciprocal Monte Carlo Method*

The rigorous demonstration of this principe provided by Tesse (2001) will be not repeated here, we juste make this principe to be understood by explaining the exchange formulation of radiative transfer presented in the Ph.D thesis of Tesse (2001). Considering an enclosure with non-isothermal opaque walls, containing a non-isothermal, heterogeneous, absorbing and emitting medium. The medium and the walls are divided into N_v elementary volumes

[4]Different authors have defined the reciprocal Monte Carlo method by different formulas. Here just the principe used in this thesis is presented.

(called cell) and N_s elementary surfaces (called cell, too). Each cell is assumed to be isothermal, homogeneous and characterized by uniform radiative properties (see Fig. 3.8).

The main idea of the exchange formulation of radiative transfer is that the radiative power (or radiative flux) in the cell i can be written as a sum of exchange terms with all the other cells j (Tesse et al. 2002):

$$P_i = \sum_{j=1}^{N_v+N_s} P_{ij}^{exch} = \sum_{j=1}^{N_v+N_s} -P_{ji}^{exch} \tag{3.28}$$

where P_{ij}^{exch} is the radiative power exchanged between the cells i and j, and can also be written as:

$$P_{ij}^{exch} = P_{ji}^{rea} - P_{ij}^{ea} = \int_0^\infty (P_{\nu,ji}^{rea} - P_{\nu,ij}^{ea}) d\nu \tag{3.29}$$

Assuming that:

$$\frac{P_{\nu,ij}^{ea}}{P_{\nu,ji}^{rea}} = M_{ij} \tag{3.30}$$

where M_{ij} is a ration of power between i and j, Eq. 3.29 can be written as:

$$P_{ij}^{exch} = \int_0^\infty P_{\nu,ij}^{ea} \left(\frac{1}{M_{ij}} - 1 \right) d\nu \tag{3.31}$$

Then the term P_{ij}^{exch} will be detailed below to show that term M_{ij} in Eq. 3.30 is equal to $L_\nu^0(T_i)/L_\nu^0(T_i)$.

Supposed that both cells i and j are volumes, as demonstrated in Ph.D thesis Tesse (2001), P_{ij}^{exch} is given:

$$P_{ij}^{exch} = \int_0^\infty k_{\nu,i}[L_\nu^0(T_j) - L_\nu^0(T_i)] \int_{V_i} \int_{4\pi} \sum_{c=1}^{N_p} \tau_\nu(BF_c) \left[\int_0^{l_{jc}} k_{\nu,j} \exp(-k_{\nu,j} s_{jc}) ds_{jc} \right] d\Omega_i dV_i d\nu \tag{3.32}$$

as shown in Fig. 3.8, an optical path departing from point B of cell i firstly arrives at the boundary $w1$ with emissivity $\varepsilon_{w1\nu}$, then arrives at the first inlet point F1 of cell j, after passing through cell j, reaches the boundary $w2$ with emissivity $\varepsilon_{w2\nu}$, then crosses cell j again with the second inlet point F2. $k_{\nu,i}$ is the spectral absorption coefficient relative to cell i. N_p represents the total number of crossing of cell j by a given optical path issued from cell i. In Fig. 3.8, the optical path crosses cell j for two times, so $N_p = 2$ (just an example). $\tau_\nu(BF_c)$ is the spectral transmissivity between the source point B associated with dV_i and F_c the c^{th} inlet point in the cell j of a given optical path. s_{jc} is the abscissa, taken from F_c to the current point G_c in cell j for the c^{th} crossing. l_{jc} represents the length of the c^{th} crossing of cell j by a given optical path. $d\Omega_i$ is an elementary solid angle issued from the source point B and centered around a direction Δ.

The spectral transmissivity is given by

$$\tau_\nu(BF_c) = \exp\left(- \sum_{m=1}^{M_c-1} k_{\nu,m} l_m \right) \prod_{h=1}^{N_{rc}} (1 - \varepsilon_{wh\nu}) \tag{3.33}$$

where l_m is the distance traveled through the cell m, $m = 1$ and $m = M_c$ correspond respectively to the first cell crossed by the optical path (cell i) and the last one for the c^{th} crossing (cell j). N_{rc} is the number of wall refections along the optical path between point B and F_c, h is the index of wall reflections along this optical path and $\varepsilon_{wh\nu}$ is the local wall spectral emissivity.

And in Eq. 3.32, the integration over the volume V_j has been replaced by integrations over the solid angle 4π and the length l_{jc} (Tesse et al. 2002):

$$\frac{dV_{jc}}{l^2_{BG_c}} = ds_{jc} d\Omega_i \tag{3.34}$$

where l_{BG_c} is the length of an optical path between the source point B and the current point G_c.

After analytical integration over the length l_{jc}, the radiative power exchanged between cells i and j becomes:

$$P^{exch}_{ij} = \int_0^\infty k_{\nu,i} L^0_\nu(T_i) \left(\frac{L^0_\nu(T_j)}{L^0_\nu(T_i)} - 1 \right) \int_{V_i} \int_{4\pi} \sum_{c=1}^{N_p} \tau_\nu (BF_c) \alpha_{\nu,jc} d\Omega_i dV_i d\nu \tag{3.35}$$

where $\alpha_{\nu,jc}$ is the spectral absorptivity associated with the column of length l_{jc} and defined by:

$$\alpha_{\nu,jc} = 1 - \exp(-k_{\nu,j} l_{jc}) \tag{3.36}$$

In the formulation Eq. 3.35, an elementary exchange is an exchange between an elementary volume dV_i around point B of cell i and an elementary column of length l_{jc} crossing cell j.

On the other hand, the spectral power emitted by cell i and absorbed by cell j P^{ea}_{ij} can be written:

$$P^{ea}_{ij} = \int_0^\infty P^{ea}_{\nu,ij} d\nu = \int_0^\infty k_{\nu,i} L^0_\nu(T_i) \int_{V_i} \int_{4\pi} \sum_{c=1}^{N_p} \tau_\nu (BF_c) \alpha_{\nu,jc} d\Omega_i dV_i d\nu \tag{3.37}$$

Referring to Eq. 3.31, Eq. 3.35 and Eq. 3.37, the reciprocal principe shown in Eq. 3.25 is clearly fulfilled.

In this thesis, one of the reciprocal Monte Carlo methods (FM, ERM, ARM and ORM) mentioned in Tesse (2001) and Dupoirieux et al. (2006) which is the best suitable for our computation case will be used. So at first, the realizations of these formulations will be detailed in the next part.

3.3.4 Monte Carlo Numerical Scheme used in this thesis

In the Forward (classical) Monte Carlo method (FM), the optical path (ray) defined from point A to point B is only used to compute the power emitted from A and exhausted at point B, but in the reciprocal method (ERM, ARM and ORM), the same path is used for calculating the power exchanged between A and B, that means radiative transport from A to B and from B to A are associated.

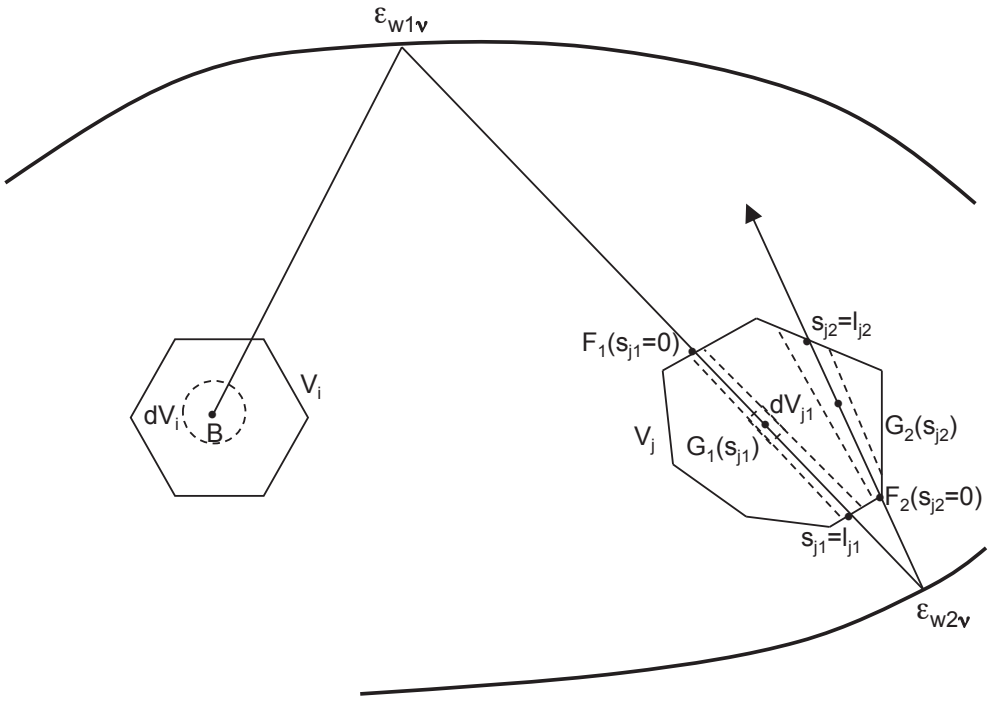

Figure 3.8 – *Coupled elementary cells for exchange formulation*

Now we consider an enclosure with opaque wall, containing non-isothermal, absorbing and emitting medium, and divide the medium and the walls into Nv elementary volumes and Ns elementary surfaces (Fig. 3.48). Both of them are called cells in the following.

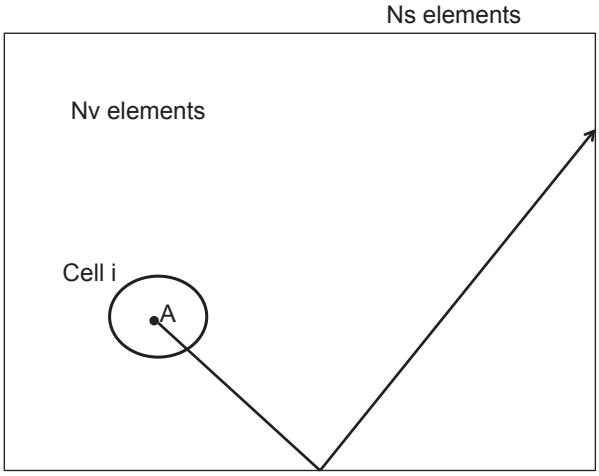

Figure 3.9 – *Enclosure to be computed*

Step1:

Building a large number of optical paths N from each cell which are characterized by three parameters generated randomly: the frequency ν, the direction Δ and the source point A. Each optical ray carries a certain amount of energy determined by the emission energy of the source point. Because these parameters are independent, noting the function distribution

for cell i (source point A):

$$f_i\left(A,\Delta,\nu\right)=f_{1,i}\left(A\right)f_{2,i}\left(\Delta\right)f_{3,i}\left(\nu\right) \tag{3.38}$$

Determination of the source point A

- Creating a smallest parallelepiped surrounding cell i
- Randomly picking one point from this parallelepiped.
- If the point picked in the previous step is located inside cell i, the point is decided as the source point A. Otherwise, repeat the previous step.

Determination of the frequency ν distribution function

The distribution function of the frequency ν is obtained by the following formulation:

$$R=\int_0^{\nu_n} f_{3,i}\left(\nu\right)d\nu=\frac{\int_0^{\nu_n} k_{i,\nu}L_\nu^0\left(T_i\right)d\nu}{\int_0^{\infty} k_{i,\nu}L_\nu^0\left(T_i\right)d\nu} \tag{3.39}$$

where R is a uniform random number in [0,1]. A CK model has been implemented here to determine the $k_{i,\nu}$, more details are presented in AppendixA.

Determination of direction Δ distribution function

Two independent uniform random numbers R_θ and R_φ defined in interval $[0,1]$ are used to determine the optical path direction, which can be described by two angles θ and φ as shown in Fig. 3.10:

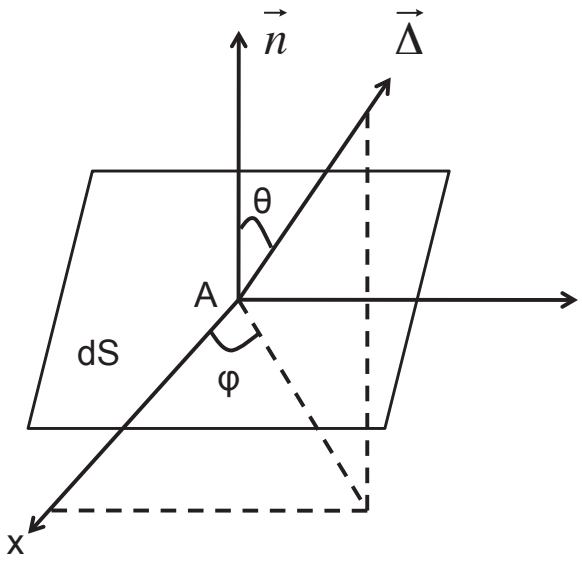

Figure 3.10 – *Definition of the angles θ and φ, direction $\vec{\Delta}$ departing from point A on the surface dS*

$$\theta=\arccos\left(1-2R_\theta\right) \tag{3.40}$$

$$\varphi=2\pi R_\varphi \tag{3.41}$$

θ is the angle between the normal direction $\vec{n}$ of the surface dS and the propagation direction $\vec{\Delta}$. If the source point is located in one cell inside the radiative medium, the optical path can cover all the 4π space. So the intervals of these two angles are:

$\theta \in [0, \pi]$ and $\varphi \in [0, 2\pi]$

For the source points located on the surface element with diffuse emissivity, only 2π space can be accessed by the optical path:

$$\theta = \arccos\left(\sqrt{R_\theta}\right) \tag{3.42}$$

$$\phi = 2\pi R_\phi \tag{3.43}$$

And the intervals of these two angles are:

$\theta \in [0, \pi/2]$ and $\varphi \in [0, 2\pi]$

Step 2:

Each optical path crosses successively each cell in the selected optical direction, when the optical path goes through a cell, the energy absorbed in this cell is computed with the local crossed length absorptivity and the remained energy in the path leaving from this cell can be computed with the local transmissivity. In this way, the energy carried along the path will decrease gradually until the amount of energy becomes less than a cutoff value or until the path leaves the enclosure.

Forward Monte Carlo method (FM)

A statistical estimation of the exchanged energy between cell i and other cells (radiative power in cell j) can be expressed by the following equation (Fig. 3.11):

$$\tilde{P}_i^{FM} = \sum_{j=1}^{N_v+N_s} \tilde{P}_{ji}^{ea} - P_i^e \tag{3.44}$$

Here $\tilde{P}_{ji}^{ea}$ is the statistical estimation of the power emitted by cell j and absorbed by cell i, it can be obtained by averaging the contributions of all the N_i optical paths (but only N_{ij} optical paths give rise to a non zero contribution). Referring to Eq. 3.37, it is written as:

$$\tilde{P}_{ji}^{ea} = \frac{P_j^e}{N_i} \sum_{n=1}^{N_{ij}} \sum_{c=1}^{N_{pn}} \tau_{\nu,n}(B_{jn}F_{ic})\alpha_{\nu,ic} \tag{3.45}$$

noting that the integrations of $d\nu$, dV_i and $d\Omega_i$ in Eq. 3.37 are replaced by $\sum_{n=1}^{N_{ij}}$ here, because the optical paths are generated randomly based on three parameters: source point (dV_i), direction ($d\Omega_i$) and frequency ($d\nu$). And P_i^e is the energy emitted by cell i calculated in a deterministic manner:

$$P_i^e = \int_0^\infty k_{\nu,i} L_\nu^0(T_i)\, d\nu \int_{V_i} \int_{4\pi} d\Omega_i dV_i \tag{3.46}$$

Evidently, the exchange power $\tilde{P}_i^{FM}$ in FM model not only depends on the emission of cell i but also depends the emission of cell j.

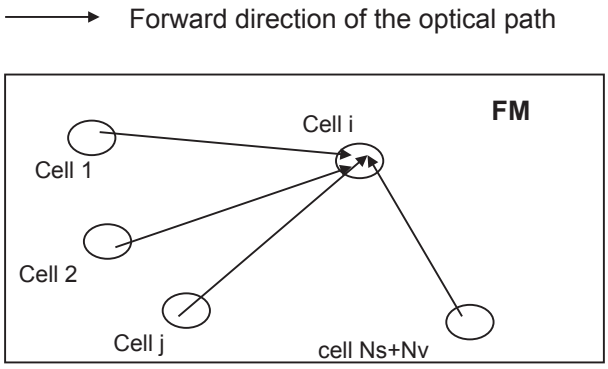

Figure 3.11 – *Forward Monte Carlo Method*

Reciprocal Monte Carlo method

Using the reciprocal principle to calculate the exchanged power in cell i with the **Emission Reciprocity Method (ERM)** (shown as Fig. 3.12), the energy emitted by i is computed in deterministic manner with the forward optical path and the energy absorbed by i ($\tilde{P}_{ji}^{rea}$) is computed with the reverse optical path using Eq. 3.25, we have:

$$\tilde{P}_i^{ERM} = \sum_{j=1}^{N_v+N_s} \tilde{P}_{ji}^{rea} - \sum_{j=1}^{N_v+N_s} \tilde{P}_{ij}^{ea} \tag{3.47}$$

$$\tilde{P}_i^{ERM} = \sum_{j=1}^{N_v+N_s} \frac{P_i^e}{N_i} \sum_{n=1}^{N_{ij}} \left[\frac{L_{\nu,n}^0(T_j)}{L_{\nu,n}^0(T_i)}\right] \sum_{c=1}^{N_{pn}} \tau_{\nu,n}(B_{in}F_{jc}) - P_i^e \tag{3.48}$$

similar to Eq. 3.45, term $\tilde{P}_{ij}^{ea}$ can be written as:

$$\tilde{P}_{ij}^{ea} = \frac{P_i^e}{N_i} \sum_{n=1}^{N_{ij}} \sum_{c=1}^{N_{pn}} \tau_{\nu,n}(B_{in}F_{jc})\alpha_{\nu,jc} \tag{3.49}$$

According to Eq. 3.48, the statistical estimation of the radiative power in the cell i can be calculated as soon as all the optical paths originating from cell i have been generated. Thus, the exchange power at cell i in ERM model only depends the emission of cell i, the ERM allows accurate calculation of the radiative power in only one cell by simple allocating a large number of optical paths starting from this cell.

On the contrary, the same principe is used to calculate the exchanged power in cell i with the **Absorption Reciprocity Method (ARM)** (shown as Fig. 3.13), the energy absorbed by i is computed in deterministic manner with the forward optical path and the energy emitted by i is computed with the reverse optical path.

$$\tilde{P}_i^{ARM} = \sum_{j=1}^{N_v+N_s} (\tilde{P}_{ji}^{ea} - \tilde{P}_{ij}^{rea}) = \sum_{j=1}^{N_v+N_s} \frac{P_j^e}{N_j} \sum_{n=1}^{N_{ij}} \left[1 - \frac{L_{\nu,n}^0(T_i)}{L_{\nu,n}^0(T_j)}\right] \sum_{c=1}^{N_{pn}} \tau_{\nu,n}(B_{jn}F_{ic}) \tag{3.50}$$

Different from ERM, in ERM method, the statistical estimation of the radiative power in the cell i can only be calculated when all the optical paths originating from all the system cells j have been generated.

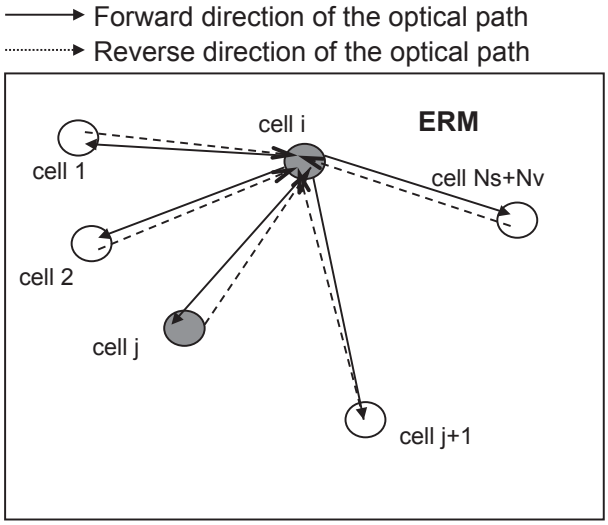

Figure 3.12 – *Emission Reciprocity Monte Carlo Method*

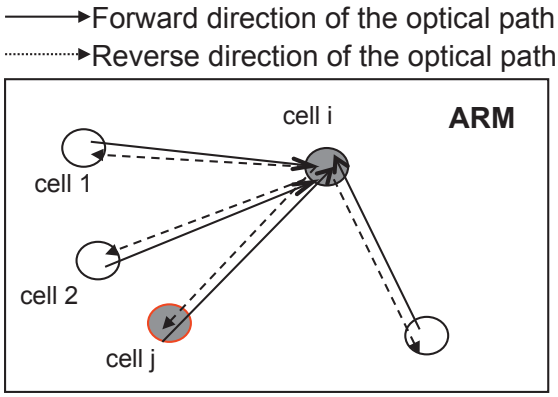

Figure 3.13 – *Absorption Reciprocity Monte Carlo Method*

Firstly, these two reciprocal Monte Carlo methods ERM and ARM are compared by their definitions. In ERM, energy emitted by cell i is calculated in a determinist way, and energy absorbed in cell i is calculated by the reciprocal path. Evidently, deterministic calculation is more accurate than reciprocal computation. So in this case, the energy emitted is better estimated than the energy absorbed. For the cells who have the higher temperature, emission energy plays a more important role than the absorption energy in the exchanged energy determination. Therefore, this method ERM must be more adapted for the zone with higher temperature. With the same reason, ARM should be more efficient for the cold zone.

The comparing results of these three methods can be resumed in Tab. 3.1.

Then, another optimized hybrid method (**Opimized Monte Carlo Method, ORM**) has been proposed by Dupoirieux et al. (2006) to overcome the drawbacks of ERM and ARM method by selecting to use one of them according to local conditions. If the temperature of the computing zone is high, ERM is used, on the contrary, ARM is used.

Finally, comparing these three reciprocal method in terms of computational performance. In ERM, the radiative energy in a given cell can be calculated only using the "information"

Monte Carlo Methods	Suitable cases	Disadvantages
FM	Optially thin media, semi-transparent media, characterized by important temperature gradients	Less efficient than ERM and ARM in the case with the large optical thicknesses or the weak temperature gradients
ERM	Zone with high temperature	-
ARM	Zone with low temperature	requirement of the complete information from all of the computational domain

Table 3.1 – *Comparison of the three Monte Carlo Methods, FM, ERM and ARM*

(energy emitted, absorptivity, etc.) from this cell, which allows to compute the radiative power of each cell of the computational domain independently. This advantage can be applied on some complex configurations to decrease the storage requirement. On the other hand, in ARM, to calculate the radiative energy in a given cell, the "information" from all of other cells in the computational domain must be required, which will certainly ask for more storage and will be difficult to be applied on some complex configurations. This disadvantage also exists in ORM.

In order to choose the best method for our coupling computing case between combustion and radiation, some tests with one dimensional flame(see chapter 4.2) have been carried out. The objectives are:

- Validating the numerical tools - Code ASTRE
- Choosing the best method among FM, ERM, ARM and ORM according to their results in terms of the physical behavior and computational perfomance
- Defining the best suitable parameters for the following three dimensional calculations.

Chapter 4

Monte Carlo numerical solver

Table of contents

A three dimensional parallelized code (ASTRE) developed by ONERA and EM2C is used here as radiation solver (Tesse et al. 2002; Dupoirieux et al. 2006; Tesse et al. 2004). Four Monte Carlo formulations FM, ERM, ARM and ORM are implemented (Tesse 2001) to calculate the radiative power and the radiative flux with unstructured grids. Additionally, many complex physical phenomena can also be treated in this solver such as the effect of soots. Concerning the gas radiative properties, the CK model, the SBPM model or the line by line model are available (Tesse 2001).

Firstly, in order to choose the most suitable Monte Carlo formulation for our specific simulations, the one dimensional flame test case is presented in section 4.1. Then two techniques to improve the performance of ASTRE code are discussed in section 4.2. Finally, based on these results, a new three dimensional Monte-Carlo solver (Rainier) specially dedicated to coupled simulations between combustion and radiation will be described in section 4.3.

4.1 Validation of Emission Reciprocal Monte-Carlo Method (ERM) with 1D flame using ASTRE

4.1.1 Description of the test case

Numerical configuration

To compare the four Monte Carlo formulations (FM, ERM, ARM and ORM) in the context of combustion processes, simulations of a one-dimensional premixed laminar flame are performed using ASTRE solver.

The simulated configuration is displayed in Fig. 4.1. A non-isothermal, emitting and absorbing medium is enclosed between two parallel infinite isothermal semi-reflecting opaque walls perpendicular to x-axis (in order to simplify the promblem, the emissivity is supposed equal to 1 in this chapter). The computation slab has a dimension of $0.1\ m \times 0.0004\ m \times 0.0004\ m$ (x, y, z) with 16 000 hexahedron cells. The grid size of this mesh is constant and equal to $\Delta = 0.1\ mm$ in all of the computational domain. To simulate the infinite transverse dimension of the 1D benchmark along the y and z axis, four lateral faces of this slab are considered as four symmetry boundary conditions. A premixed propane/air flow is injected from the inlet at the location of $x = -0.05\ m$ with an upstream mean velocity of about $0.48 m/s$ and an equivalence ratio $\phi = 1.0$. The pressure at the outlet boundary of the computation domain is imposed as 1 bar. The flame front is defined near the center of this cube.

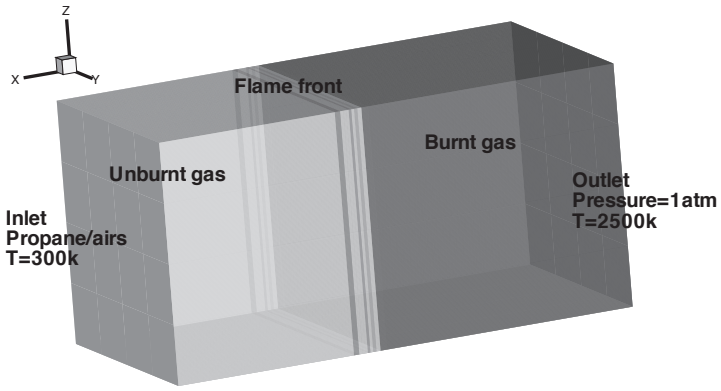

Figure 4.1 – *Geometry of 1D flame with grid size 0.1mm*

Combustion and radiative transfer modeling

As mentioned in section 2.3.2, the Thickened Flame (TF) model has been used here to resolve the flame fronts. Later in this chapter, some detailed discussions will be given about the impact of this model on the radiative results with the different artificial thickening factors. To avoid the uncertainties coming from this model in the present test cases, we choose a thickening factor $F = 1$ and a grid size of mesh $\Delta = 0.1mm$ that is small enough to accurately describe the flame front. An usual laminar flame is then computed.

Concerning the chemical aspect, a one-step global chemical mechanism is chosen to represent the reaction between propane and air (Selle et al. 2004).

$$C_3H_8 + 5O_2 \longrightarrow 3CO_2 + 4H_2O \tag{4.1}$$

The corresponding reaction rate is given by:

$$\dot{\omega} = A[C_3H_8]^{\alpha}[O_2]^{\beta} \exp(-E_a/RT) \tag{4.2}$$

where $[C_3H_8]$ and $[O_2]$ denote the molar concentration of species C_3H_8 and O_2, the corresponding exponents α and β are respectively 0.856 and 0.503, the pre-exponential factor A_i can be adjusted according to the test cases, more details about this parameter will be discussed in the next paragraph. The activation energy E_a is 31126 $cal.mol^{-1}$ and T is the absolute local gas temperature. With these chemical parameters, a laminar flame speed $S_L^0 = 0.48\ m/s$ is obtained for a equivalence ratio $\Phi = 1.0$.

In the version of AVBP used here, the chemical scheme provided to describe the propane-air chemistry uses different Schmidt numbers for each species. These different Schmidt numbers introduce preferential diffusion in the flame front and can lead to large variations of the ratio between CO_2 and H_2O mass fractions. This effect is highly amplified when the Thickened Flame model is used. Although it can be negligible if we only focus on the flame dynamics, it will lead to large error when dealing with radiation. Because CO_2 and H_2O are the two major absorbing species in the flame, and their proportions are crucial to accurately estimate the radiative power in the flame. So in this dissertation, the Schmidt numbers have been set to an unique value for all the species. To simplify the computation, the same flame speed S_L is conserved and the pre-exponential factor A is adjusted (Goncalves Dos Santos 2008), the value used here is $3.162 \cdot 10^{10}$ (cgs). With all of these combustion parameters, Fig. 4.2 shows the converged results of laminar flame obtained by AVBP.

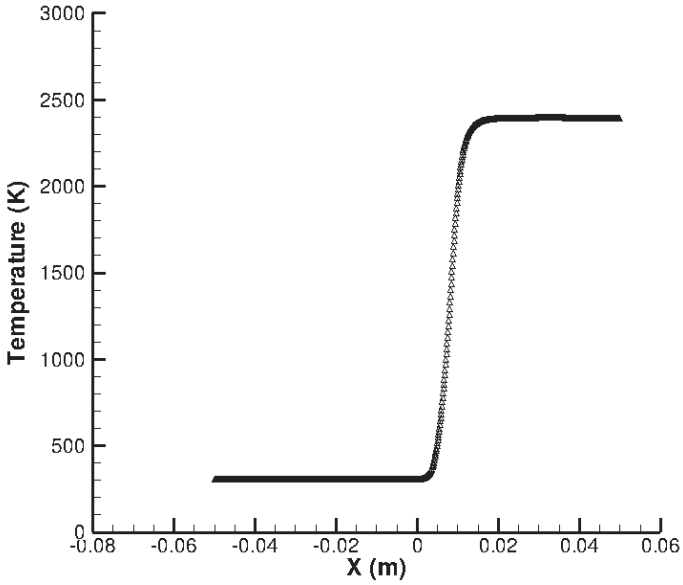

(a) Temperature profile

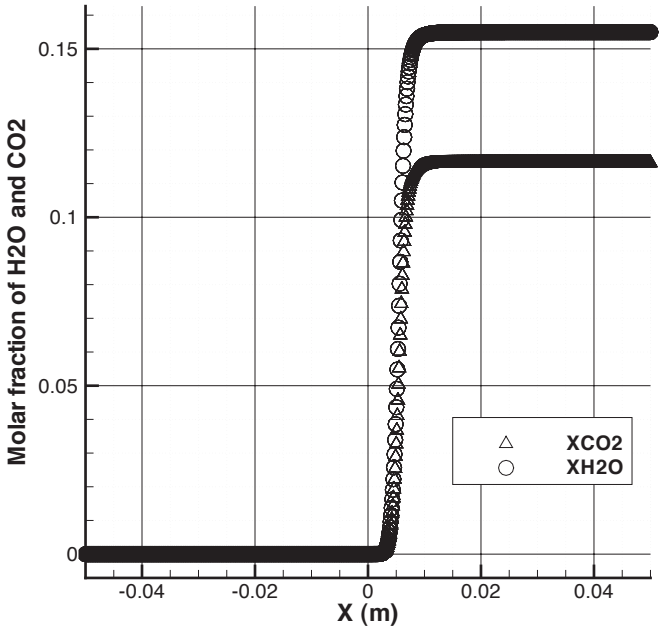

(b) Molar fraction of CO_2 and H_2O profiles

Figure 4.2 – *Temperature, X_{CO_2} and X_{H_2O} profiles of flame 1D modeled with AVBP*

Gas radiative properties are treated in a correlated manner by a correlated-k (CK) model which was firstly generalized for reactive applications by Rivière et al. (1992) and the database was developed by Soufiani and Taine (1997) More details about this model will be presented in Appendix A.1. Among all of the species, only H_2O and CO_2 have been taken into account in the absorbing medium. 44 joined spectral bands with variable width are considered for H_2O (from 150 cm^{-1} to 9200 cm^{-1}) and 17 spectral bands for CO_2 which are overlapping H_2O bands. Additionally, a 7-points Gauss quadrature for each gaseous

component is used. That leads to 1022 pseudo-spectral points as show below[1].

$$\overbrace{(44-17)}^{H_2O \text{ bands no overlapped by } CO_2} \times \underbrace{7}_{a} + \overbrace{17}^{H_2O \text{ bands overlapped by } CO_2} \times \underbrace{7}_{b} \times \underbrace{7}_{c} = 1022 \tag{4.3}$$

To simplify the computation, the emissivity is supposed equal to unity both at the inlet and outlet, that means all the radiative arriving rays are totally absorbed. The temperature of the outlet is equal to T_{BG}, where T_{BG} is the burnt gas temperature, while T_{inlet} is set equal to 300 K. Furthermore, all the cases tested here correspond to an optically thin medium.

Finally, the random number generator used in this thesis is a combined multiple recursive generator developed by L'Ecuyer (1999). It has been tested in the Ph.D thesis of Tessé (2001), observing that results are not sensitive to this generator.

4.1.2 Resultats and discussions

The radiative power of this 1D flame has been computed using the ASTRE code . Noting that here two transformations have been made to link AVBP and ASTRE results, species mass fractions used in combustion code are transformed into molar fractions used in radiation code and physic parameters expressed at nodes with AVBP are interpolated to be expressed at the cell centers with ASTRE.

Besides of the converged results for each quantity at each cell, Monte Carlo method also gives access to the standard deviation σ which shows and controls the convergence:

$$\sigma(i) = \sqrt{\frac{\sum_{j=1}^{N_b}(\overline{A_i} - A_{ij})^2}{N_b}} \tag{4.4}$$

in order to adapt to the parallel computations and simplify the standard deviation calculations, the total optical rays generated from cell i was divided into N_b beams (also called "little computations"), the notation "beam" is a group of the optical "rays", for example, beam j contains N_j optical rays and the total optical ray generated from cell i is $N_b \cdot N_j$. For each beam j, a mean radiative power A_{ij} is computed by using the radiative power of the N_j optical rays:

$$A_{ij} = \frac{\sum_{k=1}^{N_j} A_{ik}}{N_j} \tag{4.5}$$

then the variance of this Monte Carlo calculation is obtained by computing the standard deviation of the radiative power of all these optical beams. More detailed description of this technique has been presented in Dupoirieux et al. (2006). $\overline{A_i}$ is the mean value among these N_b beams being written as :

$$\overline{A_i} = \frac{\sum_{j=1}^{N_b} A_{ij}}{N_b} \tag{4.6}$$

The radiative power presented in the following figures is this mean value $\overline{A_i}$.

[1]Term a represents 7-points Gauss quadrature for H_2O concerning the bands no overlapped by CO_2, term b represents 7-points Gauss quadrature for H_2O concerning the bands overlapped by CO_2 and term c represents 7-points Gauss quadrature for CO_2

Influence of the optical paths' number

The influence of the number of the optical paths on the convergence of Monte Carlo Method has been firstly studied. The minimum optical path number departing from each cell in order to get converged results is determined.

Two spatial distribution techniques have been developed to define the number of the optical paths generating from each cell. One is NUD characterizd by a NON-uniform Spatial Distribution of the optical path in the calculation domain, the ray number N_i generating from cell i is proportional to the radiative power emitted by cell i. The other one is Uniform Spatial Distribution (UD), which applies the same ray number to all the cells.

UD is chosen for the following computations in this thesis because NUD has several shortcomings which are not adapted to our coupling case.

- According to Tessé et al. (2002), the reciprocal Monte Carlo methods like ERM or ARM are very sensitive to the spatial distribution of optical paths. With the principe of NUD, the radiative energy emitted by the cell located in the cold zone is small, so only a few optical paths are generated from this cold region, so the computations are difficult to converge. For ERM method, the absolute value of the radiative power emitted in the cold zone is small, so the fact that only a few optical paths are generated could be considered as not very important. However, for ARM method, the absolute value of the radiative power absorbed in the cold zone is important, the fact that only a few optical paths are generated will lead to convergence difficulties. So NUD is not acceptable in this case.
- In the coupling between combustion and radiation, flame structure changes after each iteration of combustion (or several iterations), so the temperature profile changes, the radiative power also changes. If NUD is used, as the ray number drawn from each cell is proportional to the local radiative power, it must be re-defined at each iteration (or several iterations), which might induce the computation inefficiency in terms of CPU time. So UD adapts better in our coupling case.

Fig 4.4 shows the standard deviation of ERM model with the different ray numbers generating from each cell. Fig 4.3 shows the corresponding radiative power (mean value) for each case. The standard deviation decreases when the ray number increases. In addition, Tab. 4.1 shows evolution of the ratio (order of magnitude) between the standard deviation and the maximum radiative power for each case, evidently this ratio also decreases when the ray number increases.

Total ray number N	Ratio=standard deviation/maximum radiative power
10^2	$\sim 10\%$
10^3	$\sim 0.2\%$
10^4	$\sim 0.067\%$
10^5	$\sim 0.02\%$

Table 4.1 – *Ratio (order of magnitude) between the standard deviation of Fig. 4.4 and the maximum radiative power of Fig. 4.3 for different ray number cases*

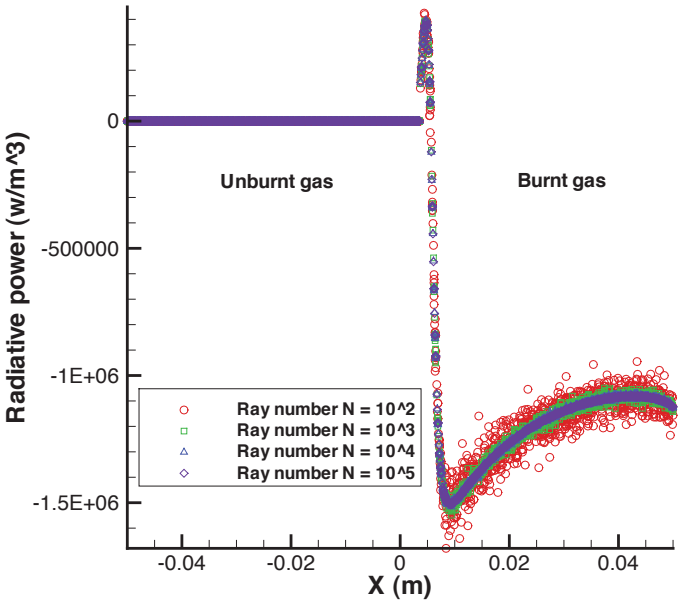

Figure 4.3 – *Comparison of the radiative power with different ray numbers displayed as a function of the optical coordinate, ERM model, grid size = 0.1 mm, flame 1D, here ray number N = ray number per beam × beam number (N_b)*

According to the law of large numbers (LLN) in probability theorem, the convergence of Monte Carlo method can be defined by this following way: if the standard deviations of a series of random variables composed by N independent individuals decrease according to the law $1/\sqrt{N}$, this computation is converged. For example, in our test, for each cell, in each beam, ray numbers N_j are separately chosen as 20, 200, 2 000 and 20 000, the number of beams (little computations) is $N_b = 5$ for every cell. Fig. 4.5 shows the comparison between the mean standard deviation computed and the reference standard deviation $(1/\sqrt{N})$. The minimum ray number N which can make this Monte Carlo computation converged is determined as 10^4 (2000 ray numbers per beam and 5 beams considered), it will be used in the following calculations of this chapter. Please note that in every figure below in this chapter, N represents ray number per beam × beam number (N_b).

Although all of the above results are shown with ERM model, these tests have also been performed with FM, ARM and ORM models. Because in the following discussion, we will find that ERM is the most suitable model for our computation cases, only the results of ERM are shown, but other models display the same behaviour.

Comparison among FM, ERM, ARM and ORM methods

The comparison among the four models FM, ERM, ARM and ORM have been studied in terms of mean radiative power and standard deviation, as illustrated in Fig. 4.6, Fig. 4.7 and Fig. 4.8.

In the isothermal fresh gas zone, where the mass fraction of CO_2 and H_2O are equal to 0, there is no absorption energy. Near the low temperature side of the flame front, absorption

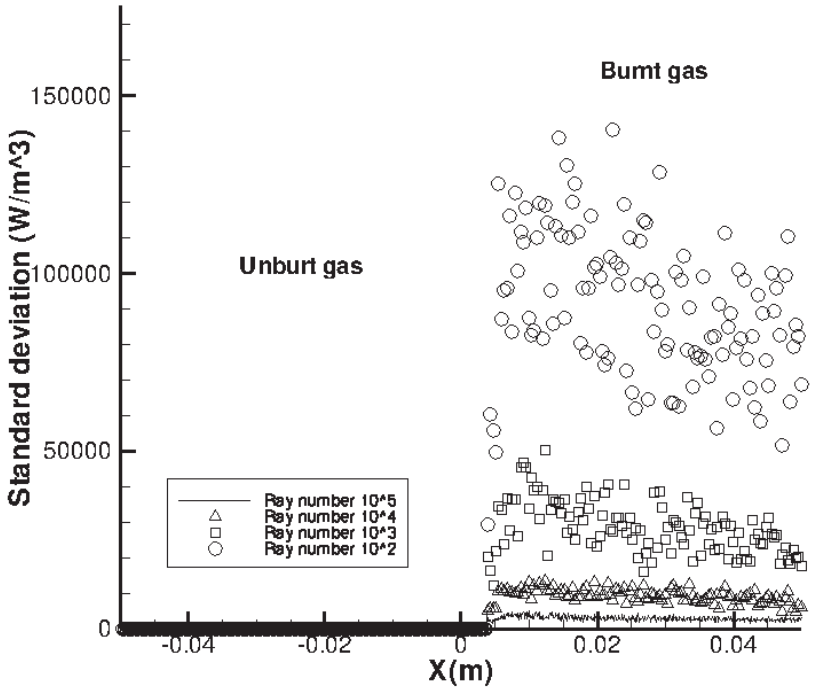

Figure 4.4 – *Comparison of the standard deviations with different ray numbers displayed as a function of the optical coordinate, ERM model, grid size = 0.1 mm, flame 1D, here ray number N = ray number per beam × beam number (N_b)*

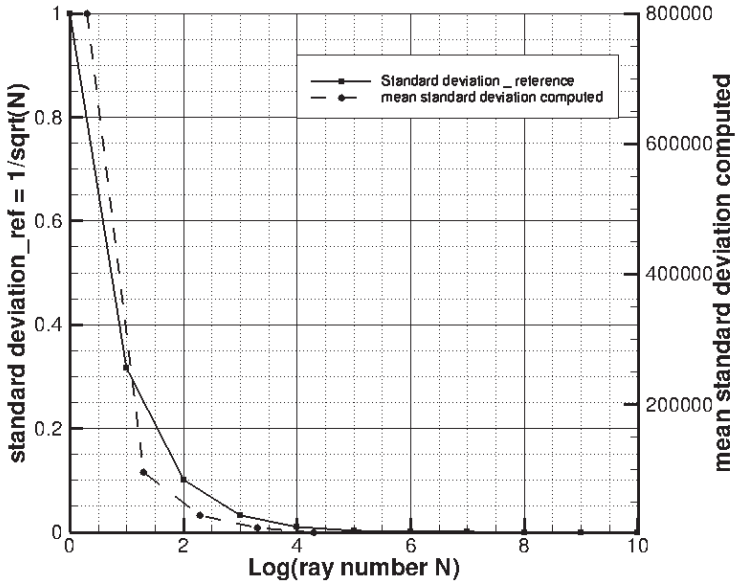

Figure 4.5 – *Determination of the minimum ray number for a converged result in the test case, ERM model, grid size = 0.1 mm, flame 1D, log means log_{10}*

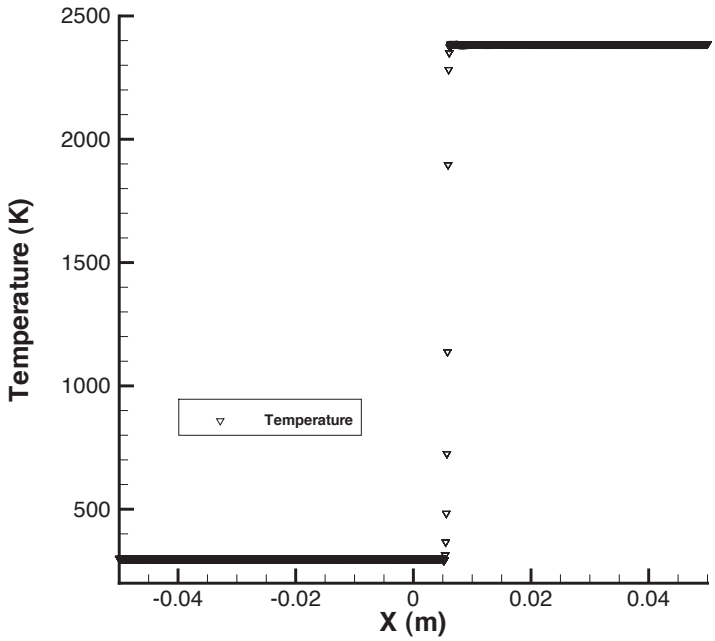

(a) Temperature

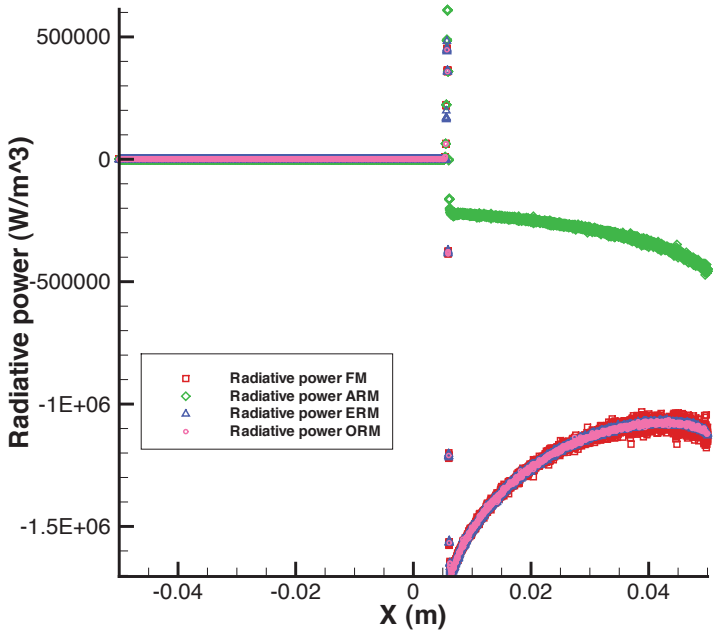

(b) Mean radiative power

Figure 4.6 – *Temperature and mean radiative power of the 1D flame with different reciprocity models of Monte Carlo Method, thickness factor=1, grid size=0.1 mm, number of the optical paths=*2000*/cell,* $N_b = 5$

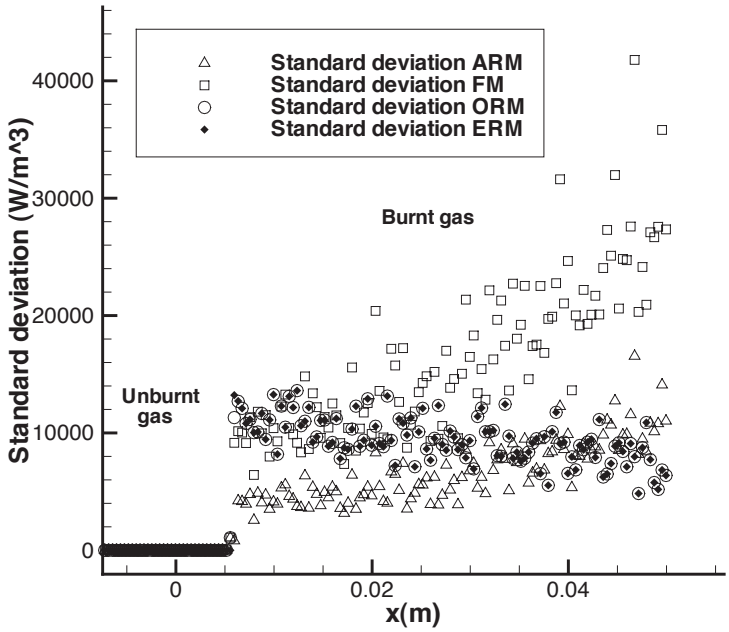

Figure 4.7 – *Standard deviation of the 1D flame with different reciprocity models of Monte Carlo Method, thickness factor=1, grid size=0.1 mm, number of the optical paths=*2000*/cell, $N_b = 5$*

energy appears dominant due to the CO_2 absorption bands at 600 K. Because of the large temperature gradient, the modulus of the radiative power gets a maximum value in the high temperature part of flame front, before decreasing in the isothermal burnt gas zone. In the present simulation the outlet temperature has been set equal to 2400 K and the related emissivity equal to 1, so the boundary condition can be considered as an infinite extension of the burnt gas region. Furthermore, it is important to notice that the mean radiative powers calculated with FM, ERM and ORM completely superimpose in all of the computation domain except that FM presents more fluctuations near the boundary.

The ARM model does not give a satisfying result in the hot region (Fig. 4.6). Referring to the ARM formulation, it calculates the emission power indirectly and the absorption power directly. Because CK model is used here as the radiative properties models, and in this model, the optical paths are generated in function of the local emission power (please see the Appendix A.1 for more details). For one cell i in the hot zone, the fact that the emission power is calculated indirectly means the optical paths used are generated in function of the emission power of the cells different of this cell i, probably in the cold zone. Therefore, the number of optical paths generated are limited and the computations are difficult to be converged. In the same time, for cell i in the hot zone, the emission is the dominant phenomenon to exchange the energy compared to absorption, absorbed power is low, so if the emission power can not be accurately calculated, the radiative power equal to absorption power minus emission power will not be correctly modeled.

Since the performance of Monte Carlo method is defined as the product of the computation time t and the variance σ^2 (Farmer and Howell 1998), the comparison of the standard

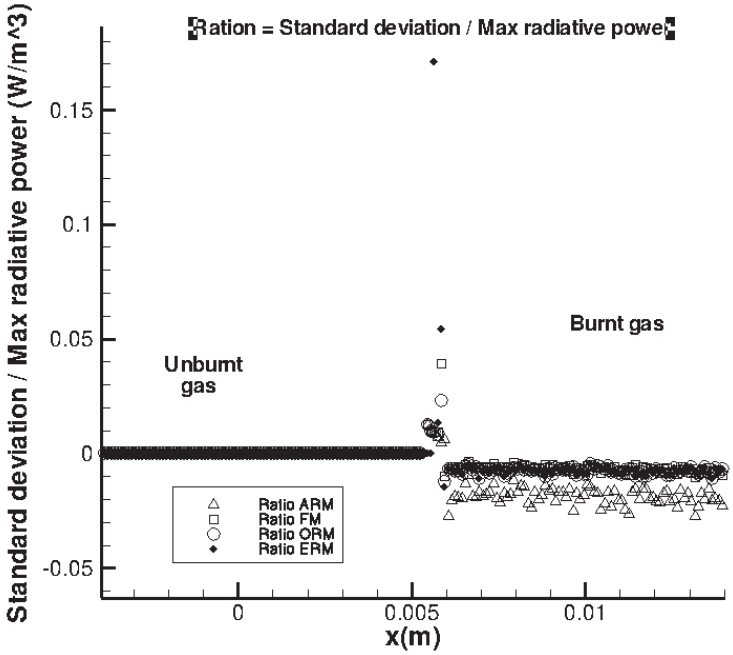

Figure 4.8 – *Ratio between the standard deviation and the maximum radiative power of the 1D flame with different reciprocity models of Monte Carlo Method, thickness factor=1, grid size=0.1 mm, number of the optical paths=*2000*/cell,* $N_b = 5$

deviations σ obtained from the different approaches is then significant. In our test, the effect of σ has been observed with the same simulation time. As shown in Fig. 4.7, obviously, ERM, ORM, ARM and FM provide nearly the same standard deviation levels in the flame front, while ERM, ORM and ARM converge more quickly than FM in the burnt gas region which corresponds to the fact that reciprocal model is more efficient in isothermal medium.

Furthermore, several remarks from the point of view of the computational time and the storage requirement. Firstly, as mentioned in Chapter 3, calculating the radiative power of one cell with ARM model needs to store the information of all the cells in the computational domain in order to calculate the absorption power from other cells, but ERM only needs to store the information of the cell calculated itself (ex: $\sim 20MB$ needed by ERM and $> 200MB$ needed by ARM). Secondly, in ERM, any part of the computational domain can be calculated independently, this characteristic will be very useful for some complex configurations, because we can just choose to calculate the parts of the domain of interest or where radiative transfer are significant , and it will spend less time than computing all the domain. Finally, although ORM has almost the same result as ERM in the precedent tests, it is a mix of ERM (in the hot region) and ARM (in the cold region), so the same storage problem must exist in ORM.

To summarize, ERM has been considered as the most suitable model for the following computations.

Influence of the mesh size

The influence of the grid size has been studied in this part. Two different meshes have been used respectively for combustion and radiation simulations in this work because these two phenomena have not the same constraint in terms of mesh sizes.

On one hand, the combustion code asks for a mesh with the grid small enough in order to obtain more accurate results in the flame front. On the other hand, the radiation solver does not always need so small size mesh, which may depend on the gradient of the temperature and molar fractions. Furthermore computations are not very efficient if the mesh size is too small. For Monte Carlo method, every time the optical path crosses a new cell, it will exchange the energy with the local medium. It means that the Monte Carlo solver needs to compute the coordinates of the intersection point and the local absorption. Therefore, the grid size of the cells (for a constant computational volume larger cells leads to a smaller number a of cells) and the total number cells will largely influence the efficiency of the radiation code.

In this section, simulations are presented to check the impact on the predicted radiative field, of using a coarser mesh in the radiation solver. If the error, introduced by this coarser mesh, remains low, a merging mesh technique may be used to optimize the performance of the radiative code reducing the storage requirement and CPU time.

To perform these validation simulations, the same physical parameters have been used. The mesh previously presented, with the grid size equal to 0.1 mm, is retained as the reference mesh and a second mesh with a grid size equal to 0.5 mm is used as the coarser mesh. In order to conserve the same temperature profile and the same molar fractions of CO_2 and H_2O on both meshes, an interpolation has been performed in the flame front from the reference mesh into the coarser mesh (The interpolation is used for the general case. In the actual test case, one cell in coarser mesh corresponds 5 cells in the reference mesh).

As shown in Fig. 4.9 and Fig. 4.10, the two cases present a good agreement in most computation domain when focussing on the mean radiative power, or on the standard deviation. A zoom in flame front Fig. 4.11 makes evident that using a coarser mesh artificially omits some important points so that the radiative power in flame front is not accurately reproduced. Additionally, the medium in the computations cells with larger size is less homogeneous, which will lead to a slower convergence. That is why a significant standard deviation has appeared in the flame front of Fig. 4.11. So attention must to be paid in flame front if we want to merge the meshes, the subject of "merge" will be discussed in the section 4.2.1.

Influence of the thickening factor

As already indicated at the beginning of this chapter, the influence of the artificial thickness factor of the Thickened Flame model on the radiative results are studied.

In fact, in laminar flows, the Thickened Flame model is applied to resolve the reactive zone using an Arrhenius law without changing the laminar flame speed while its thickness δ_L^0 is multiplied by the factor F (Butler and O'Rourke 1977). In turbulent flows, eddies smaller than $F\delta_L^0$ do not interact with the flame any longer, as a result, the thickening of the flame reduces the ability of the vortices to wrinkle the flame front, then the flame surface is

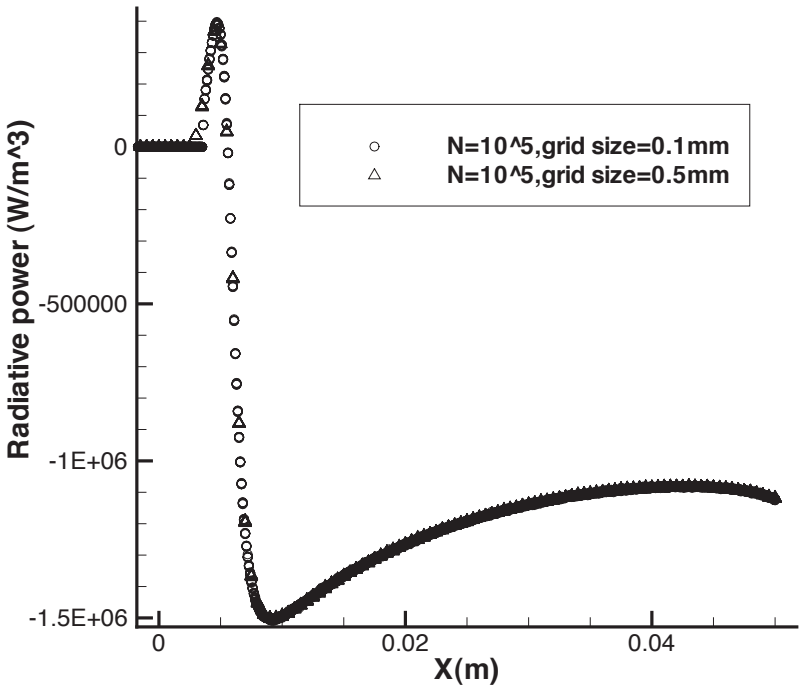

Figure 4.9 – *Comparison of the radiative power with the different grid sizes, 1D flame, ERM model, grid size=0.1 mm, 0.5 mm, number of the optical paths=*2000*/cell,* $N_b = 5$

reduced, the reaction rate is underestimated. In order to correct this effect, an efficiency function ε has been developed from DNS results and implemented into AVBP (Schoenfeld 2008). The model then describes a flame front of thickness $F\delta_L^0$ propagating at the turbulent flame speed εS_L^0 where S_L^0 is the laminar flame speed.

Nevertheless, the thickening operation changes the profiles of the temperature and the mass fraction of all the species in the flame front and modifies the radiative power and fluxes in the radiation simulations. As shown in Fig. 4.12, three flames with different thickening factors produce different radiative powers in the flame front. To quantify this numerical error more clearly, integrations of the emission power and the absorption power are separately calculated within the interval [-0.05 m,0.05 m] of x, as illustrated in Tab. 4.2.

Physically, emission and absorption powers should be the same for these three cases, but Tab. 4.2 shows that it is not true in our simulations. The maximum value of emission power (or absorption power) is decreased when the thickening factor increasing (the maximum value in case $F = 1$ is larger than other two cases). The integration of the absorption power when $F = 20$ is larger than other two cases. As a result, in order to avoid this kind of error, when $F \neq 1$ (grid size is not small enough in flame front), a correcting factor is needed. Considering that the error is lower than 3% ($F = 1, 10$), this correcting factor will not be studied in this thesis, it might be discussed in following Ph.D studies.

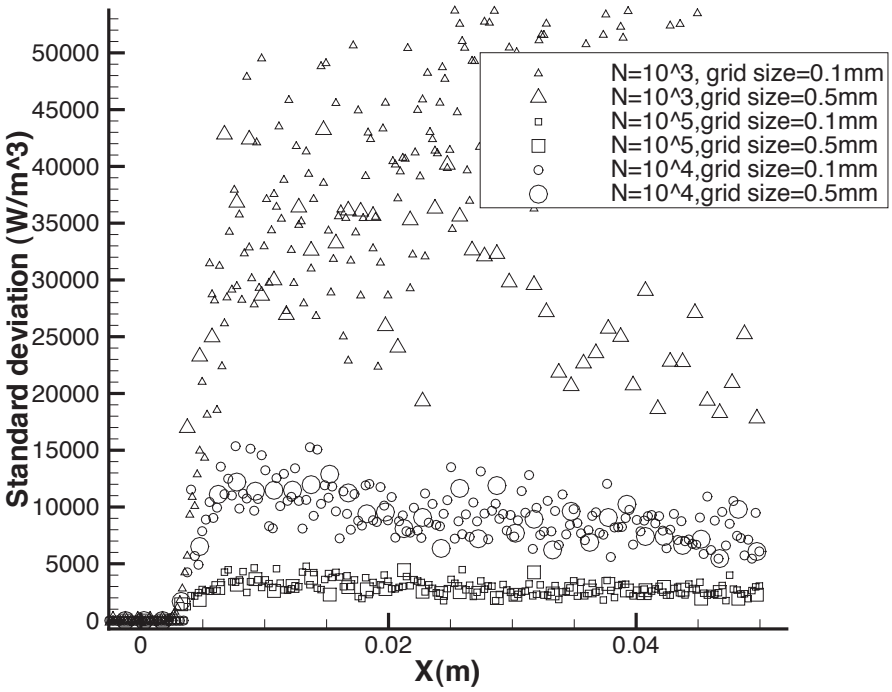

Figure 4.10 – *Comparison of the standard deviation with the different grid sizes, 1D flame, ERM model, grid size=0.1 mm, 0.5 mm, number of the optical paths=*2000*/cell, $N_b = 5$*

Thickening factor F	Absorption power (W/m^3)	Emission power (W/m^3)	Radiative power (W/m^3)	divided by radiative power in case of F=1
1	99.3	- 53884	-53784.7	1
10	547.0	- 52939	-52392	0.9741
20	996.2	- 48603	-47606.8	0.8851

Table 4.2 – *Integrations of the radiative power for the three different thickening factors*

4.1.3 Conclusions

Test cases of 1D flame have been performed by using the radiation code ASTRE with gas medium characteristic of a flame. Some significant parameters for Monte Carlo method like the number of rays or the convergence have been discussed. After the comparison of four Monte Carlo models , ERM model is considered as the most suitable model for our following coupling computation both from a physical point of view and a numerical point of view. Comparing results with the different grid size shows that it could be efficient to develope a new technique to merge the meshes which will be presented in section 4.2.1. Due to the use of the thickening factor of Thickened Flame model for combustion simulation, numerical error may appear in the radiation results. In order to avoid this kind of error, a correcting factor might be needed for coupling computation (this factor will not be studied

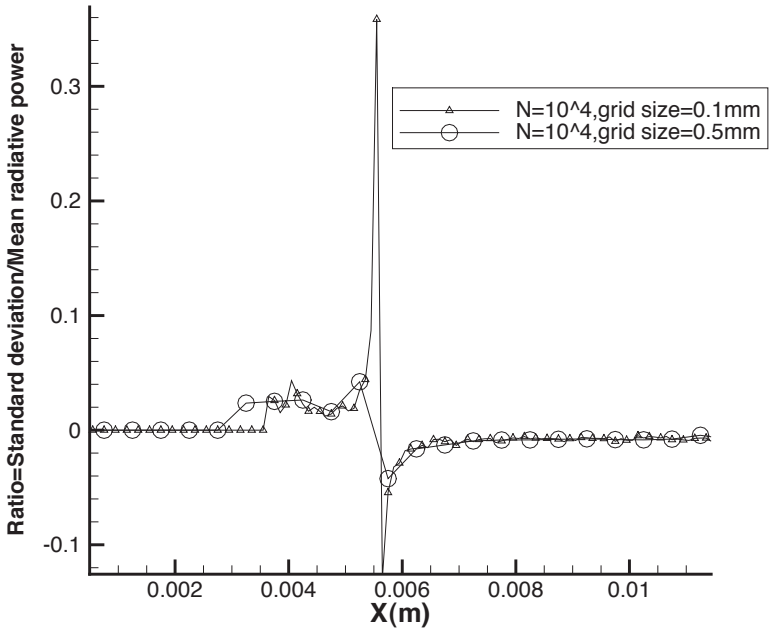

(a) Total optical path number = 10^4

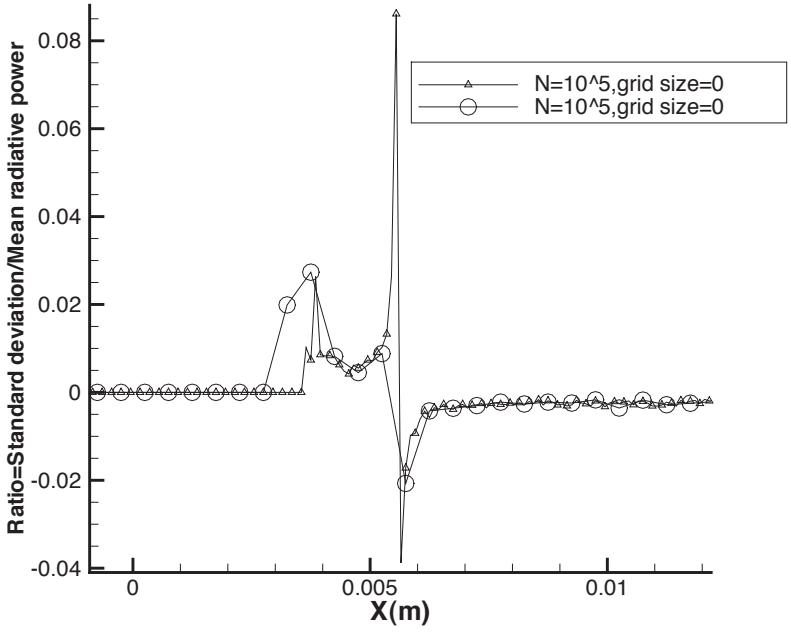

(b) Total optical path number = 10^5

Figure 4.11 – *Comparison of the ratio between the standard deviation and the radiative power$_{max}$ with the different grid sizes, flame 1D, ERM model, grid size=0.1 mm, 0.5 mm, number of the optical paths=*2000*/cell, $N_b = 5$*

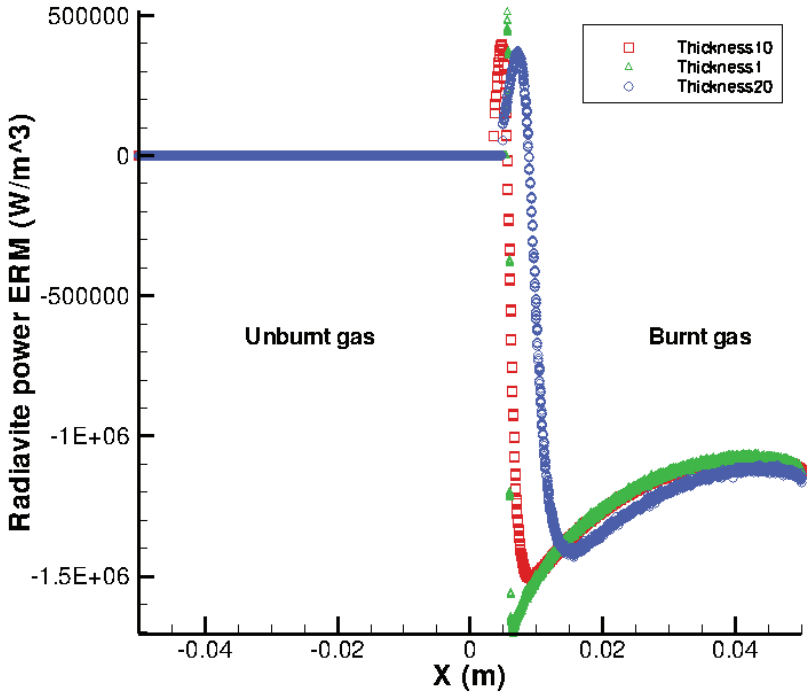

Figure 4.12 – *Comparison of the radiative power with the different thickness factors, flame 1D, ERM model, thickness factor=1,10, 20 grid size=0.01 mm, number of the optical paths=*2000*/cell,* $N_b = 5$

in this thesis, it might be developed in following thesis at EM2C laboratory).

4.2 Improvement of ASTRE code's performance

As discussed by some studies realized recently, asking for huge CPU time and memory is one of the disadvantages of Monte Carlo methods which will restrict their application in actual industrial cases. In this section, a test case applying on a mesh with 2 700 000 cells will be presented, the performance evaluation of ERM model directly using ASTRE code shows that the computational cost is so expensive that it will not be acceptable for coupling. In practice, to get the converged results, 16 hours computation and 4.8G total storage with 5 processors are needed on computer SGI Altix350. The details of this test configuration will be described later. So two tools to improve the performance of the ASTRE code have been developed and will be detailed in this chapter.

4.2.1 "Grid merge" method

Principe of the method

Numerically, the radiation code does not need meshes as fine as those required in combustion simulations using LES model. Additionally, ASTRE code can deal not only with structured meshes like the tetrahedron and hexahedron but also unstructured meshes especially including multi-face cells. A "grid merge" technique which combines a large number of cells together according to certain rules to reduce the number of cells is developed. The objective is to reduce the computational time and the memory without changing the final results of radiative simulation.

Firstly the criterion according to which the grid is merged is discussed. The radiative power is calculated basing on three parameters coming from results of the combustion code, which are respectively the temperature, the mass fractions of CO_2 and H_2O. To simplify the problem, only the temperature has been chosen as the criterion here. As illustrated in Fig. 4.13, the merge process is that:

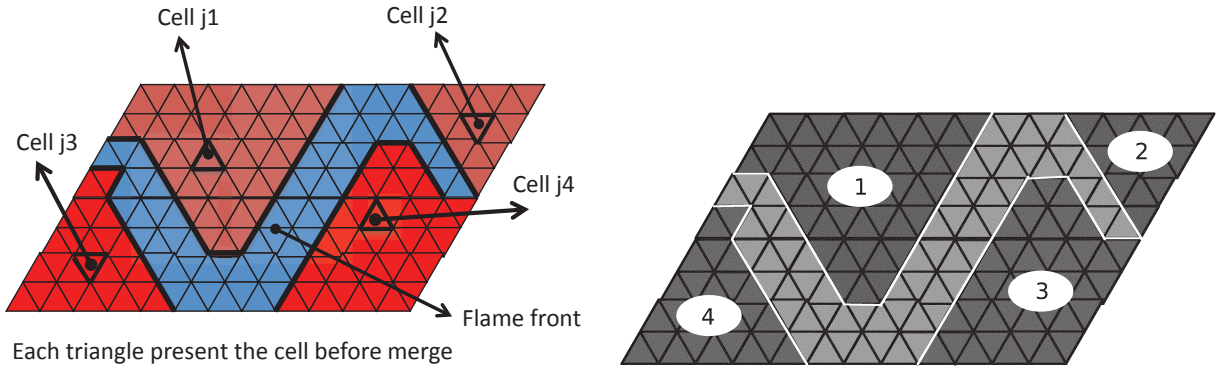

(a) Before merging, cells j1, j2, j3 and j4 are chosen as the original cell j

(b) After merging, new merged grid cell 1, 2, 3 and 4 are generated from the original cells j1, j2, j3, and j4

Figure 4.13 – *Principe of the grid merge. In the flame front where high temperature gradient exists, the original small grid is conserved. In the burnt gas zone and unburnt zone which are almost isothermal, the new merged grid has been generated like cell 1, 2, 3, 4 as illustrated in this figure.*

1. Pick up one cell j in the computational domain ($j = 1, \cdots N$, with N is the total cell number) and this cell has N_j faces.
2. Test if cell j has already been merged, if not continue to do step 3, else return to step 1 and pick up another cell.
3. Pick up cell i next to cell j, here "next to" means that these two cells have a common face (with $i = 1, \cdots, M_j$, and M_j is the number of the cells next to cell j, and cell i has N_i faces). Then compare the temperature of cell j and cell i, if $\mid T_j - T_i \mid \leq \Delta T$ (where the choice of the merge criterion ΔT will be discussed later), then cell j and cell i will be merged by deleting the common face between them, the new cell $j\prime$ has $\mid N_j + N_i - 2 \mid$ faces noted as $NF_{j\prime}$.

4. Repeat step 3 for all of the cell i next to cell j as long as the total faces number $NF_{j\prime}$ is less than (or equal to) a fixed value N_{mf}. N_{mf} can be considered as a precision control parameter which will be discussed later. We can also choose the total merged cell number as the precision control parameter, but for our code, N_{mf} is easier to implement.

5. If all of the cells next to cell j have been merged and the total faces number of the new cell $j\prime$ - $NF_{j\prime}$ is still less than N_{mf}, then treat the cell $j\prime$ by the same method like that for cell j as mentioned in step 3, that means testing all of the cells next to the new cell $j\prime$ until the total faces number $NF_{j\prime}$ is equal or more than N_{mf}.

6. The new merged cell has the same value of temperature, mass fraction of CO_2 and H_2O as the original cell j.

7. Repeat step 1 for all of the cell j in the computational domain.

In order to use the new merged grid with multi-face cells, some modifications have been carried out in ASTRE code:

- In the case without merging, the optical ray is generated from the center of the cell for optically thin cells and is generated randomly for optically thick cells. After merging, the shape of some new cells is no longer regular, so their centers might not be located inside the cells. For this reason, optical rays are generated randomly for these cells.

- Changing some algorithms in ASTRE code to make sure that it works well with the concave merged grid. Because in the original version of ASTRE code, the determination of the direction of the face vector between two neighboring cells depends on the mass centers of these two cells. For example, as shown in Fig. 4.14, cell 1 is the cell "upsteam" and cell 2 is the cell "downsteam", the vector from the mass center of cell 2 to the mass center of cell 1 is noted as $\overrightarrow{O_2O_1}$, the direction of the face vector from the cell "upsteam" to the cell "downsteam" noted $\overrightarrow{n_{12}}$ should respect the relation $\overrightarrow{O_2O_1} \times \overrightarrow{n_{12}} < 0$. But after cell merging, some deformed concave cells might be produced, due to the shape deforming of the concave cell 2, the position of mass center is changed, the direction of the vector $\overrightarrow{O_2O_1}$ is then reversed, it will then have the problem. In the new version, all the deformed concave cells will be detected and their face vector directions will be corrected.

Test cases and discussions

In this part, some tests being carried out with a one-dimensional laminar premixed flame case and a swirled gas turbine injector case are presented to validate this "grid merge" method by quantifying the reduction of CPU time and memory achieved with this tool.

1D flame case

The test is performed with the configuration used in section 4.1. Numerical parameters are summarized in Tab. 4.3:

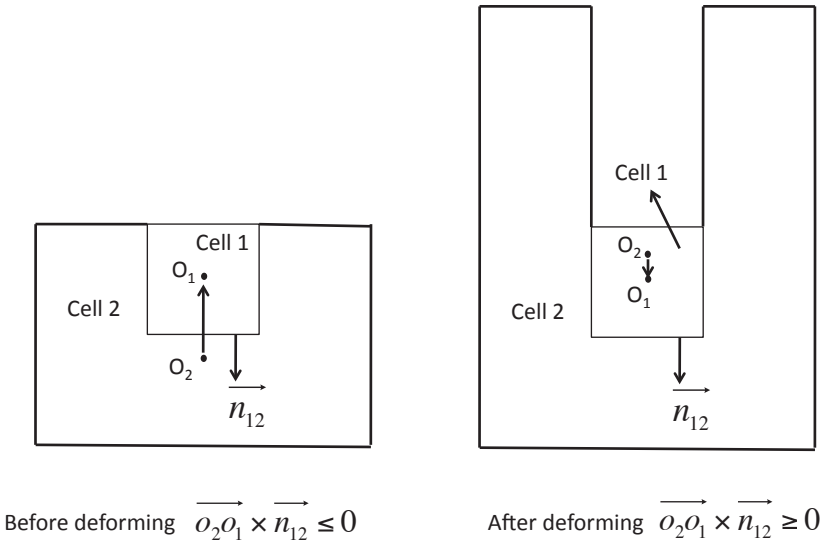

Figure 4.14 – *Problem of the determination of the face vector direction for deformed concave cell in ASTRE*

Thickening factor	Optical paths distribution	Original minimum grid size
1	Uniform Spatial Distribution	0.1mm

Table 4.3 – *Numerical parameters for grid merge computation*

Subsequently the influence of two characteristic factors for grid merge, which are respectively the maximum face number allowed for the new merged cells, N_{mf}, and the temperature criterion used for merging, ΔT, has been studied. Because of the independence of these two factors, their influence can be investigated separately.

Firstly, with $\Delta T = 1K$, we test the relation between the new cell number N_{cell} after merging and the maximum face number allowed per cell N_{mf}. As shown in Fig. 4.15 (16000 cells without merge), at the beginning, N_{cell} decreases quickly when N_{mf} increases. If N_{mf} is more than 200, the number of merged cells do not decrease any more when the maximum face number merged increases, which means that all of the cells with $\Delta T = 1K$ have been nearly combined. According to this test, $N_{mf} = 200$ is chosen.

In order to verify this merging criterion, several computations to show the improvement of Monte Carlo method performance were accomplished. As defined by Farmer and Howell (1998) the "performance" of various Monte Carlo computations is the product of run time t and variance σ^2 of the solution, or

$$Performance = \sigma^2 \cdot t \tag{4.7}$$

σ is kept constant for the different calculations with the different optical paths numbers as illustrated in Fig. 4.16, then the performance only depends on the CPU time t. As shown in Fig. 4.15, the similar evolution for the variation of the computation time t and the new cells number after merging was obtained, which means that both of these two parameters firstly decrease sharply until the maximum number of cells merged N_{mf} reaching 200, then decrease slowly (or maintain almost the same value) while N_{mf} increasing. Therefore, $N_{mf} = 200$ has been validated as the most suitable criterion. Furthermore, this grid merge model can reduce the CPU time has also been confirmed.

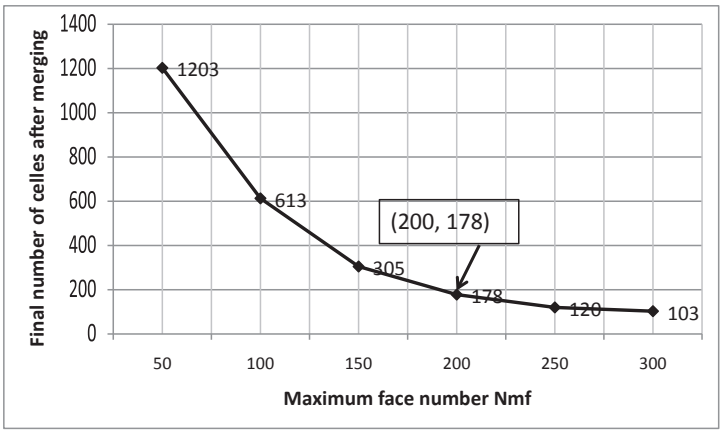

(a) Variation of the new cells number after grid merge according to the maximum face number allowed for the new merged cells N_{mf}

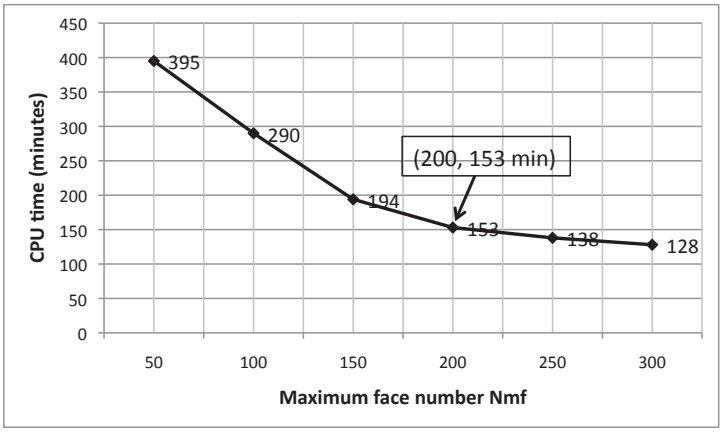

(b) Variation of the CPU time according to the maximum face number allowed for the new merged cells N_{mf}

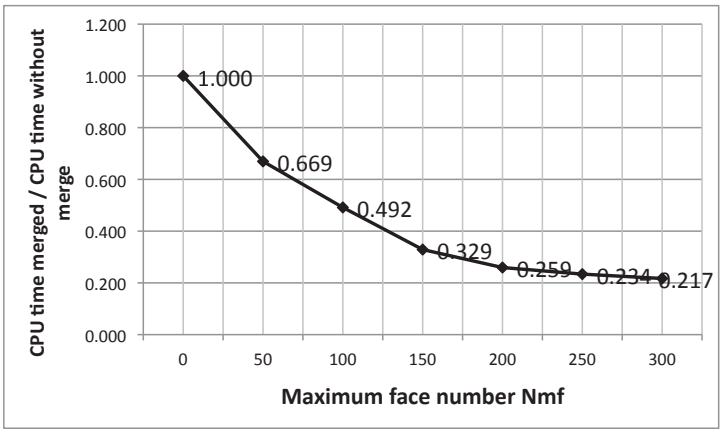

(c) Variation of the ration between the CPU time with merge and the CPU time without merge according to the maximum face number allowed for the new merged cells N_{mf}, the CPU time without merge is 590 min

Figure 4.15 – *Influence of the maximum face number N_{mf} allowed per merged cell, computations realized on SGI Altix350 with 2 processors, with the same variance σ^2*

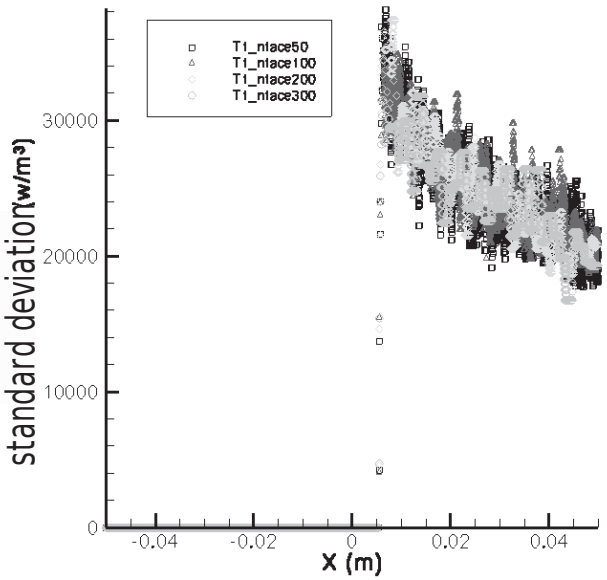

Figure 4.16 – *Variance of the test cases with the different N_{mf} (N_{mf} = 50, 100, 200 and 300), $\Delta T = 1K$, about 10^5 optical paths in total, Uniform Spatial Distribution*

Secondly, having chosen $N_{mf} = 200$, we test the variation of the new cell number after merging N_{cell} as a function of the temperature merging criterion ΔT. As shown in the table 4.4, according to the increase of ΔT, N_{cell} is more or less constant. That can be explained as: on the one hand, the temperature distribution in the zone of burnt gas and non-burnt gas is nearly homogeneous, so whether the grid is combined by $\Delta T = 1K$ or by $\Delta T = 15K$ will not have too much influence on the results of these two zones, on the other hand, in the flame front, normally there is large temperature difference, it might be bigger than 15K, and the objective of our grid merge is not to combine this kind of cells. Additionally, Fig. 4.17 verifies that using different ΔT, provides the same radiative power even in the flame front zone. As a result of that, ΔT can be chosen as 1K, 5K, 10K or 15K.

$\Delta T(K)$	1	5	10	15
N_{cell}	178	173	172	171

Table 4.4 – *Variation of the new cells number after grid merge according to the merging temperature criterion*

Thirdly, in order to validate this grid merge method with more details, a comparison of the radiative power between one case after merging ($N_{mf} = 200$ and $\Delta T = 1K$) and one case without merging has been conducted. Fig. 4.18 shows that both of these two cases match each other excellently even though in the flame front zone. Furthermore as mentioned above, the performance of a Monte Carlo method can be defined as the product of the computation time t and the variance σ^2, it is worth nothing that the computation time would be shorter if a less precision is required. For this reason, to compare their performances, we chose the same variance for these two cases, of course, both of them have

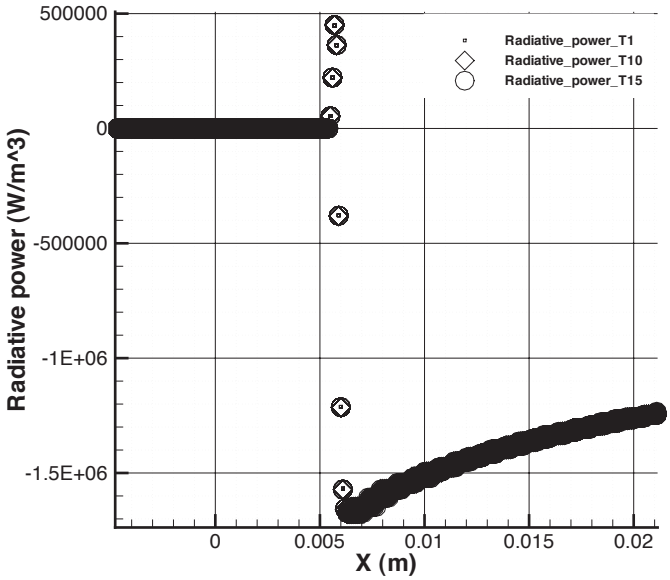

Figure 4.17 – *Comparison of the radiative power for three cases with different* ΔT*,* $N_{mf} = 200$*, Uniform Spatial Distribution*

been converged, then a comparison of the CPU time was observed as shown in Tab. 4.5[2]. In conclusion, the grid merge method works well with the flame 1D test case, which can reduce the CPU time by about 30%.

Test Case	CPU time	Rays/cell	Total ray number	Variance(w/m^3)
With merge	183.7 min	1500	$\sim 10^5$	25000
Without merge	262.6 min	30	$\sim 10^5$	25000

Table 4.5 – *Comparison of the numerical performance between the case with merge and the case without merge, realized by SUN cluster with 2 processors (EM2C Laboratory)*

Turbine gas case

Based on the validation of "Grid Merge Method" in the 1D flame case and the determination of several key numerical parameters corresponding to this method, a computation applied to a more complex realistic geometry is performed in order to qualify the advantage of this merging technique particularly in terms of the reduction of the computational memory.

A swirled gas turbine injector is used here as the complex geometry. The experimental set-up was investigated by Galley (2006). Fig. 4.19 shows the main features of the burner. It is composed by three parts: a swirling generator, a mixing tube and the combustion chamber. Propane is injected with a maximum flow rate $15Nm^3.h^{-1}$ and the air is injected in the diagonal swirler through the holes located on both sides of the 18 swirling vanes with

[2]The reduction of the memory is not very evident for this 1D case, so the comparison of the memory will be presented in the case "turbine gas case" which has a more complex mesh

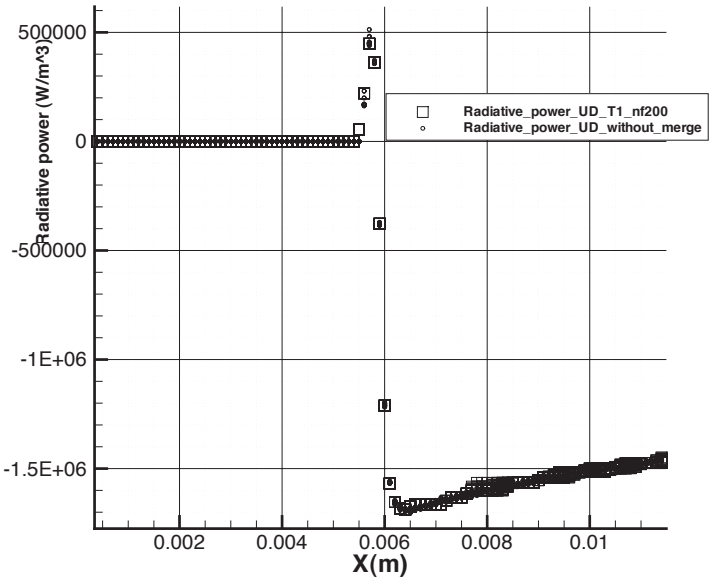

Figure 4.18 – *Comparison of the radiative power between the case without merging (about 10^5 optical paths in total)and the case with maximum 200 faces merged (about 10^5 optical paths in total), $\Delta T = 1K$, Uniform Spatial Distribution*

a maximum flow rate $300Nm^3.h^{-1}$. The computational domain starts at the trailing edge of the vanes including the description of the reactant mixing in the mixing tube.

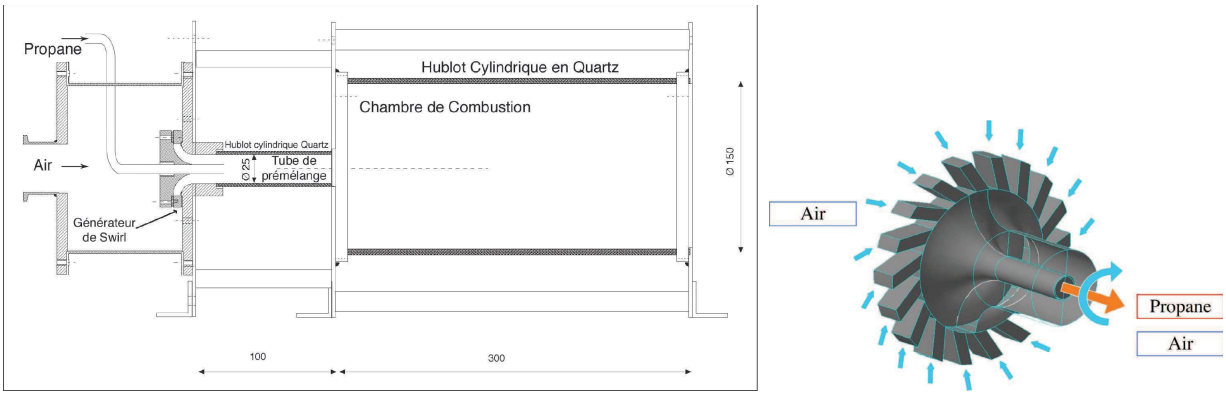

Figure 4.19 – *Geometry of the swirled gas turbine injector*

Fig. 4.20 illustrates the numerical configuration with some simplifications compared with the experimental set-up in order to reduce the complexity of the simulation. On purpose to avoid to simulate the inlet flow velocity, one part of the swirling generator is also meshed. This grid contains about 2 900 000 tetrahedron cells. The minimum grid size is about 0.5 mm which is found in the flame front zone. At the outlet of the combustion chamber, a domain of 40 cm long and 80 cm in diameter was added to roughly simulate the atmosphere conditions. This domain with larger grid size is used here to facilitate the simulation of the flow exiting from the end of the combustion chamber and to reduce the interaction between the boundary condition at the outlet and the flow in the combustion chamber.

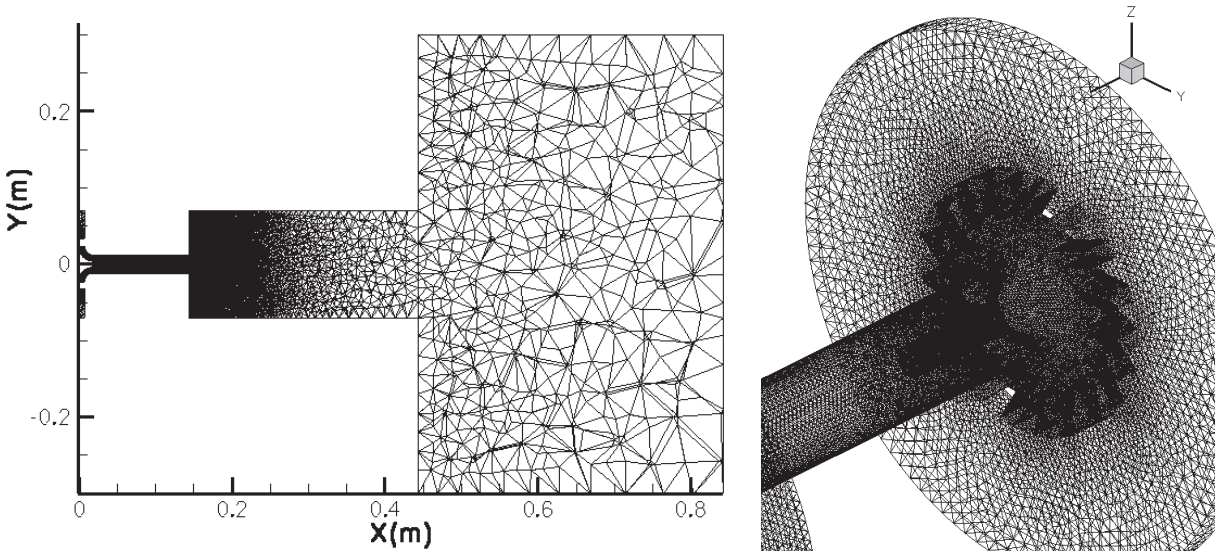

Figure 4.20 – *Longitudinal cut of the mesh of swirled gas turbine injector at $z = 0$ and mesh of one part of swirling generator*

Here we do not present all of the combustion computations conducted with AVBP, more details can be found in the dissertation of Galley (2006). Starting from one of the combustion results already stabilized as shown in Fig. 4.21, we focus on the radiation calculation in two cases: with and without grid merge. The numerical simulations for this swirled gas turbine have been conducted on a computer SGI Altix 350 which has a common memory of 48 Go shared by 16 processors. As shown in Tab. 4.6, the memory required by the case without merge reaches 4.8 G, which is difficult to handle on the industrial computations and can not be applied directly, particularly for the parallel computation, because today the parallel computer only provides a separate memory of about 2 G for each processor.

Test Case	CPU Time	Total rays number	Memory
With merge	1.4 hours	$\sim 10^7$	1.7G
Without merge	16 hours	$\sim 10^7$	4.8G

Table 4.6 – *Comparison of the numerical performance between the case with merge and that without merge for swirled gas turbine injector, computation performed by 5 processors, the CPU time will become 7 hours (1.4×5) and 80 hours (16×5) if only one processor is used. No uniform (NUD) spatial distribution of the optical path source points is used here, so no ray number per cell is presented.*

As having been determined in the previous part for the flame 1D case, the maximum merge face number fixed here is $N_{mf} = 200$ (although for this maximum merge face number determination, there is not a evident link between the 1D flame and turbine gas case, to simplify the problem, $N_{mf} = 200$ is used here. Theoretically, this parameter N_{mf} depends on the initial mesh, so the same kind of tests as performed for 1D flame should be carried out to precisely determine N_{mf}). Considering that the ΔT can vary from 1K to 15K, ΔT has been chosen as $1\%T_{local}$ adapted to the local temperature, as a result of that, ΔT can be 22K for the burnt gas zone where T is about 2200K and be 3K for the unburned gas zone where T is about 300K. Concerning the boundary conditions, the temperature imposed for

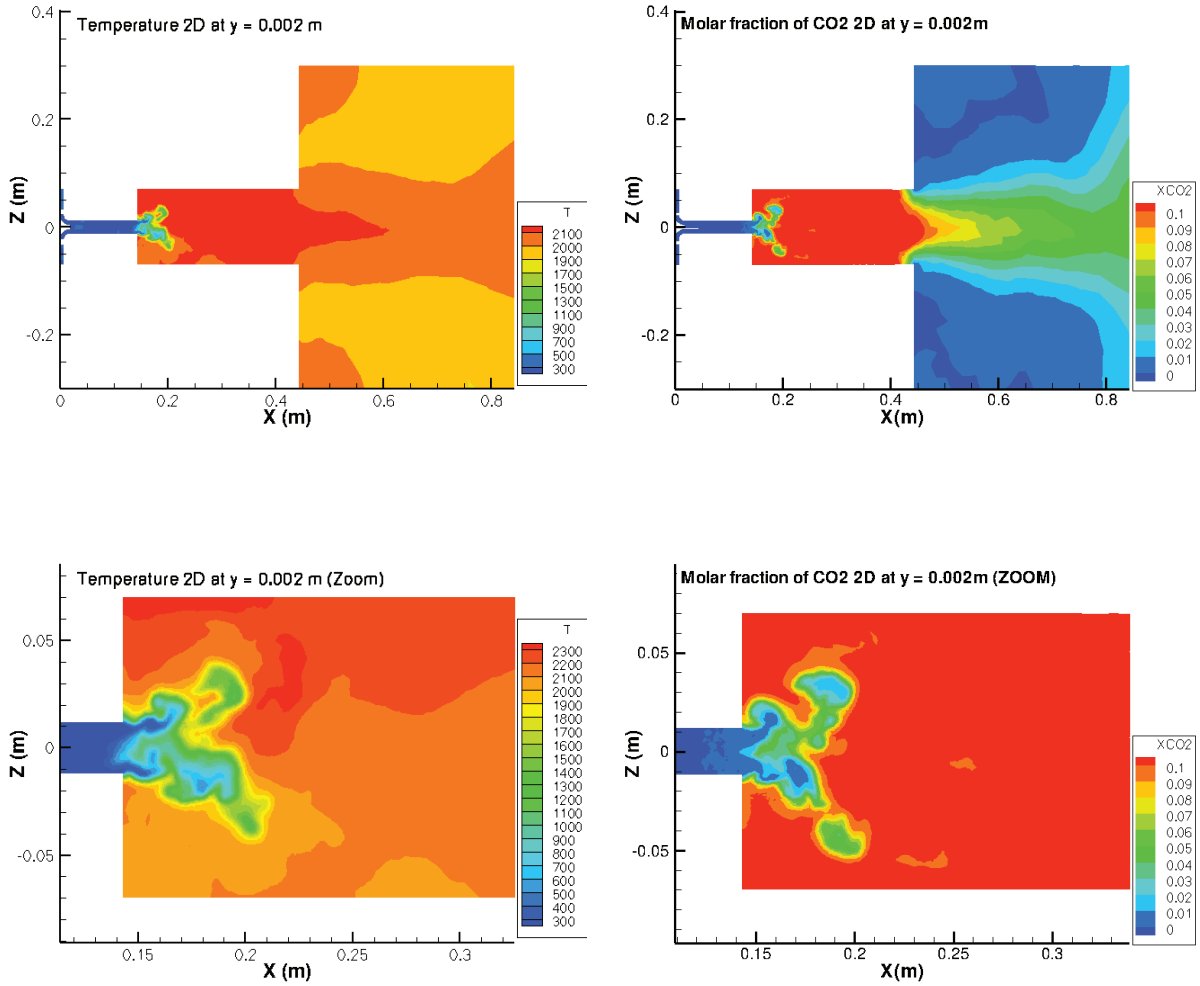

Figure 4.21 – *Temperature profile and molar fraction of CO_2 profile at the plan y = 0.002m, computations realized by Galley (2006) using AVBP*

the inlet and the outlet is respectively 300K and 2000K, emissivity is equal to 1, while other walls have the temperature 500K (here 500K is just an averaged value corresponding a balance between the emission energy and the absorption energy) and the emissivity 0.8. The total ray number is about 3×10^7 and the calculation is converged.

Fig. 4.22 displays the radiative power at y = 0.002 m. In these two cases, we obtain more or less the same results even if a little overestimation or underestimation is found in some small zones. To make a comparison between them more clearly, two cuts at $x = 170\ mm$ and $x = 190\ mm$ are presented in Fig. 4.23. We note that the maximum difference between these two cases is about 7%, validating the method.

Furthermore, a little more discussion about the temperature criterion ($1\%T_{local}$ for this case or ΔT for 1D case). For some cells which have hight temperature, $\Delta T = \%1T_{local}$ will be relatively large, especially for the flame front where large temperature gradients exist. Additionally, the radiative power varies as T^4, so a little variation of temperature can lead to a great changing of the radiation characteristics. As a result, if we would like to

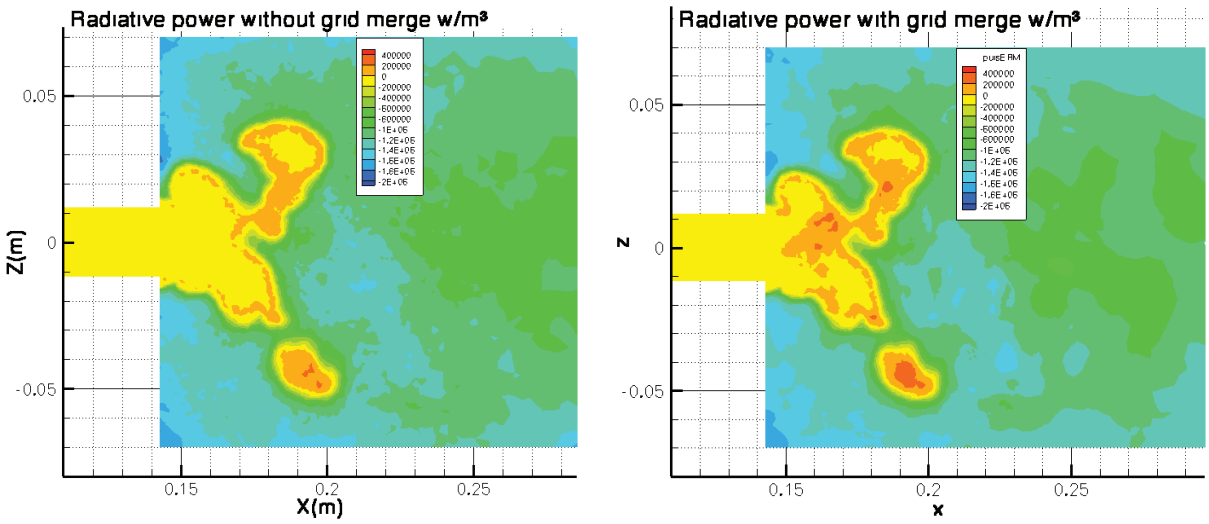

Figure 4.22 – *Comparison of the radiative power at y = 0.002 m betwee n two cases : without grid merge and with grid merge (maximum merged faces number N_{mf}= 200, $\Delta T.$ = 1%T_{local})*

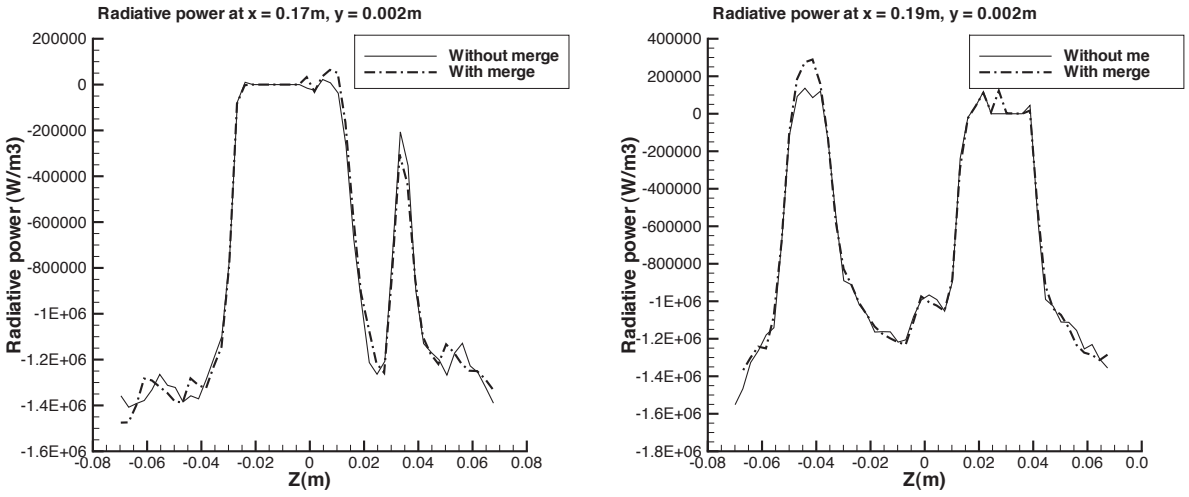

Figure 4.23 – *Comparison of the radiative power at y = 0.002 m, x = 0.17 m, and x = 0.19 m between the case without grid merge and the case with grid merge (maximum merged faces number N_{mf}= 200, ΔT = 1%T_{local})*

increase the precision of this grid merge method, a solution is to fix a temperature criterion distinguishing high and low temperature zones and combining 1%T_{local} and ΔT, for example if $T_{local} < 1500K$, $\Delta T = \%1T_{local}$, else $\Delta T = 15K$.

In terms of numerical performances, according to the results presented in Tab. 4.6, both of these two cases are converged with a total optical paths 10^7 (NUD), the computation using this grid merge method takes about 10% (1.4h) of the CPU time needed for the computation without merge (16 h) and the memory storage decreases from 4.8 G to 1.7 G, significantly improving the performance of the Monte Carlo method. In addition, the performance improvement is more efficient in this turbine gas case than in the 1D flame

case, because the homogeneous zone is more important here and much more cell number has been decreased. As mentioned before, in 1D case, the cell number changes from 16 000 to $\sim$ 200 by merge, and in turbine gas case, it changes from $\sim$ 2 900 000 to $\sim$ 20 000.

Conclusion

A "Grid merge method" has been developed and validated with a 1D premixed laminar flame and a swirled gas turbine injector, the impact of two factors - maximum merged face number N_{mf} and the temperature criterion ΔT has also been discussed. The precision of the results after merging can be controlled by changing these two factors, and the difference of the radiative power between the case with merge and the case without merge is little enough to be accepted in our future computations. This technique is particularly efficient for combustion computation with large homogeneous area, like in furnaces. In addition, the reduction of CPU usage and memory storage obtained shows that this method is very efficient to improve the performance of the Monte Carlo Method.

4.2.2 "Near-range-interaction far-range-interaction" (NIFI) method

Method description

"Near-range-interaction far-range-interaction" used here does not have the same meaning as in the electromagnetic concept. It is an optimized formulation dealing with the far field and the near field of our radiative transfer computational domain differently (simplified as NIFI in this dissertation). This model is developed to improve the performance of the numerical solver.

As shown in Fig. 4.24, the principe of this model can be briefly described as below: in order to calculate the radiative power at point A in the computational domain, we can artificially divide the whole area into two parts (Part 1 and Part 2). Part 1 is a set of all the points which are located inside a sphere with the diameter R_0 and the center point A, such as the field inside the circle presented in Fig. 4.24, and is called "near-range" in this dissertation. Part 2 is a set of all the points which are located outside the sphere, which means the distance between these points and the center point A (noted as R) is larger than R_0, presented by the field outside the circle in Fig. 4.24, and is called "far-range" here (R_0 is called the criterion distance to distinguish the "near-range" and "far-range").

We will assume that above this criterion distance R_0, the influence of the *fluctuation* of the "far-range" (Part 2) on the computation of the radiative power at point A can be neglected, which means that the influence of the "far-range" on radiation power computation is independent on time. So for each iteration of radiation, the radiative power at point A can be calculated by only taking into account the variation in "near-range" while the "far-range" radiation is kept constant. Concerning its physical signification, it means that, over certain distance, the alternation of burnt gas and unburnt gas in the "far-range" will be no longer important for the local radiation computation. This assumption can be simply understood like this, but indeed it comes from the test cases (as shown below in this part).

If this assumption can be verified and validated, the radiation computation will be largely simplified. For example, in the coupling calculation between combustion and radiation, after N iterations of the combustion computation, a set of thermodynamics data, such as

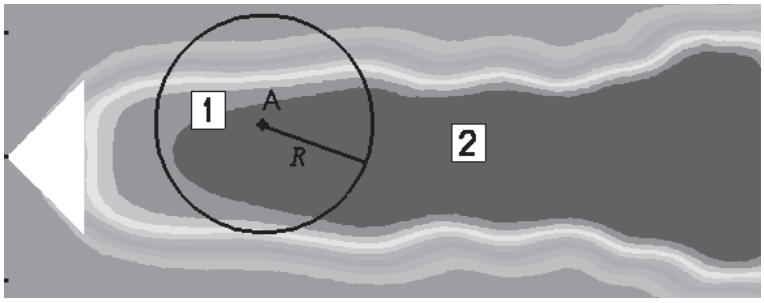

Figure 4.24 – *principle of the "near-range-interaction far-range-interaction" model*

temperature and mass fraction of the species (Y_i), calculated by the combustion code have been obtained and will be sent to the radiation solver. With this "NIFI" method, instead of sending these data for all of the computational domain, only the data in the "near-range" for each point corresponding in the computational domain will be sent to the radiation code, and the data in the "far-range" field will remain the old value or use an averaged radiation value. As a result of that, less information is needed to be stored in the radiation code and less data will be exchanged between the combustion solver and the radiation solver, furthermore, less computation will be needed.

In the real cases, this model should be used to all of the points in the computational area, but in the following validating cases, to simplify the calculation and just present the principal idea, all the tests are performed just at one given point.

Firstly, a simple test case is performed to validate this formulation and to demonstrate its feasibility. Then this model is applied to a three dimensional flame. During the validation, a key parameter is discussed - the criterion distance R_0. Obviously, this method should be applied to the optically thin medium, because if the medium is optically thick, the energy carried by the optical paths will be quickly absorbed, the length of the optical path is then short, so there is no "far-range". Therefore, at the end of this part, the optical thin assumption has also been verified.

Method tests

A simple three dimensional configuration, shown in Fig. 4.25 (a), is used to validate this approach. This computational mesh contains 8 000 hexahedron cells in a domain of $x, y, z \in [-0.1\ m, 0.1\ m]$ ($20 \times 20 \times 20$ cells respectively in x, y, z direction). The grid size is $0.01\ m$. To simplify the problem, here we did not use the AVBP code to compute the combustion data. The temperature and the molar fractions of CO_2 and H_2O (X_i) are just set artificially around the center of this cube as shown in Fig. 4.25 (b) (c). These instantaneous parameters, at a given time noted as t_1, follow the formulations below:

$$T(t_1) = 1000 \cdot \sin\left(\frac{2\ \pi}{0.04} \cdot\ R\right) + 1300$$

$$XCO_2(t_1) = 0.06 \cdot \sin\left(\frac{2\ \pi}{0.04} \cdot\ R\right) + 0.06$$

$$XH_2O(t_1) = 0.08 \cdot \sin\left(\frac{2\ \pi}{0.04} \cdot\ R\right) + 0.08 \tag{4.8}$$

where R is the distance from the center point A (0, 0, 0).

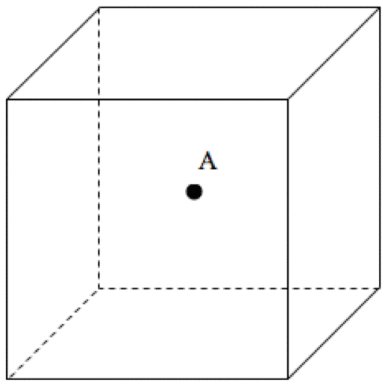

(a) Geometry of the test case

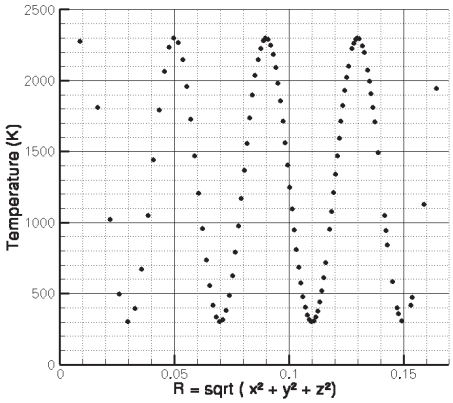

(b) Instantaneous temperature profile imposed artificially for the case at t_1

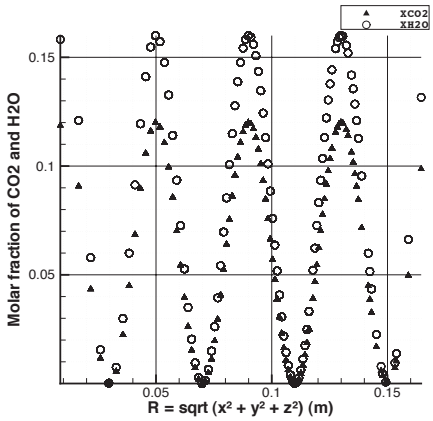

(c) Instantaneous molar fractions of CO_2 and H_2O imposed artificially for the case at t_1

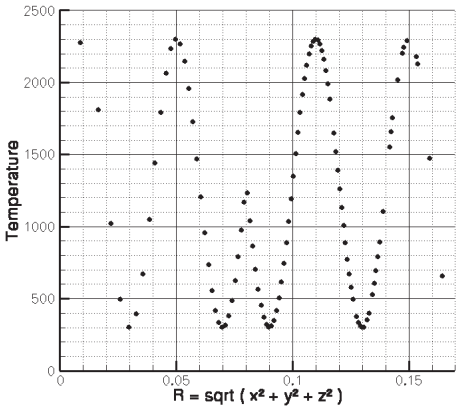

(d) Instantaneous temperature profile imposed artificially for the case at t_2 with $R_0 = 0.08\ m$

Figure 4.25 – *Presentation the test case to validate NIFI model*

In order to test the influence of the "far-range" thermodynamic profiles on the radiative power of point A, a new thermodynamic profile is imposed by changing the thermodynamic profiles of the "far-range" as: for $R < R_0$, we retain the same thermodynamic profiles (T,X_{CO_2} and X_{H_2O}) as those at case t_1 (Eq. 4.8), for $R > R_0$, we impose the new profiles as illustrated in Eq. 4.9, in fact, compared with the profiles at t_1, these new profiles correspond to a phase changing of π :

$$T(t_2) = -1000 \cdot \sin\left(\frac{2\ \pi}{0.04} \cdot\ R\right) + 1300$$

$$XCO_2(t_2) = -0.06 \cdot \sin\left(\frac{2\ \pi}{0.04} \cdot\ R\right) + 0.06$$

$$XH_2O(t_2) = -0.08 \cdot \sin\left(\frac{2\ \pi}{0.04} \cdot\ R\right) + 0.08 \tag{4.9}$$

If the criterion distance R_0 is chosen as $R_0 = 0.08\ m$ (here $R_0 = 0.08\ m$ is just a example value, the impact of different R_0 values will be discussed later), this new composed temperature (noted as case at time t_2) can be displayed in Fig. 4.25 (d).

Then two thermodynamics parameters (imposed at t_1 and t_2) are used by radiation solver to compute the radiative power field. Here all the six walls are considered as blackbodies with the temperature equal to 300K. Fig. 4.26 shows the radiative power based on case t_1 and case t_2 ($R_0 = 0.08\ m$) as a function of the distance R (Here R is the distance between each point in the computational domain and point A). The temperature of point A is 1300K.

Furthermore, in order to determine the most suitable criterion distance R_0, several tests have been performed (with $R_0 = 0.02 \cdot i, i = 2...8$). Fig. 4.27 shows the difference of the radiative power at point A between the case t_1 and the case t_2 on function of R_0. Evidently, this difference decreases gradually on function of R_0. That means the fluctuations of thermodynamics parameters located far from the point computed (point A for this test) have less impact, and this impact decreases gradually according to the this distance increasing. So from certain distance R_0, the influence of fluctuation of the "far-range" field can be ignored. This conclusion is interesting for the complex computations, because for each point to be computed in the computational domain, we can always divide the field into two parts - "near-range" field and "far-range" field and just consider the fluctuation of its "near-range" field for each iteration. For the example displayed in Fig. 4.27, the error is about 1% when the distance R_0 is about 0.12 m (noting that the period of this signal is 40 mm, 0.12 m is just three times of the period).

Then this model is applied to a real three dimensional flame test case to evidence its advantage in complex computations.

Three dimensional flame test case and discussions

The geometry configuration and physical parameters used for this three dimensional flame test case are the same as these in the case $\ll Diedre\_3D \gg$ in Chapter 5, except that a mesh with less number of cells is used here and the grid size is a little different. The emissivity is equal to 1 for all the walls.

The radiative computations are based on the combustion results calculated by AVBP at four different instantaneous time (t_1, t_2, t_3 and t_4 are respectively obtained from 2 750 000 iterations, 2 800 000 iterations, 2 850 000 iterations and 2 900 000 iterations of AVBP calculation, and the AVBP time step is about $\Delta t_{LES} \approx 0.19\mu s$). So there is about 10 ms between each thermodynamics field. The temperature fields and the molar fractions of CO_2 and H_2O fields are displayed in Fig. 4.28.

In order to simplify the presentation of the model principe, as mentioned above, only the computations at several given points are taken as an example. The radiative power of point i can be computed by:

$$P_{i,e}(t_j) \longrightarrow F_{i,N}(t_j) + F_{i,F}(t_j)$$

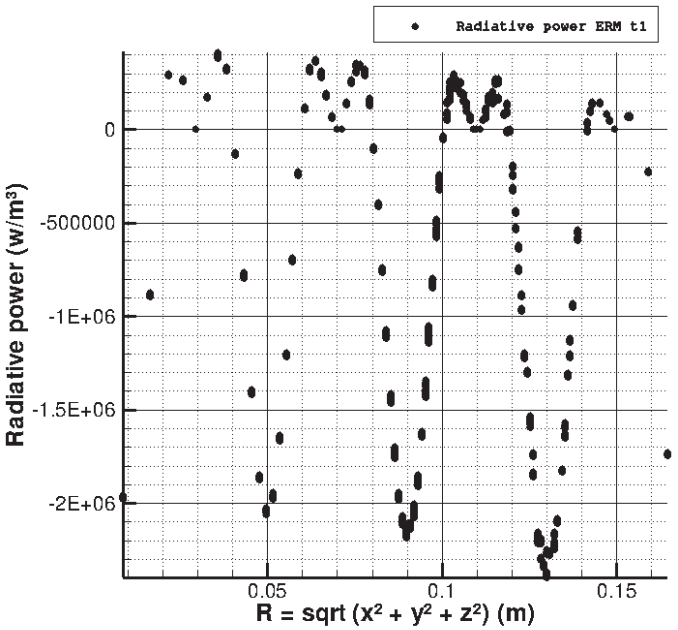

(a) ERM radiative power field for case at t_1, corresponding temperature profile shown in Fig 4.25 (b)

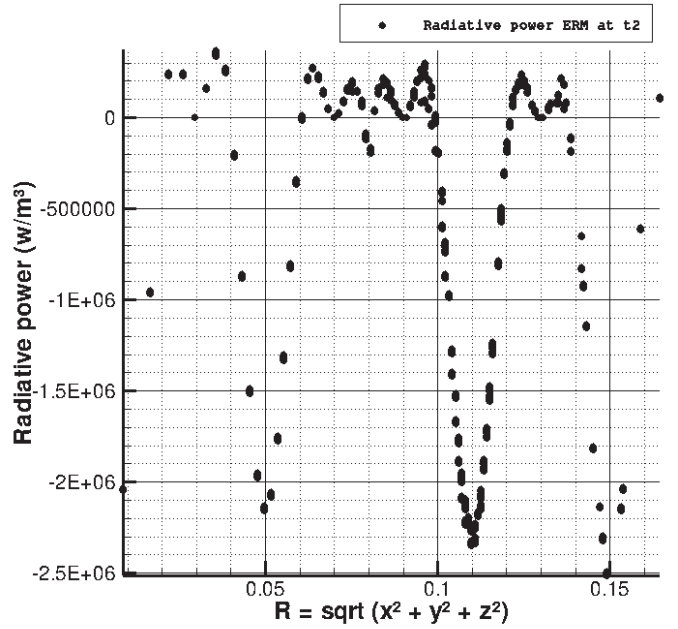

(b) ERM radiative power field for case at t_2, $R_0 = 0.08\ m$, corresponding temperature profile shown in Fig 4.25 (d)

Figure 4.26 – *Radiative power ERM at point A at different times*

$$P_{i,a}(t_j, t_{j\prime}) \longrightarrow F_{i,N}(t_j) + F_{i,F}(t_{j'}) \tag{4.10}$$

where $P_{i,e}(t_j)$ is the exact radiative power computed at point i using the thermodynamics data (temperature, molar fractions of CO_2 and H_2O, etc.) at t_j, $F_{i,N}(t_j)$ represents the thermodynamics data in the "Near-range" field of point i at t_j and $F_{i,F}(t_j)$ represents the thermodynamics data in the "Far-range" field of point i at t_j. The definition of "Far-range"

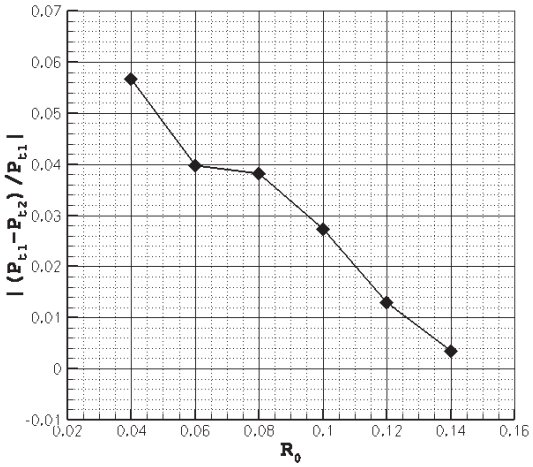

Figure 4.27 – *The difference of radiative power ERM of point A between case t_1 and case t_2 on function of the criterion distance R_0, P_{t1} is the radiative power computed using the thermodynamics profiles (temperature and molar fractions of CO_2 and H_2O) of case t_1, P_{t2} is the radiative power computed using the thermodynamics profiles (temperature and molar fractions of CO_2 and H_2O) of case t_2, R_0 is the criterion distance*

field is the same as mentioned above, which means if the distance between the field and the computed point i is larger than R_0, this field can be considered as "Far-range" field for point i. On the other hand, $P_{i,a}(t_j)$ is the approximate radiative power computed at point i using the thermodynamics data in the "Near-range" field of point i at t_j and the thermodynamics data in the "Far-range" field of point i at $t_{j'}$. According to the "NIFI" model, from a certain distance R_0, the influence of the fluctuation of the "Far-range" radiation field can be neglected. As a result of that, the approximate radiative power $P_{i,a}(t_j)$ will almost equal to the exact radiative power $P_{i,e}(t_j)$.

Then the following work is to find the critical distance R_0 from which the difference between $P_{i,e}(t_j)$ and $P_{i,a}(t_j, t_{j'})$ could be ignored. That means to test the error:

$$E_{P_i}(t_j, t_{j'}) = \left| \frac{P_{i,e}(t_j) - P_{i,a}(t_j, t_{j'})}{P_{i,e}(t_j)} \right| \tag{4.11}$$

This model is now applied to the three dimensional flame test case. In order to simplify the presentation, just the computation at two given points has been taken into account. As indicated in Fig.4.28 (a) (e) (i), Point A and point B are used as the computed points. These two points at the four instantaneous time (t_1, t_2, t_3 and t_4) have different temperatures and can represent four different flame states which making the test more general. The tests are performed respectively for the hot points (with high temperature, ex: point A and point B at t_1) and for the cold points (with low temperature, ex: point A and point B at t_2). The thermodynamics parameters related to point A and point B are displayed in Tab.4.7 and Tab.4.8, all of the computations below are based on these two points.

a: Test cases for the hot points

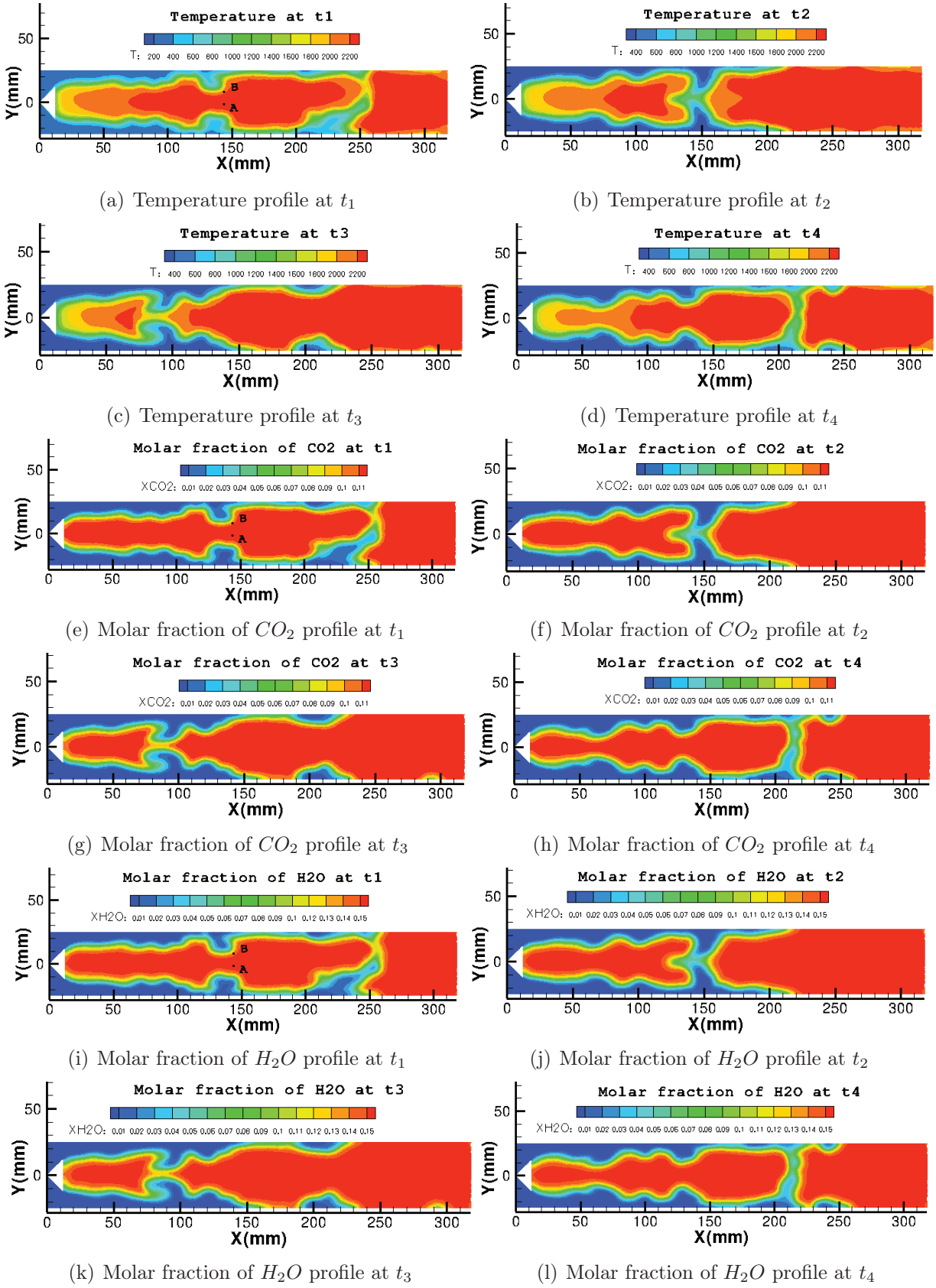

(a) Temperature profile at t_1

(b) Temperature profile at t_2

(c) Temperature profile at t_3

(d) Temperature profile at t_4

(e) Molar fraction of CO_2 profile at t_1

(f) Molar fraction of CO_2 profile at t_2

(g) Molar fraction of CO_2 profile at t_3

(h) Molar fraction of CO_2 profile at t_4

(i) Molar fraction of H_2O profile at t_1

(j) Molar fraction of H_2O profile at t_2

(k) Molar fraction of H_2O profile at t_3

(l) Molar fraction of H_2O profile at t_4

Figure 4.28 – *Temperature profiles and molar fraction profiles of the case ≪ Diedre_3D ≫ at the different computational time of combustion (details about this configuration will be presented in Chapter 5), 2D slice at $z = 0.5$ mm, Goncalves dos Santos (2008)*

Thermodynamics data	t_1	t_2	t_3	t_4
Temperature (K)	2253	930	2254	2264
Molar fraction CO_2	0.1156	$3.07E-2$	0.1165	0.1163
Molar fraction H_2O	0.154	$4.1E-2$	0.1554	0.1552
$P_{A,e}$ (w/m^3)	-2.01 E6	6.91 E4	-1.92 E6	-1.82 E6

Table 4.7 – *Thermodynamics data and exact radiative power of point A at four different instantaneous time t_1, t_2, t_3 and t_4*

Thermodynamics data	t_1	t_2	t_3	t_4
Temperature (K)	2225	692	2263	2266
Molar fraction CO_2	0.113	$1.55E-2$	0.1162	0.1159
Molar fraction H_2O	0.1508	$2.07E-2$	0.155	0.1546
$P_{B,e}$ (w/m^3)	-1.95 E6	1.24 E5	-1.95 E6	-1.96E6

Table 4.8 – *Thermodynamics data and exact radiative power of point B at four different instantaneous time t_1, t_2, t_3 and t_4*

The exact radiative power of point A at t_1 can be represented as (the same for point B):

$$P_{A,e}(t_1) \longrightarrow F_{A,N}(t_1) + F_{A,F}(t_1) \tag{4.12}$$

To compute the error, three approximate radiative power of point A, $P_{A,a_2}(t_1,t_2)$, $P_{A,a_3}(t_1,t_3)$ and $P_{A,a_4}(t_1,t_3)$, respectively using the thermodynamic data of "Far-range" field at t_2, t_3 and t_4 are:

$$\begin{aligned} &P_{A,a_2}(t_1,t_2) \longrightarrow F_{A,N}(t_1) + F_{A,F}(t_2) \\ &P_{A,a_3}(t_1,t_3) \longrightarrow F_{A,N}(t_1) + F_{A,F}(t_3) \\ &P_{A,a_4}(t_1,t_4) \longrightarrow F_{A,N}(t_1) + F_{A,F}(t_4) \end{aligned} \tag{4.13}$$

$$E_{P_{A,k}}(t_1,t_k) = \left| \frac{P_{A,e}(t_1) - P_{A,a_k}(t_1,t_k)}{P_{A,e}(t_1)} \right| (k = 2,3,4) \tag{4.14}$$

Evidently, here the thermodynamics data in "Near-range" field at t_1 is kept for all of these four cases. For each approximate case, the influence of the criterial distance R_0 is studied. Fig. 4.29 illustrates that the error $E_{P_{A,k}}(t_1,t_k)(k = 2,3,4)$ and $E_{P_{B,k}}(t_1,t_k)(k = 2,3,4)$ decrease when R_0 increases. For $R_0 > 40\ mm$, the error is lower than 1%. Noting that in the case t_2, father than 40 mm, the error does not evidently attenuate to zero. Because both point A and point B have low temperatures at t_2, as mentioned before, ERM method does not converge very well in cold zones, which leads to this little error. However, it varies near 0.5%, which is already small enough. To conclude, the thermodynamic data variation in the "Far-range" field with the distance larger than 40 mm from the point computed (point A or point B) can be ignored, so the same data of "Far-range" field can be retained for each new radiative computation iteration. Only the corresponding data in the "Near-range" field

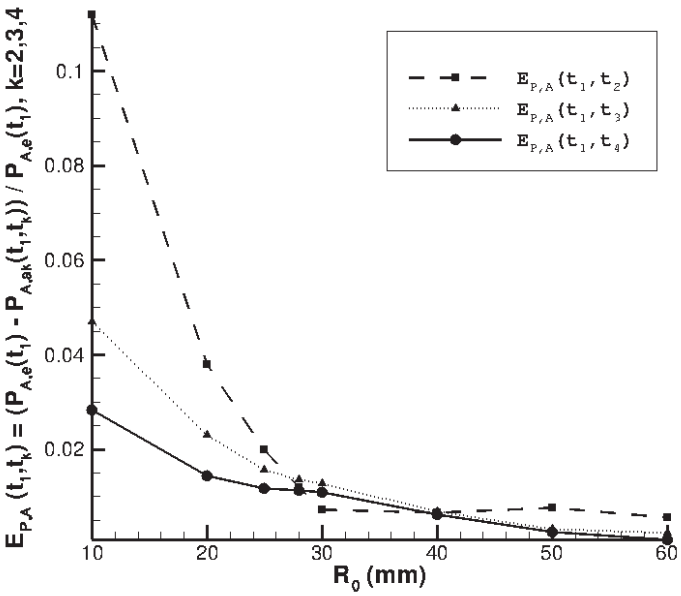

(a) Point A

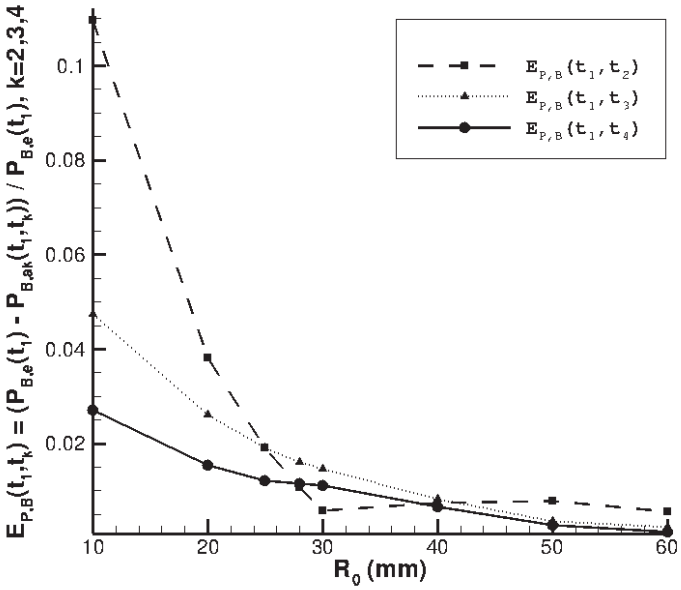

(b) Point B

Figure 4.29 – *Difference between the exact radiative power computed at t_1 and the approximate radiative power computed by using the "Far-range" data at time t_2, t_3 and t_4 on function of the characteristic distance R_0, referring to Eq. 4.14*

should be updated. About choosing the thermodynamic data in the "Far-range" field, we use the data of one given iteration, such as that at t_1 in the above test case.

Then the CPU time reduction with this model for the hot points is studied. Fig. 4.30 gives the distribution of the total optical path length from point A at t_1, these optical path

lengths are determined by computing from point A to the point where all the energy carried by this path is totally absorbed. Observing that 62% of the optical path lengths are longer than 40 mm, so applying this model will reduce the computational time.

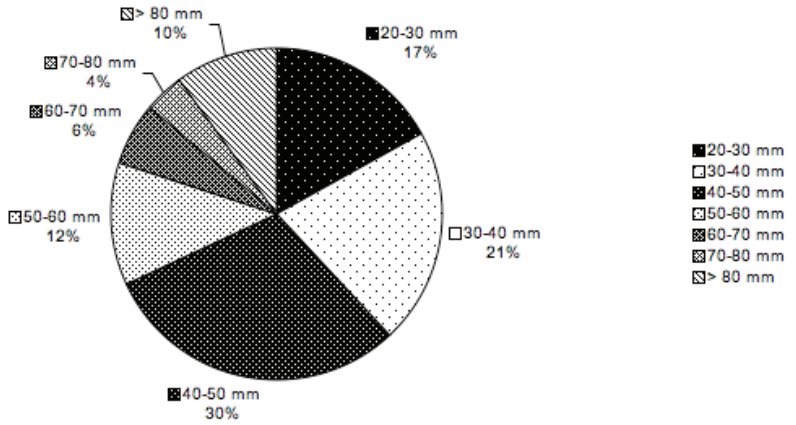

Figure 4.30 – *Distribution of the total optical path length departing from point A at* t_1

The CPU time reduction can be roughly evaluated as: for the optical paths longer than 40 *mm* (62% of the total optical paths), only the portion shorter than 40 *mm* should be treated and the portion longer than 40 *mm* will correspond to the "Far-range" having already saved. For example, for an optical path with length of 50 *mm*, time reduction is about $10/50 = 20\%$ if we assume that computing time is homogeneous for each portion of the optical path. The same principe for other optical paths.

b: Test cases for the cold points

The temperature of points A and B at t_2 are low, and are considered as the examples of the cold points. Similarly to the test cases for the hot points, the exact radiative power and the approximate power of point A at t_2 can be computed as:

$$\begin{aligned} &P_{A,e}(t_2) \longrightarrow F_{A,N}(t_2) + F_{A,F}(t_2) \\ &P_{A,a_3}(t_2,t_3) \longrightarrow F_{A,N}(t_2) + F_{A,F}(t_3) \\ &P_{A,a_4}(t_2,t_4) \longrightarrow F_{A,N}(t_2) + F_{A,F}(t_4) \end{aligned} \tag{4.15}$$

and the corresponding error between the exact radiative power at t_2 and the approximate power at t_3 and t_4 of point A is (similar to Eq 4.14):

$$E_{P_{A,k}}(t_2,t_k) = \left| \frac{P_{A,e}(t_2) - P_{A,a_k}(t_2,t_k)}{P_{A,e}(t_2)} \right| (k = 3,4) \tag{4.16}$$

Distinguishing from the case (a) for the hot points, here the thermodynamics data in the "Near-range" field is at instantaneous time t_2. Fig. 4.31 displays the approximate radiative

powers $P_{A,k}(t_2,t_k)(k=3,4)$ and $P_{B,k}(t_2,t_k)(k=3,4)$ on function of the characteristic distance R_0. Fig. 4.32 illustrates that the error $E_{P_{A,k}}(t_2,t_k)(k=3,4)$ and $E_{P_{B,k}}(t_2,t_k)(k=3,4)$ decrease when R_0 increases. Different from the results in the test cases for the hot points, noticed that the error of point A here can reach about 10% when $R_0 > 40\ mm$ (at $R \approx 50\ mm$ and $R \approx 70\ mm$ as shown in Fig. 4.32 (b)). In certain cases, this error level can be acceptable and the reasons could be:

- It could be a calculation error, because the radiative power for the cold points are low, so the relative error is important for a small quantity.
- As mentioned before, it could be due to the fact that ERM method does not work well in the cold zones.

To conclude, for certain point of view, the NIFI model works not so well for the cold points as that for the hot points.

c: Temperature criterion to distinguish the hot points and the cold points

Because this method produces a different accuracy level in hot and cold zones, a temperature criterion is proposed here to distinguish these two zones to improve the performance and the precision of this method. Hot and cold zones will be treated differently.

Computations are now performed for all the points in the domain. Fig. 4.33 shows the difference between the exact radiative power at t_1 and the approximate radiative power by using the "Far-range" thermodynamic data at t_2 on function of the temperature for the entire computation domain. Formulation is:

$$E_{P_i}(t_1,t_2) = \left| \frac{P_{i,e}(t_1) - P_{i,a}(t_1,t_2)}{P_{i,e}(t_1)} \right| \tag{4.17}$$

where i represent each point i in the whole computation domain, which is different from that presented in the precedent cases - only two points A and B were computed. Then this value $E_{P_i}(t_1,t_2)$ is divided by the number of cells having the same temperature (here the "same" means in the interval $[T_i - 0.5K, T_i + 0.5K]$) to obtain an average error $AvgE_{P_i}(t_1,t_2)$. Here the criterion distance R_0 is 40 mm.

Evidently NIFI model works well when the temperature is higher than 1500K (Error $< 5\%$) and gives a poor accuracy for temperature lower than 1500K, particularly for the zone near 1000K[3]. Additionally, in the zone where the temperature is about 300 K, this average error is almost equal to 1. Because the radiative power in this zone is almost zero, large errors are then observed.

So the temperature criterion can be fixed as 1500 K, NIFI model will be applied for points where the temperature is higher than 1500 K and the exact computation is retained for points where the temperature is lower than 1500 K. For the combustion case, we have a large homogenous hot zone with burnt gas (temperature $>$ 1500 K) and a large homogenous cold zone with unburnt gas (temperature is near to 300 K where there is almost no emission power), consequently, the zone with the temperature between 300K and 1500K is only found

[3]1000K is just in the middle of 600K where the absorption is dominant compared to emission and 1600K where the emission is dominant compared to absorption, the radiative power value at 1000K is then very small and almost zero, therefore, large errors are then obtained

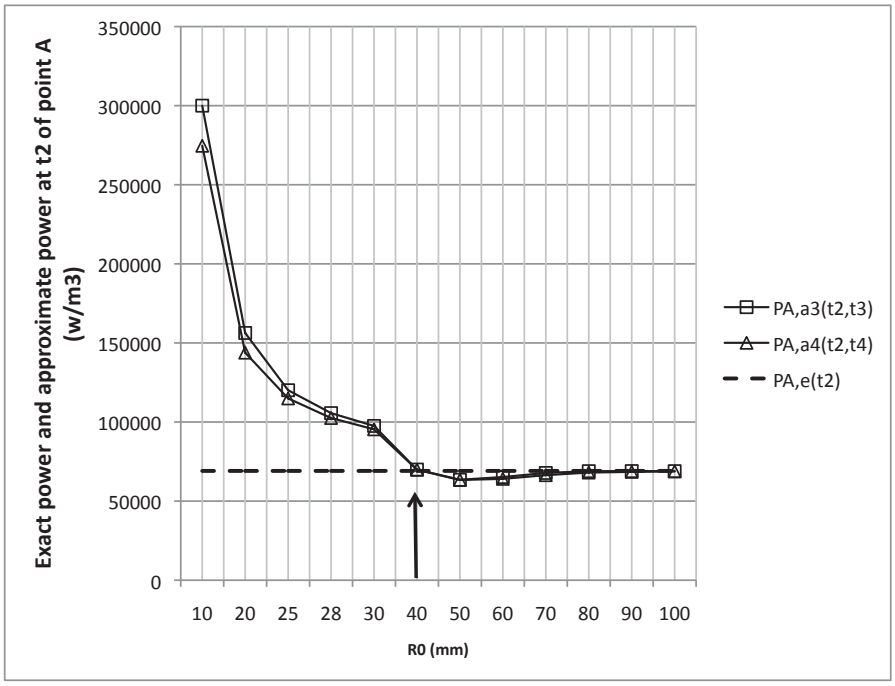

(a) Point A

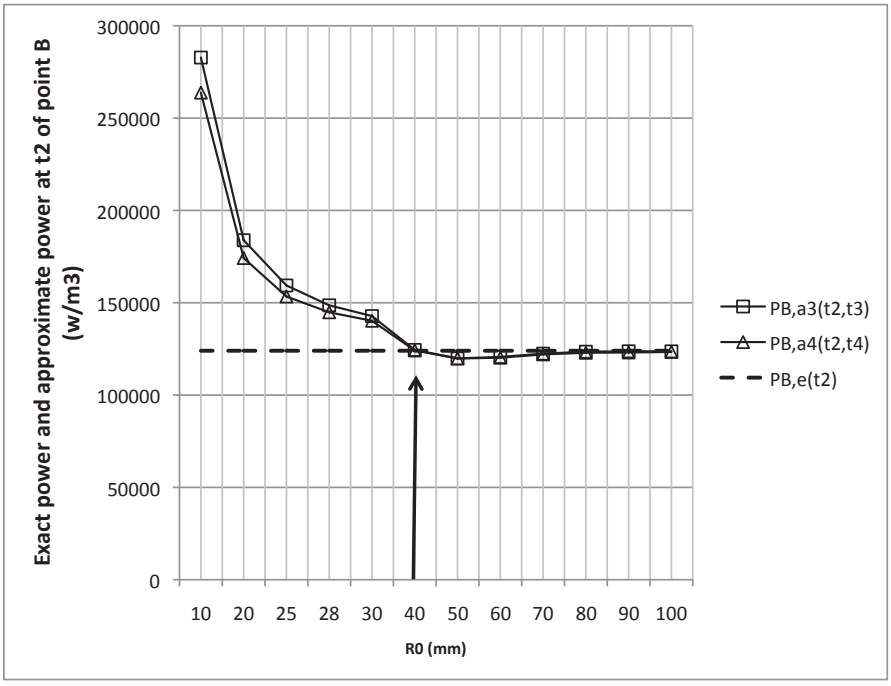

(b) Point B

Figure 4.31 – *The approximate radiative powers computed by using the "Near-range" data at t_2 and the "Far-range" data at time t_3 and t_4 and the exact radiative power at t_2 on function of the characteristic distance R_0, referring to Eq. 4.14*

in the flame front. For this reason, even if the NIFI model is only used for the hot cells, a large reduction of the CPU time can be always obtained.

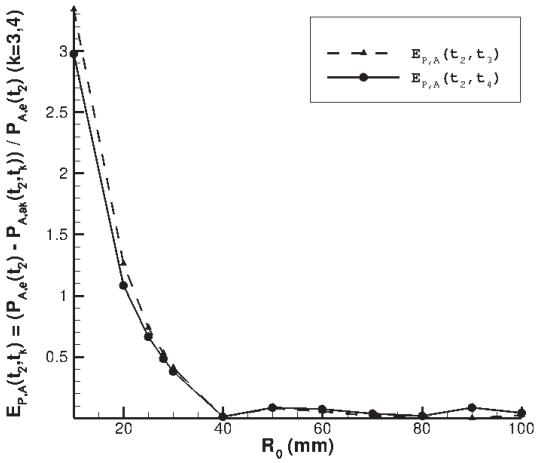

(a) Point A

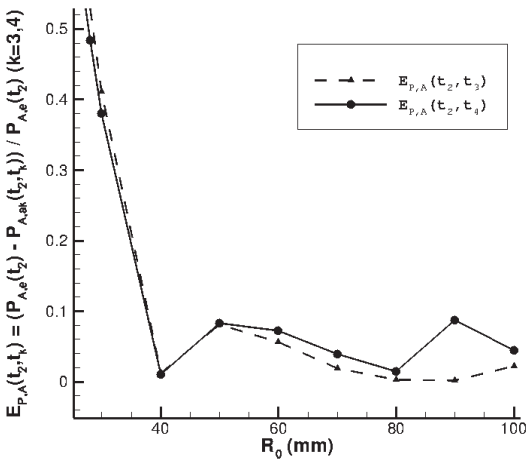

(b) Point A, Zoom

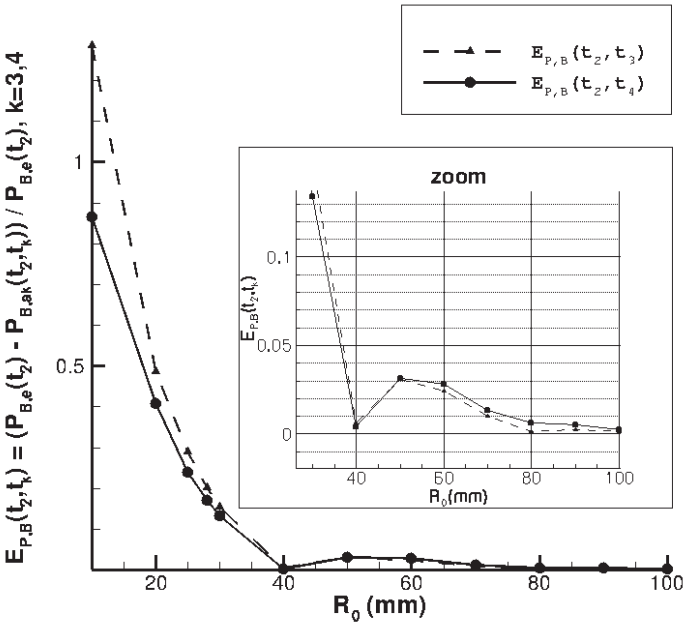

(c) Point B and the zoom of point B

Figure 4.32 – *Difference between the exact radiative power computed at t_2 and the approximate radiative power computed by using the "Far-range" data at time t_3 and t_4 on function of the characteristic distance R_0, referring to Eq. 4.14*

d: Remarks:

1. **Convergence test**

   Due to the requirement of the statistical method, for all Monte Carlo computations, before performing the calculation, the convergence should be verified firstly. So here the number of the optical paths generated from point A should be firstly determined to get the converged results.

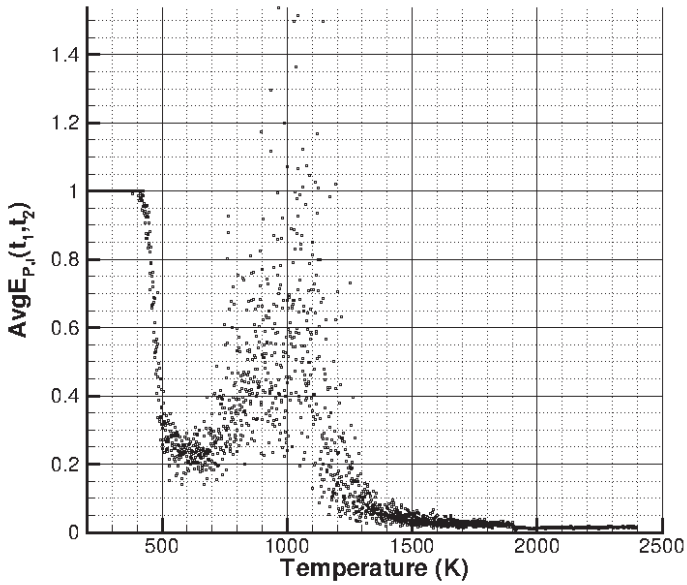

Figure 4.33 – *Difference between the exact radiative power at t_1 and the approximate radiative power by using the "Far-range" thermodynamic data at t_2 on function of the temperature for all the points in computation domain, characteristic distance $R_0 = 40\ mm$*

According to the law of large numbers (LLN) and using the same principe as mentioned in Chapter 4.1 (Fig, 4.5), the optical paths generated for each parallel computation (N_j) is determined as $N_j = 25\ 000$, and 40 parallel computations are used (which means the number of beams $N_b = 40$), so the total optical paths generated from point A is $N = 10^6$.

As show in Fig. 4.34, when $log_{10}(N) = 6$, the curve "standard deviation computed" collapses well with the curve "standard deviation reference" $(1/\sqrt{N})$, which means this Monte Carlo computation has been largely converged (see the explications of this principe in Chapter 4.1 for more details)

2. **Optically thin assumption**

Considering an absorbing and emitting medium, the monochromatic transmissivity can be expressed as (Taine et al. 2003):

$$\tau' = \exp(-e_\nu) \tag{4.18}$$

where e_ν is the optical thickness, it is a dimensionless quantity and can be calculated as below (Taine et al. 2003; Soufiani and Taine 1997):

$$e_\nu = \int_{x\prime}^{x} k_\nu dx'' = k_{m,\nu} \cdot L_m \tag{4.19}$$

$$k_{m,\nu} = x \cdot p_s \cdot [T \cdot Q(T)]^{-1} \cdot k^*_{m,\nu} \tag{4.20}$$

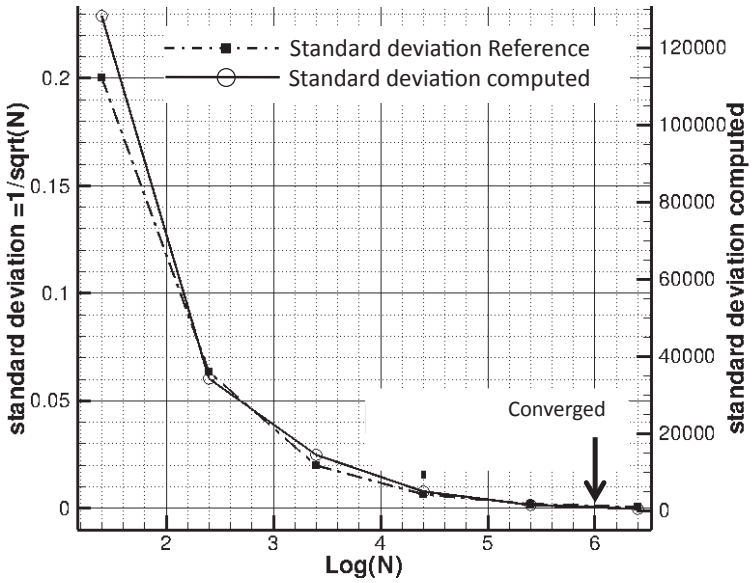

Figure 4.34 – *Verification of the results convergence for one point test case, calculating the exact radiative power of point A at t_1, 40 small computations (which means 40 optical beams, referring to section 4.1.2) · N optical paths generated per computation (per beam)*

where L_m is the length of the element m to be computed (in cm), $k_{m,\nu}$ is the pseudo-absorption coefficient, $Q(T)$ is the partition function of the absorbing molecule for CO_2 and H_2O, $k^*_{m,\nu}$ is the parameter of the CK model, p_s is equal to 1 atm and x is the molar fraction of the considered absorbing species.

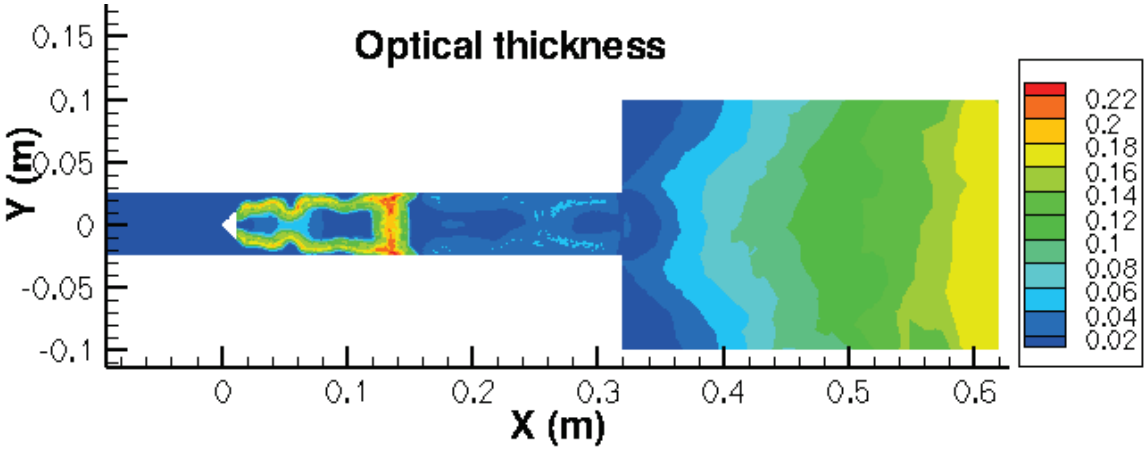

Figure 4.35 – *Optical thickness of each cell with the local temperature and the local molar fraction of the absorbing species CO_2 and H_2O, $k_{m,max}$ used, at $z = 0$*

Fig. 4.35 displays the distribution of the optical thickness in each cell with the local temperature and local molar fraction of the absorbing species CO_2 and H_2O, the maximal $k_{m,\nu}$ is used to obtain the maximal value of the local optical thickness. As the optical path is a measure of the ability of a given path length of gas to attenuate

radiation of a given frequency. A large optical thickness means large attenuation. In the present test case, the large optical thickness is observed in the flame front thanks to the absorption of the burnt gas. And in the cold zone filled with the unburnt gas, this optical thickness is quite small, because there is no CO_2 in unburnt gas and there is almost no absorption.

Evidently, the maximum value is 0.22, so each little cell in the test case area is optically thin. But a whole optical path can be optically thick with a longer length L_m .

Conclusions

A NIFI model is proposed here to improve the performance of ERM Monte Carlo solver. The results of the tests having been performed show that this model works well for the computing zone with temperatures higher than 1500K. On the contrary, due to the slow convergence of ERM model in the cold zone, different methods are used in cold and hot zones, additional work is required to get more satisfying results in the zone with temperatures lower than 1500K.

4.3 A new code "Rainier"

Even after introducing some improvement in the ASTRE code to reduce CPU usage and memory storage, computations with large meshes still cost too much (see Tab. 4.6) to be used directly in actual industrial cases, especially when coupling combustion and radiation. Therefore, a new Monte-Carlo solver "Rainier" has been developed in this thesis including only the ERM model, the CK parameters to describe the radiative properties and some new algorithms, such as a real time convergence control.

4.3.1 Algorithms modified compared with ASTRE

- **Parallel computing approach**

  Fig. 4.36 compares the parallel computing approach of ASTRE code and Rainier code.

  ASTRE code is paralleled by small individual computations (one small individual computation = one beam = a group of optical paths, definition can be found in section 4.1.2). For every individual computation, all the cells in the computational domain are calculated. Each processor deals with several individual computations (Ex. M individual computations) at the same time and there is no master processor here. This parallel algorithm has two disadvantages:

  1. Firstly, if one of these processors has finished its computations before the others, it must wait until all the processors finish their work, which might lead to a waste of CPU time.
  2. Secondly, this algorithm will not run very efficiently on massively parallel computers with a large number of processors. Normally, the objective to divide the

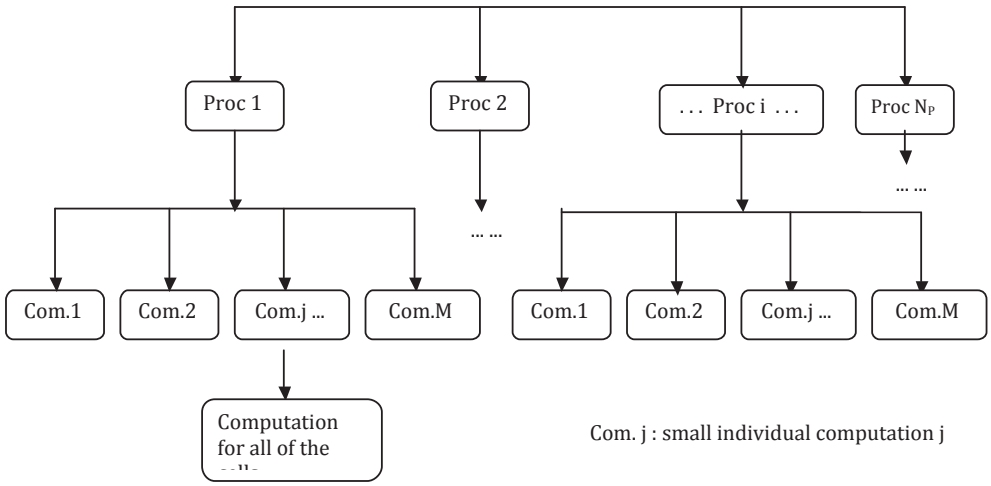

(a) Parallel computing algorithm of ASTRE code

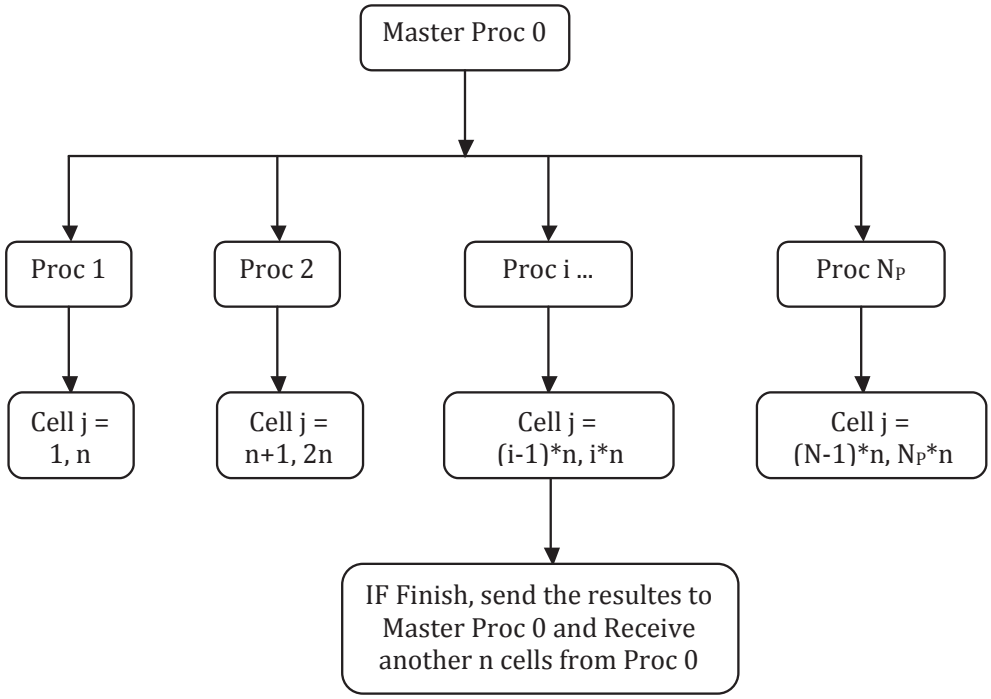

(b) Parallel computing algorithm of RAINIER code

Figure 4.36 – *Parallel computing algorithm flow chart of ASTRE code and RAINIER code*

total number of optical paths into some individual computations is to calculate the standard deviation of the results, illustrated as:

$$Nray_{tot} = Nray_{com} \times \ Nb_{com} \tag{4.21}$$

where $Nray_{tot}$ is the number of the total optical paths, $Nray_{com}$ is the number of the optical paths per individual computation and Nb_{com} is the number of individual computations. The key parameter to control the convergence is $Nray_{com}$ not Nb_{com} as mentioned in section 4.1 , so it will be not useful to increase the number of individual computations. On the other hand, according to the parallel

algorithm, Nb_{com} is $N_p \times M$ where N_p is the number of processor and M is the number of the individual computations performed per processor (Fig. 4.36). So increasing the number of processors will not make the computation more efficient with this algorithm.

Rainier code is parallelized by domain, because cells can be computed independently by using the ERM model. It contains a master processor ($i = 0$) and other executive processors ($i = 1, N$). The master processor is in charge of distributing the task to the executive processors. Firstly, processor 0 tests the states of all of the executive processors, if processor i is free, it will send a package of cells to i and continue to test other processors. When one of these executive processors, for example i, finishes to deal with the package of cells given, it will send a signal 'end' and also the results to master processor, then will receive continuously the next package of cells from the master processor.

Evidently, the advantage of this algorithm is that:

1. Each processor can work continuously without waiting for the others to finish, which contributes largely to the reduction of the CPU time.
2. The efficiency of this code will be largely increased when the number of processors increases.

- **convergence controlling algorithm**

In ASTRE code, the number of optical paths generated from one cell is determined by two spatial distribution techniques NUD and UD as mentioned in section 4.1. With NUD technique, the number of the optical paths originating from each cell is proportional to the emission power of this cell and UD technique applies the same optical path number for all cells. Its disadvantages are:

1. Both cannot control the convergence and execute the computation simultaneously. The convergence such as the standard deviation must be tested after each complete calculation, if it is small enough and is considered to be acceptable, the computation is finished, if not, another computation is needed with a larger number of optical path.
2. The correlation between the local convergence and the local number of optical path is not considered here.

In RAINIER code, a local convergence controlling algorithm is implemented, as shown in Fig. 4.37. The number of the optical paths generated from each cell is not determined before executing the computation and only its maximal value (k_max) is imposed. A test of the local convergence at cell j is performed for every iteration. The actual total number of the optical paths (k) is divided into 10 packages and there is t optical paths in each package. If the ratio of the standard deviation calculated among these 10 packages (σ_j) to the local emission power at cell j (E_j)[4] is lower than the precision (fixed as 0.01 here), then the computation is considered to be converged,

[4]if the local emission at cell j is very small, for example in the zone of unburnt gas, in order to avoid to be divided by 0, an imposed value (ex: $10^2 W/m^3$) is applied to E_j.

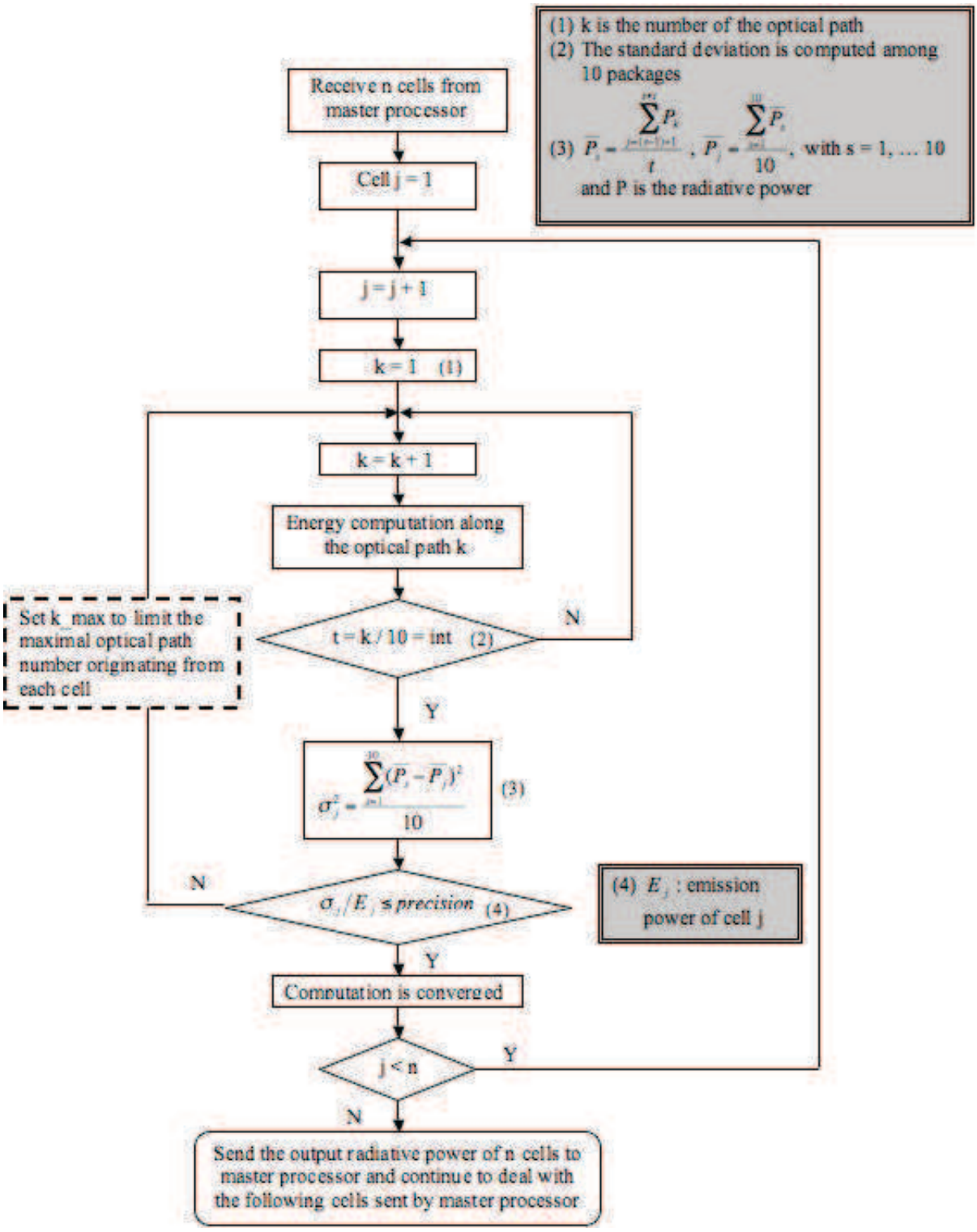

Figure 4.37 – *Local convergence controlling algorithm flow chart of RAINIER code*

the generation of optical path from this cell j is stopped and the processor begins to treat the next cell.

This local convergence controlling algorithm makes possible to relate the local convergence to the local number of optical paths. For the zone like the flame front where the convergence is difficult to achieve, more optical paths are provided, while few op-

tical paths are used in the homogeneous zone which often appear in the combustion computation. This algorithm will largely improve the numerical performance of the code in terms of the reduction of CPU time (the comparison figures and more details will be presented in the next chapter).

4.3.2 Validation of code Rainier

In order to validate Rainier code, its results applied to the test case $\ll Diedre\_3D \gg$ (the same test case than in section 4.2) are compared to the results of ASTRE code which have already been validated against analytical results in Tesse (2001).

Fig. 4.38 shows the radiative power of these two cases on plane $z = 0.002\ m$, evidently, both of them almost give the same results. Specially, these two cases match well in the flame front zone. The little difference near the boundary conditions can be ignored.

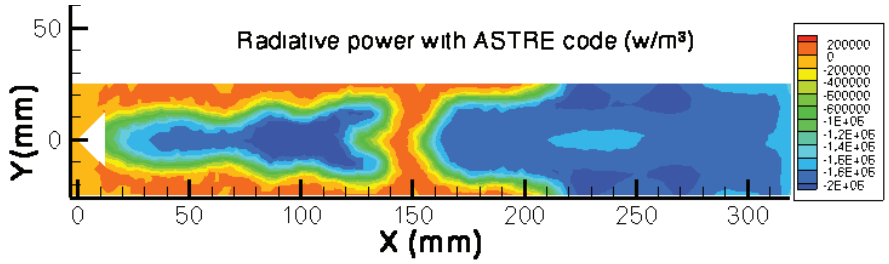

(a) Radiative power with code ASTRE

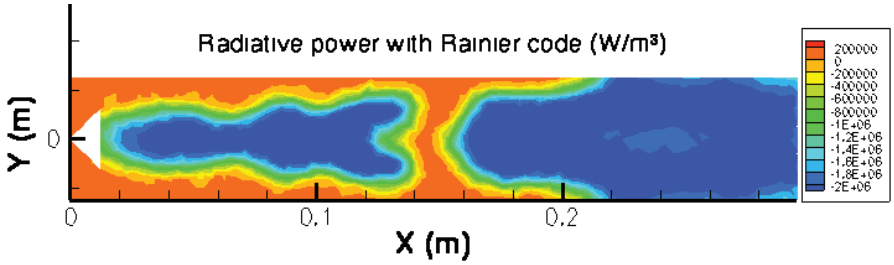

(b) Radiative power with code RAINIER

Figure 4.38 – *Validation of RAINIER code with the results of ASTRE code, Radiative power of case* $\ll Diedre\_3D \gg$, $z = 0.002\ m$

Chapter 5

Comparison between DOM and Monte Carlo methods in large eddy simulation of turbulent combustion

Table of contents

In order to check the new EM2C Monte-Carlo solver Rainier applied to the coupling with large eddy simulations, a comparison with the Discrete Ordinate Method solver DOMASIUM code (Joseph et al. 2003; Joseph 2004), which has already been used for coupled simulations (Goncalves Dos Santos 2008), was performed on a three-dimensional configuration $\ll Diedre\_3D \gg$ in terms of physical behavior of the flame and computational aspects (storage requirement, CPU time and parallel efficiency). Furthermore, as the statistic Monte Carlo method is more precise than the Discrete Ordinate Method (DOM), it is also considered as a reference to validate the DOM model.

5.1 Description of the test case $\ll Diedre\_3D \gg$

5.1.1 Experimental set-up and numerical configuration

The numerical geometry studied here corresponds to an experimental set-up investigated by Knikker (Knikker et al. 2000; Knikker et al. 2002; Knikker et al. 2004) and displayed in Fig. 5.1. A premixed propane/air flow is injected into a rectangular combustion chamber which is 300 mm long (x) and 50 $mm \times 80$ mm in cross section (y, z). The flow rate is fixed to 20 $g.s^{-1}$ corresponding to an upstream mean velocity of about 5 m.s^{-1} (turbulence level about 5%), the equivalent ratio of this premixed flow is chosen as $\phi = 1.0$ and the inlet temperature is 300 K. A stainless steel triangular flame holder (height 25 mm), corresponding to a 50% blockage ratio, is embedded in the lateral windows. A V-shaped turbulent flame stabilized by the hot gases recirculating behind the flame holder is studied.

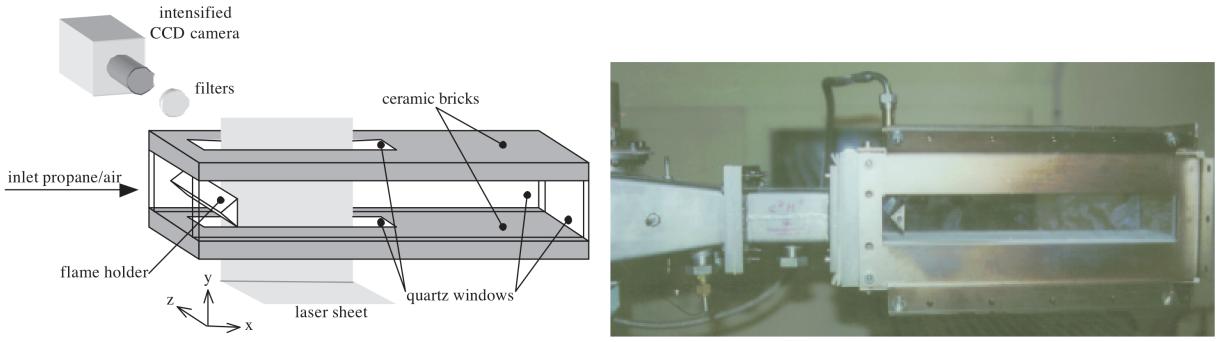

Figure 5.1 – *Experimental set-up of "diedre_3d" retained for numerical simulations investigated by Knikker et al. A turbulent premixed propane/air flame is stabilized downstream of a triangular shape flame holder*

Transparent artificial quartz windows are used to allow to visualize the whole chamber. The upper and the lower walls are made of thick ceramic material for thermal isolation including two narrow windows used to introduce laser sheets.

The computational domain starts 10 cm upstream of the flame holder and continues up to 60 cm downstream as displayed in Fig. 5.2. A zone of 40 cm long and 20 $cm \times 20$ cm in cross section with 'coarse' grid was added at the end of the combustion chamber to reduce the influence of the outlet boundary conditions on the combustion results. A co-flow of nitrogen is injected at 22 m/s and with a temperature equal to 1900 K.

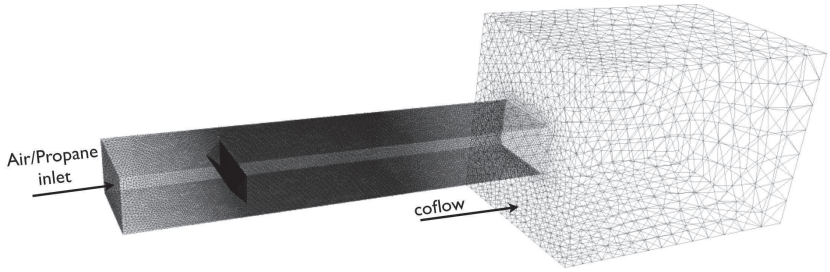

Figure 5.2 – *"Diedre_3d" mesh used by AVBP code with 4.7 millions of tetrahedrons*

The LES mesh for combustion code contains about 4.7 millions tetrahedrons cells, and the grid size has a minimum value $\Delta = 1.0$ mm in the zone near the flame holder (until 15 cm downstream of the flame holder) where lies the recirculation zone. This zone should be well described, because it is responsible for the flame stabilization. Then the grid size is geometrically increased from the end of the recirculation zone up to the burner exit. In the coflow region, a coarser grid is used.

On the other hand, the radiation code uses a different mesh with less cells to reduce required computational time and memory. The physical properties (temperature, mass fraction, etc.) can be transferred from one mesh to another in both directions using a connectivity table. The radiation mesh contains about 3.4 millions tetrahedron cells and the mesh of the recirculation zone is identical to the LES one.

5.1.2 Combustion modeling with AVBP code

For LES computation, a finite volume, second order Runge-Kutta time integration, central second order spatial discretization scheme (Lax-Wendroff scheme) are used in AVBP code. The classical Smagorinsky model based on a sub-grid scale viscosity was used here to model the unresolved turbulent stress tensor. Instead of the thickened flame model (TFLES) which has been discussed in Chapter 2.3.2, here a dynamically thickened flame model (DTFLES) (Legier et al. 2000) is retained. In this formulation, the thickening factor F is not a constant but decreases from F_{max} in flame zones to keep to 1 in non-reactive zones.

About boundary conditions in AVBP code, both the static pressure at the outlet and the velocity components (temperature and species mass fractions) at the inlet are imposed in a soft way through the Navier-Stokes Characteristic Boundary Conditions (NSCBC,Poinsot and Veynante 2005, Poinsot and Lele 1992). The four lateral walls are defined as heat-loss walls using a wall-function approach with zero normal velocity (slip wall). The thermal resistance is estimated to $R_{th} = 0.096$ Km^2W^{-1} in the upper and lower ceramic walls and to $R_{th} = 0.086$ Km^2W^{-1} in the lateral artificial quartz walls. A thermal resistance equal to $R_{th} = 120$ Km^2W^{-1} is set for the aluminum triangular-shaped flame holder. All the other walls (faces (1) to (6) shown in Fig. 5.3) are supposed to be adiabatic slip walls.

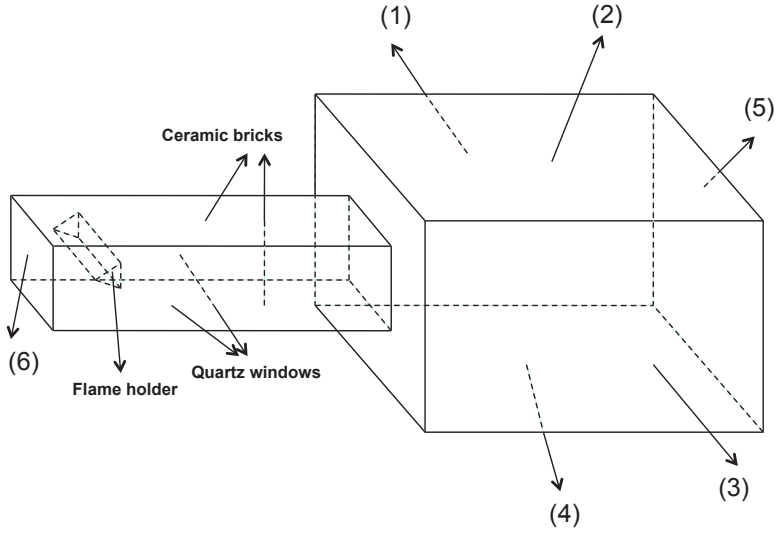

Figure 5.3 – *Boundary conditions of "diedre_3d"*

Concerning the chemical aspect of the combustion modeling, a one step global chemical mechanism is used to represented the chemical reaction between propane and air:

$$C_3H_8 + 5O_2 \longrightarrow 3CO_2 + 4H_2O \tag{5.1}$$

The reaction rate and the chemical parameters are defined in the same way as those of Eq 4.1. Instantaneous fields of the stabilised flame such as temperature, mass fraction of Y_{CO_2} and Y_{H_2O} are respectively displayed in Fig. 5.4, Fig. 5.5 and Fig. 5.6, and are transfered to the radiation code to compute radiative power and fluxes.

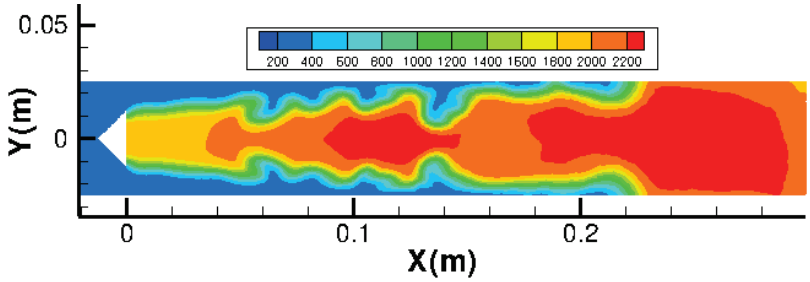

Figure 5.4 – *Field of the instantaneous temperature in plane at z=0, result of AVBP code, "diedre_3d"*

5.1.3 Radiation modeling with "Rainer" code and "Domasium" code

For Rainier code, firstly, the gas radiative properties are treated as in section 4.2 using a correlated-k (CK) model. 44 spectral bands are considered for H_2O and 17 spectral bands for CO_2, with the correlation between the spectral bands of CO_2 and H_2O, 1022 correlated points are used finally (see section 4.1.1 and Appendix A for the details). Secondly, the cut level is fixed as 0.01, that means if the remaining energy carried by an optical ray is lower

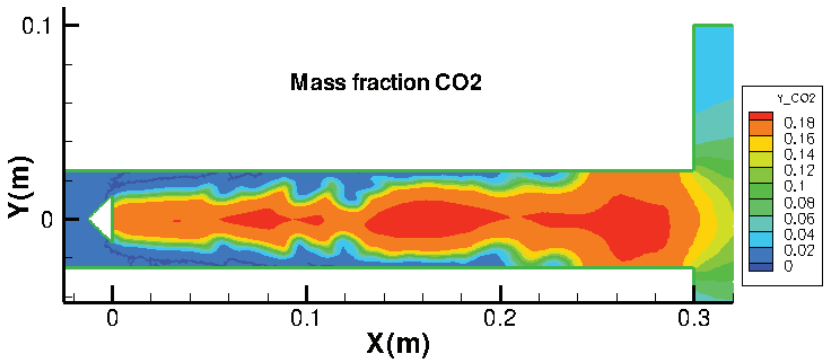

Figure 5.5 – *Field of the instantaneous mass fraction of CO_2 in plane at z=0, Result of AVBP code, "diedre_3d"*

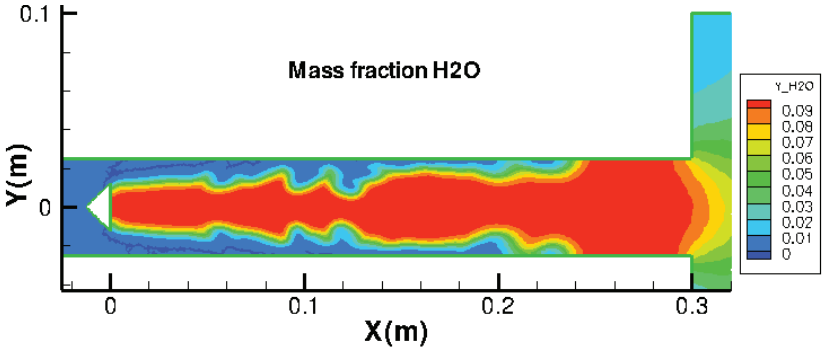

Figure 5.6 – *Field of the instantaneous mass fraction of H_2O in plane at z=0, Result of AVBP code, "diedre_3d"*

than 1% of the energy emitted by the cell where the optical path starts, the optical path is stopped.

All details of the Discrete Ordinate Method computation with code Domasium can be found in the dissertation of Goncalves Dos Santos (2008) and Joseph (2004). The correlated-k (CK) distribution method is used with a reduced number of spectral bands (28 spectral bands for H_2O and 8 spectral bands for CO_2), corresponding to the wavelengths having the most important contributions to the global radiative power. The diamond mean flux scheme (DMFS) and a quadrature of 4th order have been adopted resulting in 24 spectral directions. Additionally, no sub-grid scale radiation model is taken into account in Rainier and Domasium codes.

About the boundary condition, because there is neither reflection nor transmission in Domasium code, all rays reaching the walls are totally absorbed although the emissivities of the four lateral walls and the flame holder are not equal to 1. As the objective of this part is to compare the results between Monte Carlo code and DOM solver, the same computational boundary conditions are requested. The flame holder are considered to be hot blackbodies at a temperature of 1000 K, other walls containing the inlet, the outlet and the four lateral walls are assumed to be cold blackbodies with a temperature of 300 K. The impact of the boundary conditions and the computation with the real wall emissivities and temperature will be studied later in Chapter 6.

5.2 Results and discussions

Fig. 5.7 presents the iso-surfaces of the radiative power computed by ERM model of Monte Carlo solver. In order to show the results more clearly, a 2D slice at $z = -0.002\ m$ has been extracted as displayed in Fig. 5.8.

5.2.1 Local convergence control

Here the number of rays generated from each cell is not set a priori, but tests of convergence are performed for each package of N rays departing from one given cell, which leads to a local convergence control. If the ratio of the local standard deviation to the local radiative power is lower than a fixed criterion (0.01 in this test case), then the calculation is considered as converged. More details are given section 4.3.

Fig. 5.4, Fig. 5.7 and Fig. 5.8 show that the module of the radiative power is maximum in hot gases areas.

Fig. 5.9 shows the distribution of the number of rays for a converged result. Obviously getting convergence is slower in the flame front zone than in others, so more optical paths are needed. On the other hand, in the homogeneous hot gases zone, the number of optical paths requested is rather limited. Here the maximum number of optical paths generated from one cell is fixed to 1000, because with several tests, this value is considered as the minimum value with which the converged results could be obtained.

Fig. 5.10 shows that the maximum standard deviation is found in burnt gas zones where the maximum energy emitted, and it is always lower than 1% of the local radiative power, which corresponds well to the case mentioned above. This local error control can greatly improve the performance of our computations.

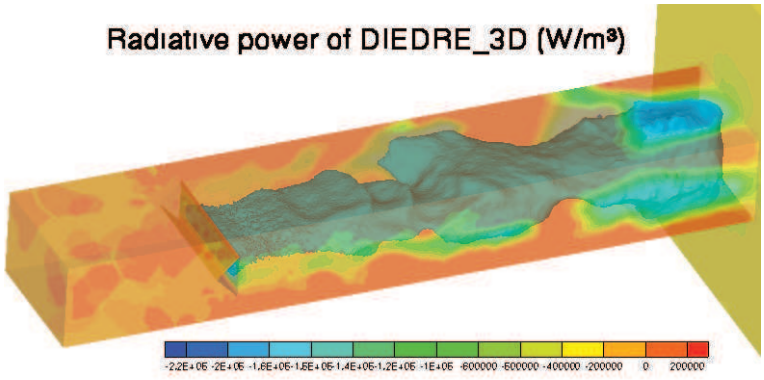

Figure 5.7 – *3D view of the instantaneous radiative power using Monte Carlo Method, converged results, Rainier code, "diedre_3d"*

5.2.2 Comparison with Domasium

The result from Domasium is illustrated in Fig. 5.11. Compared with radiative power of Monte Carlo method displayed in Fig. 5.8, these two results are similar except a small

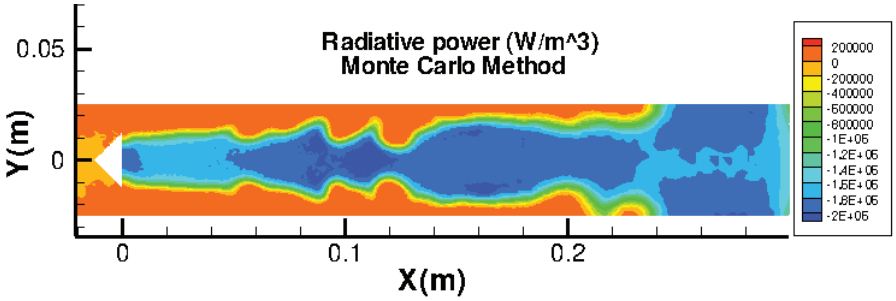

Figure 5.8 – *Instantaneous field of the radiative power in plane z = - 0.002 m, result of Monte Carlo Method, "diedre_3d"*

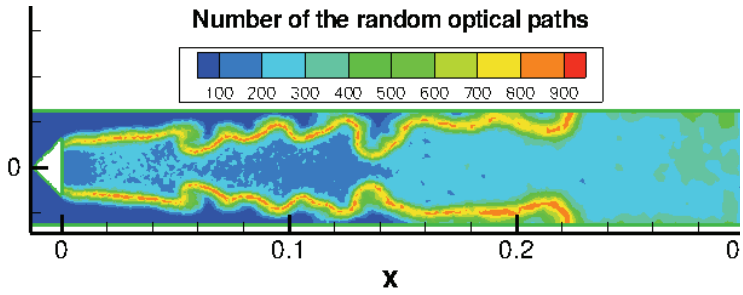

Figure 5.9 – *Instantaneous field of the number of optical rays in plane z = - 0.002 m, maximum value fixed as 1000, result of Monte Carlo Method*

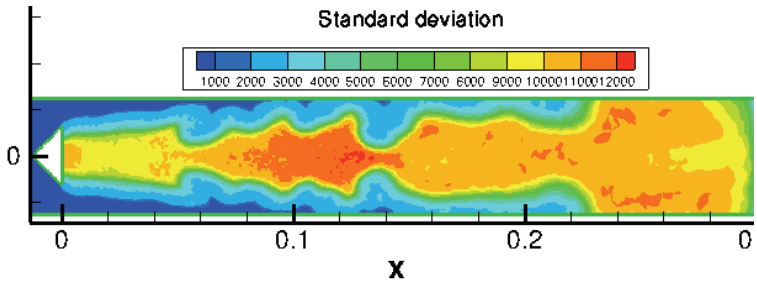

Figure 5.10 – *Cut at z = - 0.002 m of the standard deviation field (unit: W/m^3), converged result of Monte Carlo Method, "diedre_3d"*

difference in the zone near the outlet. This difference might come from the influence of boundary conditions leading to a fluctuation of the results (the boundary conditions are not modeled precisely here with some assumptions taken into account, ex: simplified wall emissivity and simplified wall temperature). In general, we can conclude that these two methods match well in this three dimensional flame holder computation.

To make the comparison more quantitative, two profiles have been extracted at $x = 0.11\ m$ and $x = 0.15\ m$. In the fresh gas zone, the difference is small, then the maximum difference appears in the hot zone rather than in the flame front. This could be due to the fact that in Monte Carlo method the full CK model has been used while in the DOM simulation only 36 correlated points were taken into account. The error between these two methods is about 7% which remains acceptable.

The comparison of the computational performance between these two methods are presented in Tab. 5.1. These computations are carried out on the a SUN cluster in EM2C Laboratory.

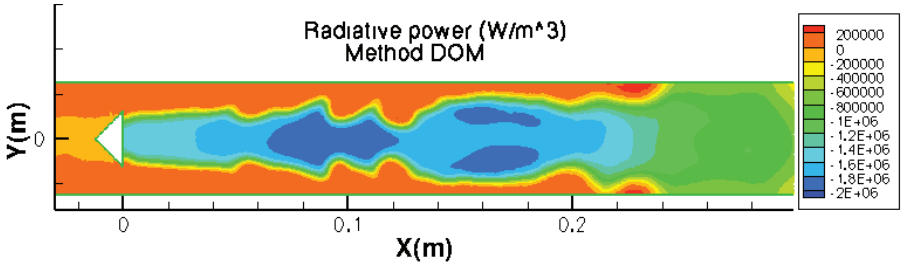

Figure 5.11 – *Plane z = - 0.002 m of the radiative power, result of Discrete Ordinate Method, "diedre_3d"*

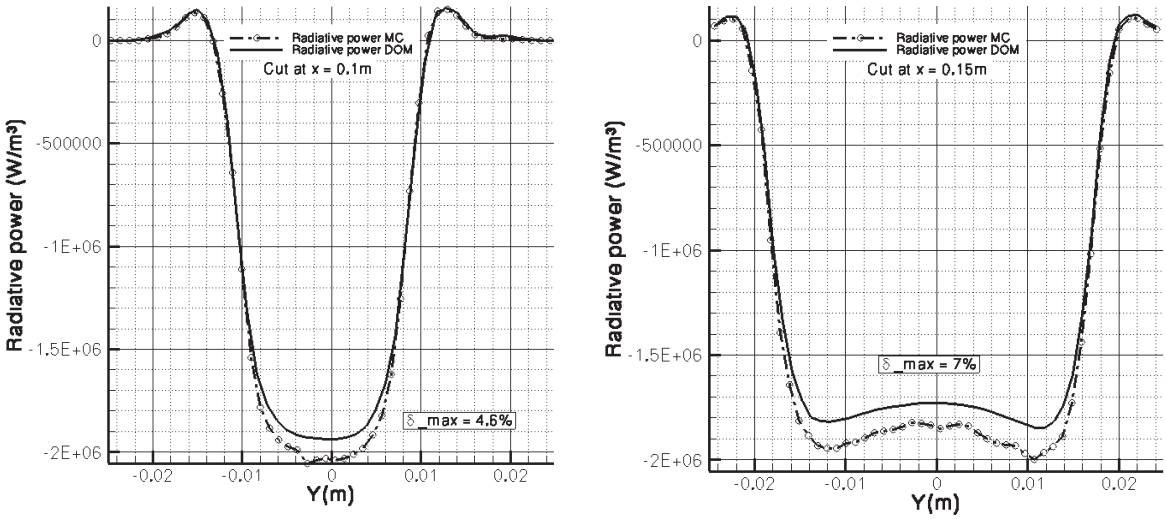

Figure 5.12 – *Comparison of the radiative power between DOM and Monte Carlo, at z = - 0.002 m and x = 0.11 m, x = 0.15 m*

With 72 processors, DOM method requires about 2 minutes and 2G of memory using 36 spectral bands. Monte Carlo method takes about 18 minutes and 0.48G of memory using 1022 spectral bands. Evidently 1022 bands is more precise than 36 bands and also asks for more CPU time, but if we consider the DOM_bis case without using simplifications in terms of the spectral bands, CPU time needed by DOM method will be more expensive than Monte Carlo method (as mentioned in Goncalves Dos Santos (2008), parallelization of Domasium code is made using the spectral bands of CK model, and the technique of band number reduction allows an important gain of computational time). Due to the limits of the computational resource (memory requirement), the calculation of Domasium code with 1022 spectral bands is difficult to achieve. Therefore, here the computation of case DOM_bis has not been performed. But we can assumed it by a simple analytic way: 2 minutes is needed for 36 spectral bands, so 56 minutes (2 minutes* 1022/36) will be needed for 1022 spectral bands, and memory asked for is higher than $2G$, as shown in Tab. 5.1

5.2.3 Conclusion

According to the results of the test cases performed in this chapter:

- Monte Carlo solver (Rainier code) can run well with a machine with available memory

Method	Proc Number	Optical paths	Spectral bands	CPU time	Memory
DOM	72	-	36	2min	2G
Monte Carlo	72	1000_max	1022	18min	0.48G
DOM_bis	72	-	1022	56min	$>$ 2G

Table 5.1 – *Comparison of the computational performance between DOM and Monte Carlo*

lower than 500MB which is acceptable by most computers, while DOM needs at least 2GB memory which is not always available in massively parallel computers. So the feasibility of Monte Carlo could be confirmed.

- It might be concluded that Monte Carlo method spent less time and memory compared to DOM if both of them take into account an accurate description of the radiation properties.

Chapter 6

Influence of the boundary condition in the numerical simulation of the radiative heat transfer coupled with turbulent combustion

Table of contents

6.1 Introduction of the boundary condition problem in radiative heat transfer

In order to simplify the problem and reduce the CPU time of radiative heat transfer simulations coupled with turbulent combustion, boundary conditions were simplified in the precedent chapters. In this chapter, we also begin with a simple case (noted **case1**) as illustrated in Fig. 6.1, supposing that emissivities are equal to unity for all of the boundaries and wall temperatures are imposed to the same value as the one of the gas close to them. In fact, **case1** is different from the boundary conditions used in the precedent chapter, wall temperatures are imposed to 300K and the temperature of the flame holder is equal to 1000K in Chapter 5.

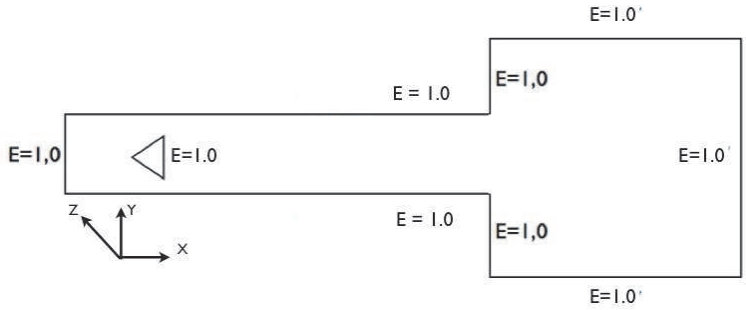

Figure 6.1 – *Case 1: wall emissivities* $\varepsilon = 1.0$ *(presented by E in the figure) in plan* $z = 0$.

In his thesis, Goncalves Dos Santos (2008) mentioned that one of the most important future works is to refine the description of boundary conditions including reflective walls in the radiation code and radiative heat fluxes in boundary conditions of the combustion code. So in the following part, the wall reflectivity with the real wall emissivity will be taken into account and then be compared to the simplified case. All the calculations in this chapter are performed with the configuration $\ll Diedre\_3D \gg$ presented in Chapter 5.

6.2 Flux calculation at the boundaries

Before presenting the influence of the different boundary conditions, fluxes will be computed at first.

6.2.1 Flux computation notions used

The radiative surface fluxes characterize the radiative power exchanged between the opaque body and the radiation field (Fig. 6.2), where "opaque body" can absorb or reflect the incident energy, but no optical ray can be transmitted. Without special remark, walls in this section are considered as "opaque body" by default. Fluxes are given by:

$$\varphi^R = \varphi^e - \varphi^a = \vec{q} \cdot \vec{n} \tag{6.1}$$

where φ_e and φ_a (arithmetic values) respectively denote the flux emitted and absorbed

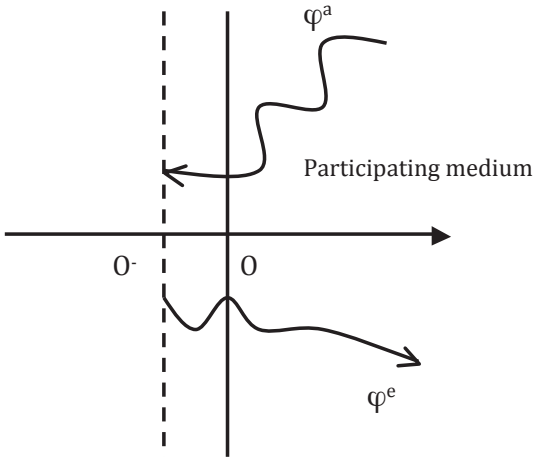

Figure 6.2 – *Radiative flux definition, from the point of view of the opaque wall*

by the "opaque body" at point o^-, here o^- is one side of the interface between wall and medium and it is used when the object studied is the wall, the other side is represented by o which will be used when the object studied is the medium. $\vec{q}^R$ is the radiative flux vector and $\vec{n}$ is the unit normal vector of the surface treated oriented towards the gaseous medium.

6.2.2 Results and discussions

Flux computations have been performed on the configuration $\ll Diedre\_3D \gg$ with the different boundary conditions (different boundary wall temperature) considering wall specular reflection. The objective of this section is to validate the flux calculation with code Rainier, so emissivity used here is that of Case 1 as shown in Fig. 6.1.

The figures below show:

1. Flux on wall surface (x, y) at $z = -0.04\ m$ (lateral wall)
2. Flux on wall surface (x, z) at $y = 0.025\ m$ (top wall)
3. One-dimensional profiles extracted from the previous figures (cut at $x = 0.16\ m$ in plan $z = -0.04\ m$ and cut at $z = 0.0\ m$ in plan $y = 0.025\ m$).

These calculations are performed with different wall temperatures (Tab. 6.1):

1. With the temperature 300 K: cold boundary condition with the atmosphere temperature
2. With the temperature 1000 K: intermediate boundary condition with an intermediate temperature between the atmosphere temperature and the fluid temperature
3. With the temperature of the fluid closed to the walls: hot boundary condition with the fluid temperature, it might give a reference for the results analysis.

Test	Temperature (K)
Test 1	300
Test 2	1000
Test 3	Fluid temperature (convection is not taken into account)

Table 6.1 – *Three tests with different wall temperatures*

Figures 6.4 to 6.12 show the instantaneous radiative fluxes (the instantaneous time t is the same as that in chapter 5) for the three above cases with different wall temperatures. Tab. 6.2 illustrates the total flux integrated through all the boundaries for these three cases. Temperature and mass fractions profiles of the gas medium are the same as Fig. 5.4 and Fig. 5.7. Additionally, temperature profiles at plan $z = -004\ m$ and plan $y = 0.025\ m$ for **test3** are illustrated in Fig. 6.3:

- As shown in Fig. 6.4 - Fig. 6.6, with lower wall temperature (300 K), the wall absorption is dominant compared with wall emission. So the flux value is positive (in this test, defining that energy absorbed is positive and energy emitted is negative). Additionally, the fluctuations of results are quite strong. Because ERM method converges less quickly for cold zones as mentioned in section 4.1, it requires more optical paths (computation time) to be converged. In this test, all three cases with different wall temperatures use the same conditions in terms of convergence (the same maximum optical paths), so the case with $T = 300\ K$ gets more fluctuations compared to others (with higher temperature).
- As shown in Fig. 6.7 - Fig. 6.9, with the wall temperature increasing (ex: 1000 K), the flux change from positive value to negative value, which means that wall emission increases and becomes dominant compared to wall absorption. Additionally, the fluctuations of results decrease, it means that the convergence state becomes better than lower temperature case ($T = 300\ K$), which corresponding to the conclusion of section 4.1. ERM method gets converged more quickly for the zone with higher temperature.
- As shown in Fig. 6.10 - Fig. 6.12, when the wall temperature is equal to the fluid temperature next to wall. The flux profile is quite similar as that of temperature (see Fig. 6.3). Emission is dominant (flux is negative) for the hot zone and absorption is dominant (flux is positive) for the cold zone. Additionally, results fluctuations are quite small, computation is well converged.

Summarizing these threes cases, from the point of view of computational performance, as mentioned before, the numerical Monte Carlo method used in this thesis "ERM" works better for the hot zone than the cold zone. As a result of that, the calculation with low

Test	Temperature (K)	Flux integration (w)
Test 1	300	4.4×10^3
Test 2	1000	-1.79×10^4
Test 3	Fluid temperature	-2.02×10^5

Table 6.2 – *Flux integrations through all the boundaries for the three tests with different wall temperatures*

temperature ($T = 300\ K$) gets convergence less quickly than that with high temperature ($T = T_F$). So in order to make the computation converged, more optical paths are needed for **test1**.

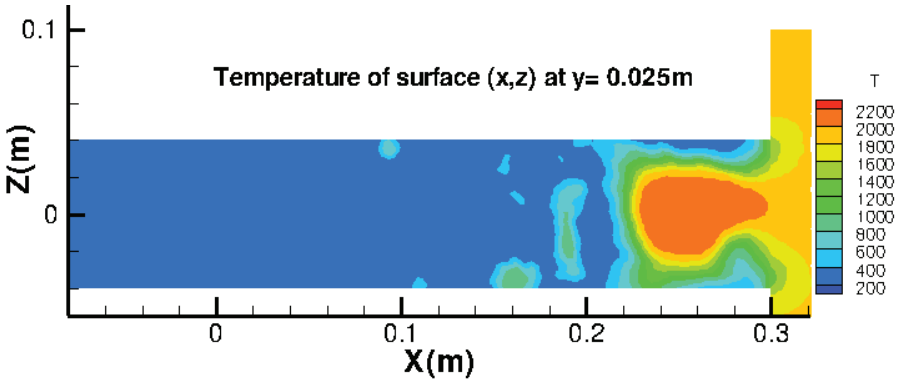

(a) Instantaneous field of the $y = 0.025\ m$ surface temperature

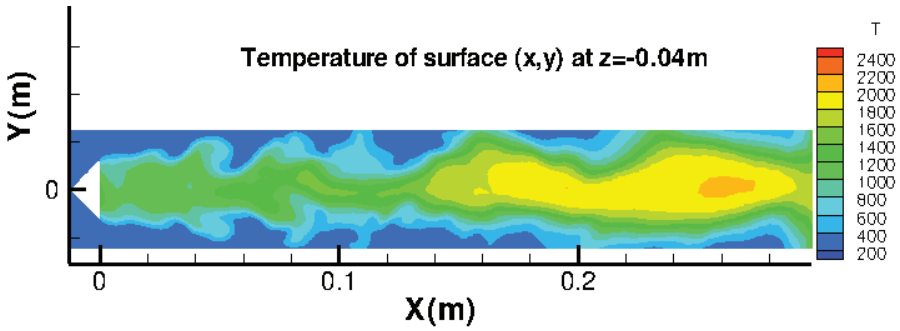

(b) Instantaneous field of the $z = -0.04\ m$ surface temperature

Figure 6.3 – *Temperature in plans $z = -0.04\ m$ and $y = 0.025\ m$ for case **test3**, $\varepsilon = 1.0$, $T_{wall} = T_F$*

To conclude, all of the results are consistent with the radiative power results calculated in Chapter 5, and are physically correct. They can then give an evidence for the validation of Rainier flux computations part.

Test1: $\varepsilon = 1$, $T = 300\ K$

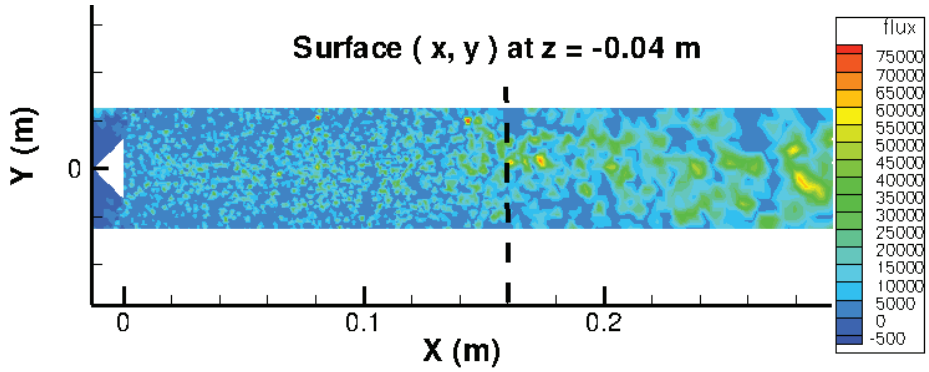

Figure 6.4 – *Instantaneous radiative flux, in plan* $z = -0.04\ m$, $\varepsilon = 1.0$, $T_{wall} = 300\ K$

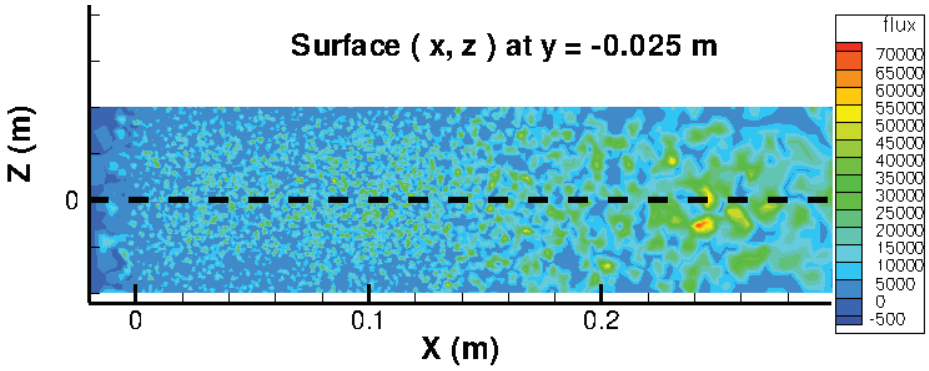

Figure 6.5 – *Instantaneous radiative flux, in plan* $y = 0.025\ m$, $\varepsilon = 1.0$, $T_{wall} = 300\ K$

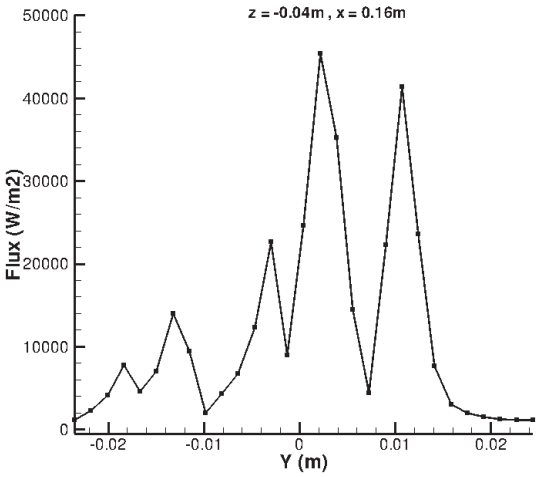

(a) surface (x,y) at $z = -0.04\ m$ and $x = 0.16\ m$

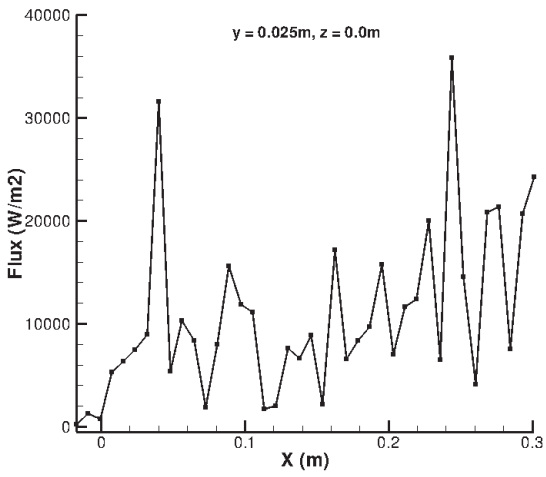

(b) surface (x,z) at $y = 0.025\ m$ and $z = 0.0\ m$

Figure 6.6 – *Flux profiles extracted from Fig. 6.4 and Fig. 6.5,* $\varepsilon = 1.0$, $T_{wall} = 300\ K$

Test2 : $\varepsilon = 1$, $T = 1000\ K$

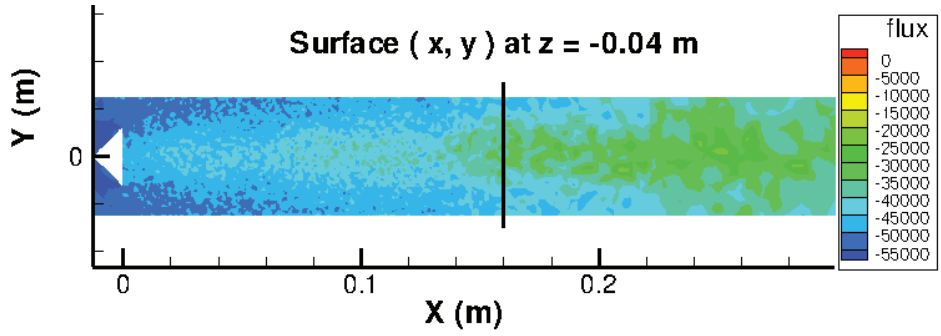

Figure 6.7 – *Instantaneous radiative flux in plan* $z = -0.04\ m$, $\varepsilon = 1.0$, $T_{wall} = 1000\ K$

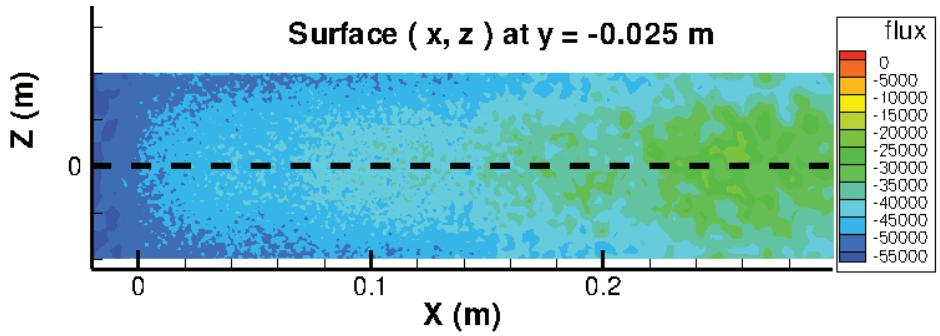

Figure 6.8 – *Instantaneous radiative flux in plan* $y = 0.025\ m$, $\varepsilon = 1.0$, $T_{wall} = 1000\ K$

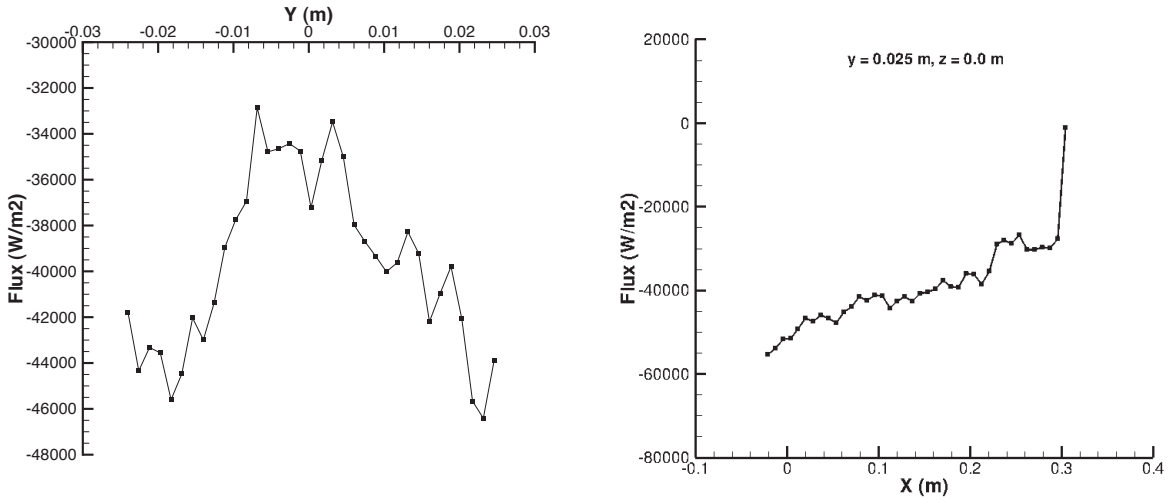

(a) surface (x,y) at $z = -0.04\ m$ and $x = 0.16\ m$ (b) surface (x,z) at $y = 0.025\ m$ and $z = 0.0\ m$

Figure 6.9 – *Flux profiles extracted from Fig. 6.7 and Fig. 6.8,* $\varepsilon = 1.0$, $T_{wall} = 1000\ K$

Test3 : $\varepsilon = 1$, $T =$ *Fluid temperature next to wall* K

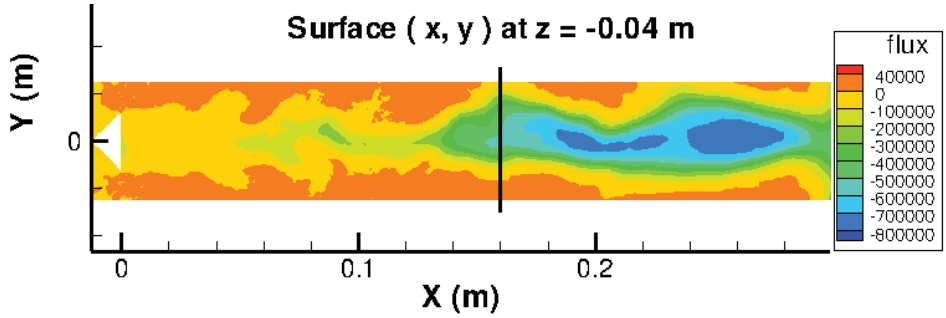

Figure 6.10 – *Instantaneous radiative flux, in plan* $z = -0.04\ m$, $\varepsilon = 1.0$, $T_{wall} = T_F\ K$

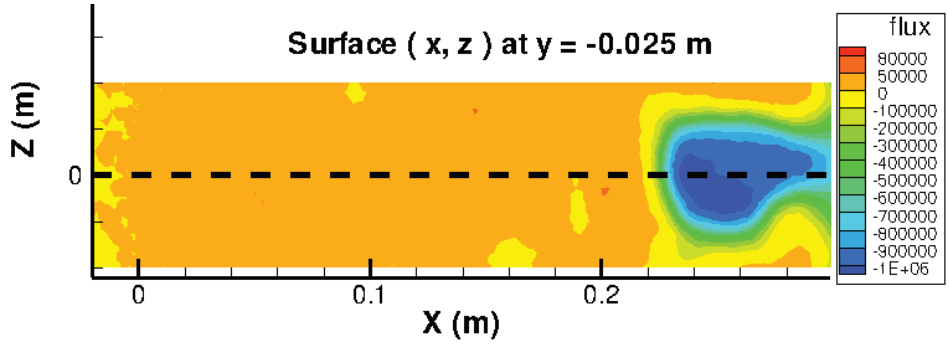

Figure 6.11 – *Instantaneous radiative flux, in plan* $y = 0.025\ m$, $\varepsilon = 1.0$, $T_{wall} = T_F\ K$

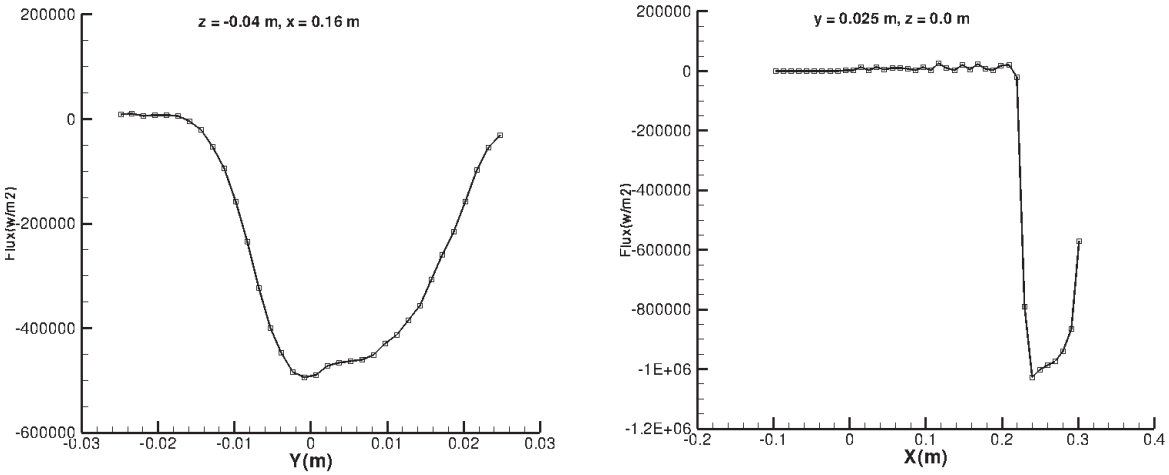

(a) surface (x,y) at $z = -0.04\ m$ and $x = 0.16\ m$ (b) surface (x,z) at $y = 0.025\ m$ and $z = 0.0\ m$

Figure 6.12 – *Flux profiles extracted from Fig. 6.10 and Fig. 6.11,* $\varepsilon = 1.0$, $T_{wall} = T_F\ K$

6.3 Comparison of radiative results with different boundary conditions

6.3.1 Emissivity

Influence of the emissivity at the combustion chamber outlet

Different from **Case 1**, here in **Case 2**, emissivity is equal to 0 at the outlet of the tank as illustrated in Fig.6.13. A comparison between **Case 1** and **Case 2** is performed to study the influence of the boundary condition at the outlet.

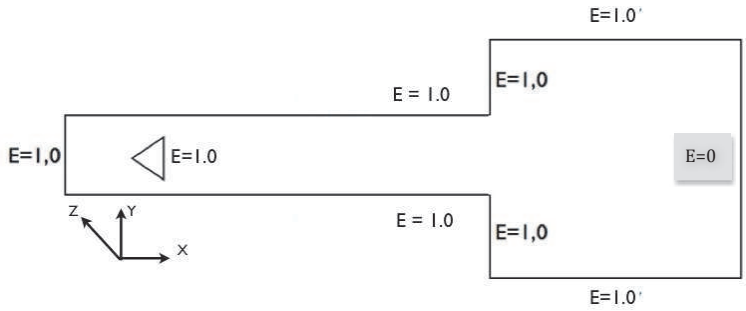

Figure 6.13 – *Case 2: emissivity of the boundary condition $\varepsilon = 0$ (presented by E in the figure) at the outlet of the tank and $\varepsilon = 1.0$ for other walls*

Fig. 6.14 shows the radiative power in plan (x,y) using the emissivity of **Case2**. Comparing with Fig. 5.8 in Chapter 5, the maximum emission power is larger, because the wall temperatures used here are the temperatures of the fluid next to the wall instead of 300 K used in Chapter 5. If the wall reflexion is considered, the medium will have more emission power coming from the walls.

The radiative power at different locations($x = 0.01\ m, 0.05\ m, 0.10\ m, 0.15\ m, 0.20\ m$ and $0.25\ m$) in plan (x,y) between **Case 1** and **Case 2** are compared. These two results match very well as illustrated in Fig. 6.15. Except for the zone near the outlet of the flame chamber where differences due to the influence of the boundary condition is present.

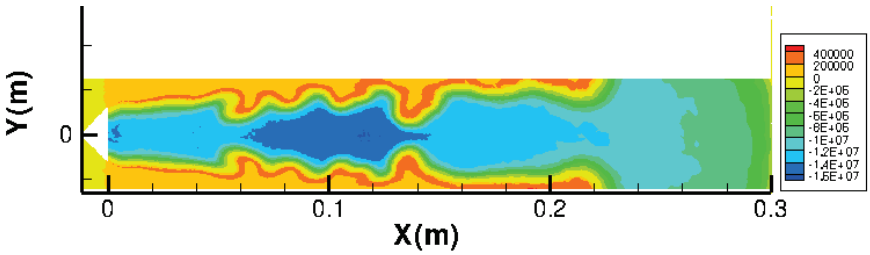

Figure 6.14 – *Radiative power in plan (x,y), $z = 0$, Case 2*

To conclude, the impact of the emissivity at the outlet on the radiative power of the flames in this combustion chamber can be neglected. So we can change the emissivity of the

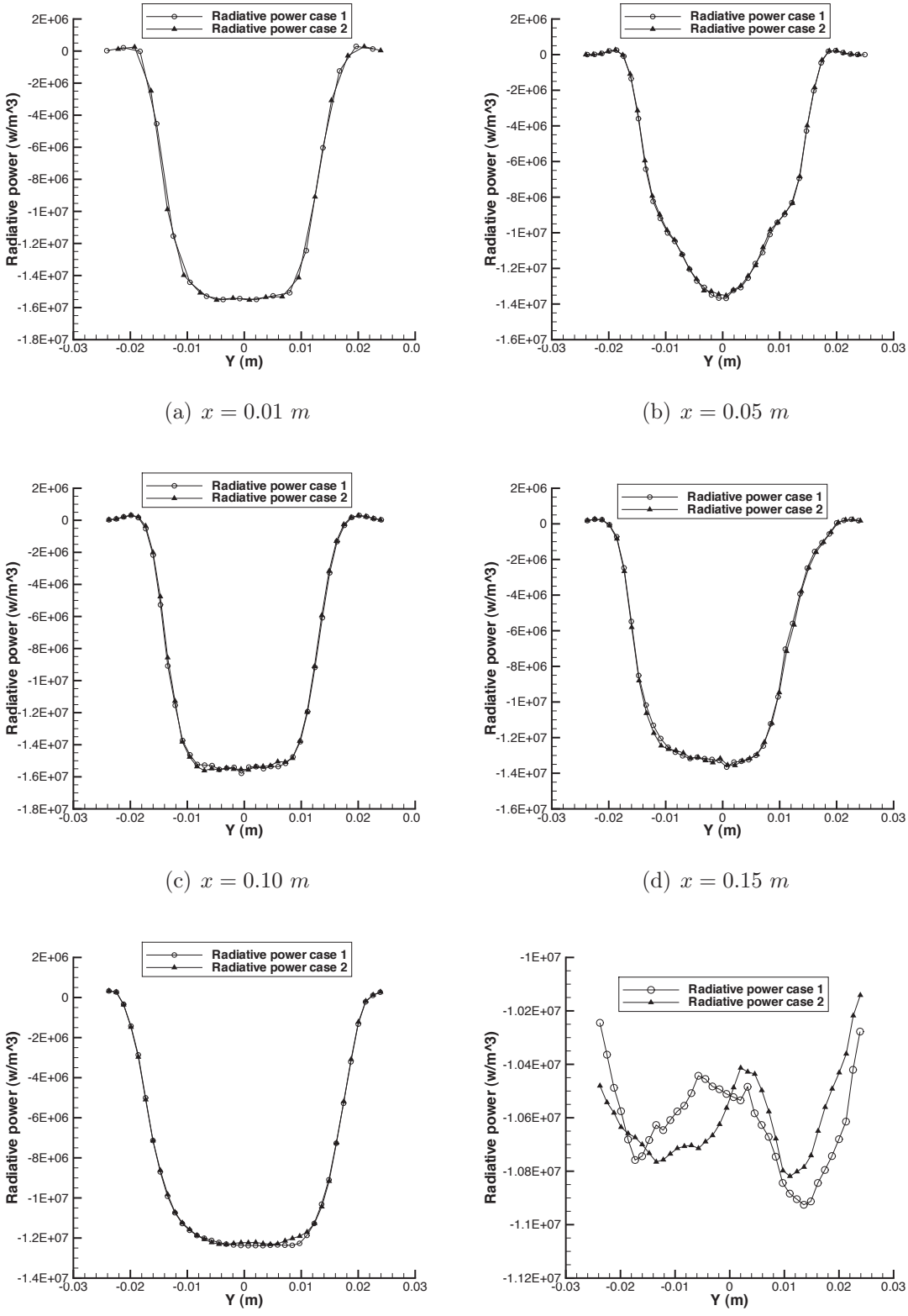

(a) $x = 0.01\ m$ (b) $x = 0.05\ m$

(c) $x = 0.10\ m$ (d) $x = 0.15\ m$

(e) $x = 0.20\ m$ (f) $x = 0.25\ m$

Figure 6.15 – *Comparisons of the radiative power between case 1 and case 2, extracted in plan (x,y), $z = 0$.*

outlet without changing the radiative characteristics of the flame, for example, choosing the different material of the outlet, adding a chimney, etc.

Influence of the emissivity of the combustion chamber lateral walls

In **Case 3**, actual emissivity is used for the four lateral walls. The material used for the walls at top and at bottom is ceramic bricks, so emissivity is equal to 0.91 as shown in Fig. 6.16. Other walls are made of the clear fused quartz 124 (used in our experimental facilities). Their curves of emissivity are on function of the wavelength which is provided by the manufacturer in Fig. 6.17. The spectral range presented in this figure corresponds to the CK spectral range database used in our simulation. On the other hand, the emissivity for other walls remain the same value as **Case 1**.

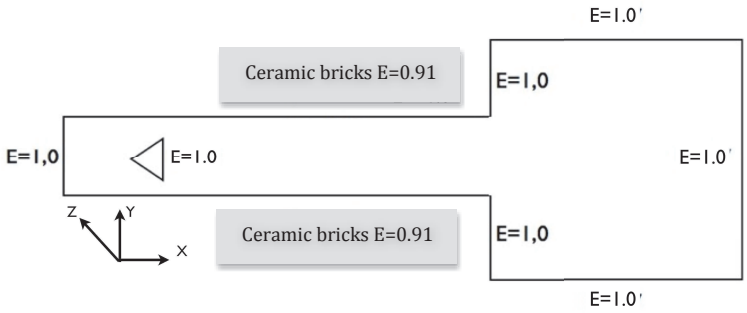

Figure 6.16 – *Case 3: real emissivity used for the ceramic walls* $\varepsilon = 0.91$ *displayed in plan (x,z)*

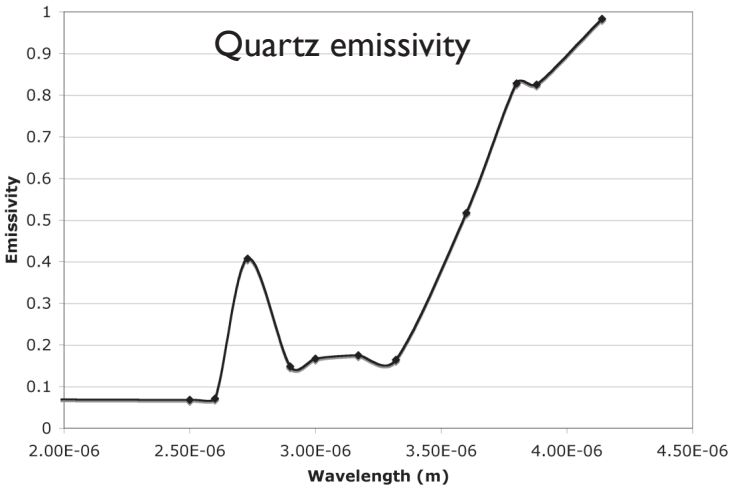

Figure 6.17 – *Case 3: Clear fused quartz 124 emissivity on function of the wavelength, used for the two walls at the plan (x,y), provided by the manufacturer, Goncalves dos Santos (2008)*

Radiative power profiles extracted at $x = 0.01\ m$ and $x = 0.015\ m$ from the plan $z = 0$ are compared in Fig. 6.18 for **Case 1** and **Case 3**. Evidently, the emission power is more important with the actual emissivity of the wall. Because walls absorb less energy using

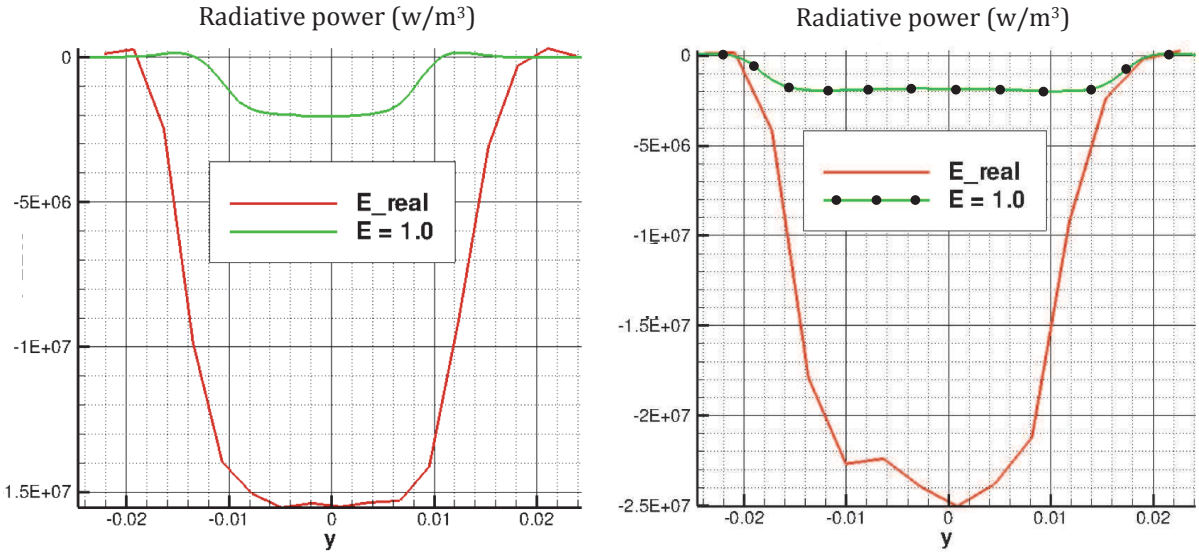

(a) x=0.01m (b) x=0.015m

Figure 6.18 – *Comparison of the radiative power between the case 2 and the case 3, value extracted in plan $z = 0$ at $x = 0.01m$, $x = 0.015m$*

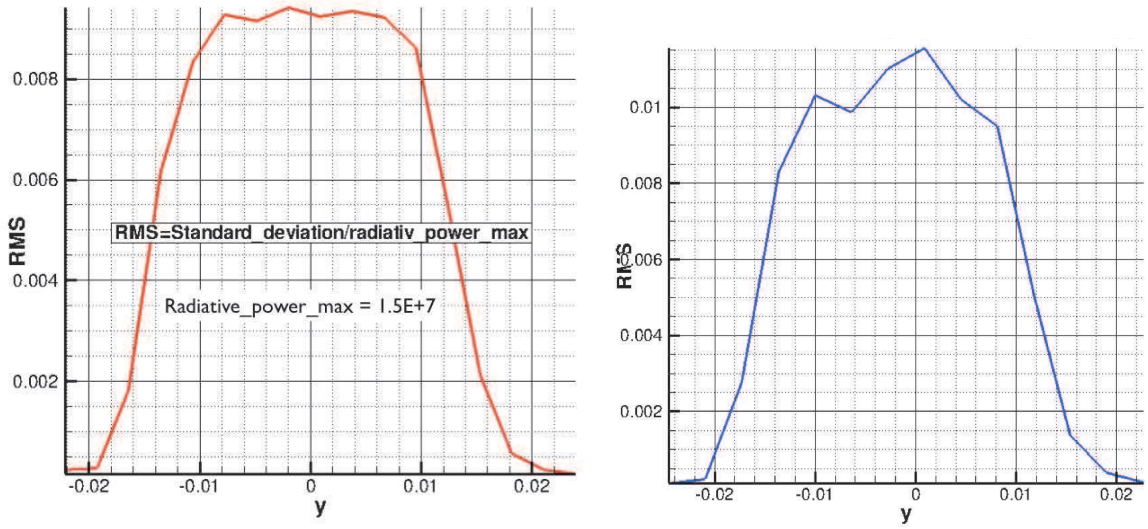

(a) x=0.01m (b) x=0.015m

Figure 6.19 – *Standard deviation of the radiative power computed in case 3 divided by the maximum radiative power, value extracted in plan $z = 0$ and $x = 0.01m$, $x = 0.015m$, without unity*

the actual emissivity compared to case $\varepsilon = 1$, the energy remaining in the domain will be higher. Although at the same time, wall with the actual emissivity will emit less energy, but this effect is not dominant[1]. Noting that the difference of radiative power between these

[1]Attention: emissivity impact might be overestimated here, because the temperature taken into account is not the real wall temperature, it is the temperature of the fluid next to the boundary which is a big approximation. Therefore, the difference of the radiative power between these two cases should be less.

two cases is large enough and cannot be neglected, so to correctly consider the lateral wall emissivity is important to simulate the radiation phenomena in the combustion chamber. However the case with the actual emissivity will take much more CPU time than the other one, largely due to the fact that reflection should be taken into account.

Remarks:

The two figures shown in Fig. 6.19 present the standard deviation of **Case 3** and confirm that the case with reflection is converged.

6.3.2 Wall temperature

In general, due to the difficulty to determine exactly the actual wall temperatures in coupled simulations of radiation and combustion in a combustion chamber, the walls are considered to have the same temperature as the fluid next to it or to imposed a priori the wall temperature such as 300 K or 1000 K. Evidently, this approximation will bring some numerical errors. In this part, transfer convection will be taken into account to estimate the actual wall temperature in order to model the radiation near the wall as accurately as possible. Firstly, this calculation will be performed theoretically to evaluate the error produced by neglecting convection phenomenon, then the case where convection can be ignored will be discussed. Finally, if necessary (that means after theoretical calculation, if the convection plays an important role), the results with the actual wall temperature will be compared to the results with the approximated wall temperature to study the influence of the wall temperature on the radiative power of the combustion chamber computation.

Forced convection taken into account

Fig. 6.20 shows briefly one part of the combustion chamber focused on the boundary conditions taking into account the influence of the forced convection.

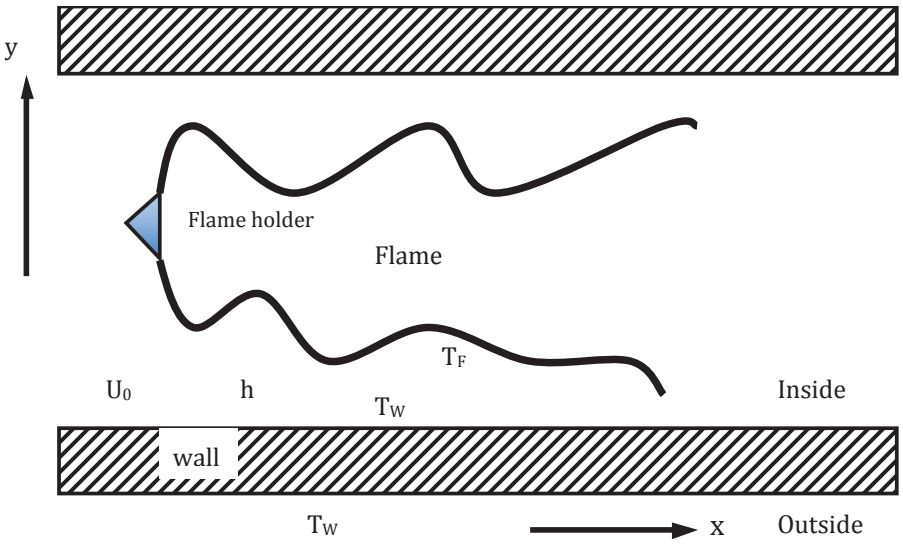

Figure 6.20 – *Computation of the real wall temperature taking into account forced convection, the wall thickness is neglected here*

Choosing a cell i from the wall as the target portion to be studied, the balance energy equation about this cell i can be written as:

$$\phi_F^R + \bar{h} \cdot (T_F - T_W) = \phi_W^R \tag{6.2}$$

The left side of this equation describes the radiative flux from the gas to the wall (ϕ_F^R) and the forced convection between the fluid and the wall ($\bar{h} \cdot (T_F - T_W)$), and the right side describes the radiative flux from the wall to the atmosphere (ϕ_W^R).

Determination of convection transfer coefficient $\bar{h}$

$\bar{h}$ ($W \cdot m^{-2} \cdot K^{-1}$) is the average convection transfer coefficient and can be expressed from the Nusselt number (Taine et al. 2003) :

$$\frac{\bar{h} \cdot L}{\lambda} = Nu_L \tag{6.3}$$

where L is the combustion chamber length in our test case (x direction), λ is the conductive heat transfer coefficient on the gas. The Nusselt number Nu_L is the ratio of convective to conductive heat transfer across (normal to) the boundary.

According to the equation 6.3, in order to determine $\bar{h}$, the Nusselt number should be specified. This case can be classified as "internal forced convection, rectangular channel, turbulent flow" case (Fig. 6.21). Referring to the "Sieder and Tate" equation (Siegel and Tate 1936), the Nusselt number can be estimated as:

$$Nu_b = 0.027 \cdot Re_b^{0.8} \cdot Pr^{\frac{1}{3}} \cdot \left(\frac{\mu_m}{\mu_p}\right)^{0.14} \tag{6.4}$$

where μ_m and μ_p are respectively the viscosity obtained at the average temperature of the gas and at the wall temperature. In this study, we neglected this difference, so μ_m/μ_p is supposed equal to unity. The local Reynolds number Re_b at the location b is written as:

$$Re_b = \frac{\rho \cdot u_0 \cdot b}{\mu} \tag{6.5}$$

and the Prandtl number is:

$$Pr = \frac{\mu \cdot c_p}{\lambda} \tag{6.6}$$

with density ρ, dynamic viscosity μ and specific heat capacity c_p.

Then the value of each term in equation 6.4 can be determined as:

- For the gas case, Prandtl number is about 0.7 (Taine et al. 2003).
- In the actual test case, using the configuration presented in Chapter 5, the value of the parameters b and L are respectively 0.05 m and 0.3 m. The velocity u_0 is 5 m/s.
- Referring to the gas characteristic at the different temperature illustrated in Tab. 6.3, Tab. 6.4, Tab. 6.5 and Tab. 6.6 (Taine et al. 2003), the approximate Reynolds number and Nusselt number can be calculated as shown in Tab. 6.7 (Kee et al. 1986).

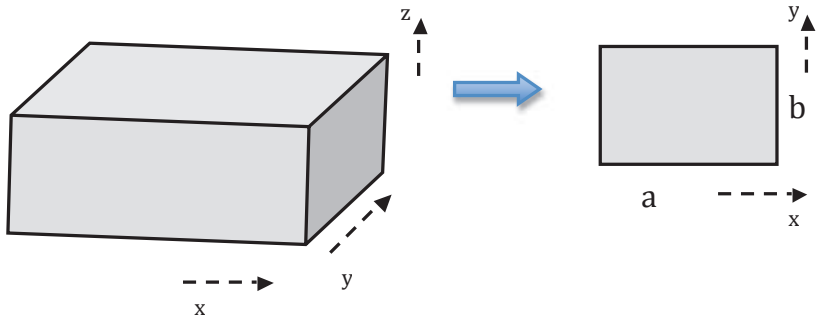

Figure 6.21 – *Rectangular channel dimension for Sieder and Tate equation*

Temperature (K)	$\rho_{air}\ (kg/m^3)$	$\mu_{air} \cdot 10^5\ (N \cdot s/m^2)$	$\lambda_{air} \cdot 10^2 (W/mK)$
300	1.1614	1.846	2.63
800	0.4354	3.698	5.73
1300	0.2679	4.960	8.2
2300	0.1513	7.66	17.5

Table 6.3 – *Air characteristics at atmosphere pressure for different temperatures*

Temperature (K)	$\rho_{O_2}\ (kg/m^3)$	$\mu_{O_2} \cdot 10^5\ (N \cdot s/m^2)$	$\lambda_{O_2} \cdot 10^2 (W/mK)$
300	1.284	2.072	2.68
800	0.4810	4.152	5.89
1300	0.2960	5.884	8.71

Table 6.4 – *O_2 characteristics at atmosphere pressure for different temperatures*

Temperature (K)	$\rho_{CO_2}\ (kg/m^3)$	$\mu_{CO_2} \cdot 10^5\ (N \cdot s/m^2)$	$\lambda_{CO_2} \cdot 10^2 (W/mK)$
300	1.7730	1.49	1.655
800	0.6614	3.37	5.51

Table 6.5 – *CO_2 characteristics at atmosphere pressure for different temperatures*

Temperature (K)	$\rho_{H_2O}\ (kg/m^3)$	$\mu_{H_2O} \cdot 10^5\ (N \cdot s/m^2)$	$\lambda_{H_2O} \cdot 10^2 (W/mK)$
300	0.5863	1.271	2.46
800	0.2739	2.969	6.37

Table 6.6 – *H_2O characteristics at atmosphere pressure for different temperatures*

Now the value of $\bar{h}$ can be determined according to Eq. 6.3 using the value of Re and Nu obtained in the Table above. Here $\bar{h}$ is just determined approximately. The aim is to find the maximum value of $\bar{h}$, because if the term $[\bar{h} \cdot (T_F - T_W)]$ is small enough compared with the other two terms ϕ_F^R and ϕ_W^R in Eq. 6.2, neglecting the effect of the thermal forced convection in this calculation will not result in important computation errors and it will be

T (K)	$\rho\ (kg/m^3)$	$\mu \cdot 10^5\ (N \cdot s/m^2)$	$\lambda \cdot 10^2 (W/mK)$	Re	Nu
800	0.4342	3.522	5.34	3082	14.82

Table 6.7 – *Reynolds number and Nusselt number calculation*

not necessary to take into account the convection in this kind of simulation, on contrary, if the influence of convection is not neglecting, then it should be useful to consider it.

In fact, the value of Nu in Tab. 6.7 has already be overestimated due to the corresponding Reynolds number overestimating. The reason is that: this calculation in Tab. 6.7 is performed at the temperature chosen equal to 800 K, however in reality, the burnt gas temperature is much higher than 800 K (the maximum value can reach about 2300 K), so the average gas density ρ should be much smaller and the dynamic viscosity μ should be much larger (the evaluation of these parameters depending on the temperature is shown in Tab. 6.3, Tab. 6.4, Tab. 6.5 and Tab. 6.6) and it causes that the value of Re shown in Tab. 6.7 is large enough to cover the cases with temperature higher than 800 K. As having been explained in the precedent paragraph, in order to find the maximum value of $\bar{h}$, using Re_{max} to calculate Nu_{max}, then using Nu_{max} to calculate $\bar{h}_{max}$ with the maximum value of λ, referring to the table above, $\lambda = 17.5 \cdot 10^{-2}(W/mK)$ is chosen here, so finally[2]:

$$\begin{aligned} \bar{h}_{max} &= Nu_{max} \cdot \lambda_{max}/L \\ &= 14.818 \cdot 17.5 \cdot 10^{-2}/0.3 \\ &= 8.64\ (W \cdot m^{-2} \cdot K^{-1}) \end{aligned} \tag{6.7}$$

Determination of the flux ϕ_F^R

ϕ_F^R is the radiative flux emitted from the gas of the boundary to the wall. It can be computed directly by "Rainier" code.

Determination of the flux ϕ_W^R

ϕ_W^R is the flux emitted from the wall to the atmosphere outside the combustion chamber. It can be approximately calculated as below:

$$\phi_W^R \simeq \bar{\epsilon} \cdot \sigma T_{wall}^4 \tag{6.8}$$

where $\bar{\epsilon}$ is the average emissivity of the wall, equal to 0.91 for the two ceramic bricks lateral wall and about 0.6 for the two quartz lateral wall and 1.0 for the others. σ is the Stefan number which is equal to $5.670 \cdot 10^{-8} W \cdot m^{-2} \cdot K^{-4}$.

Computation algorithm

Based on Eq. 6.2, in order to determine the real temperature of the wall taking into account the effect of the forced convection, the computation algorithm is defined as below:

1. Calculation is just carried out for the boundary cells located in the four lateral walls of the combustion chamber.

[2]Indeed, this value is a little higher compared with the normal value of the average convection transfer coefficient for the forced convection, our objective is to maximize the value of $\bar{h}$.

2. Dividing the computational domain (the boundary cells) into two groups. One is the cells with high temperature ($T_{cell} > 1500\ K$), for these cells, the initial wall temperature T_{W0} is set to 1200 K .The other is the cells with low temperature ($T_{cell} < 1500\ K$), and the initial wall temperature T_{W0} for these cells is set to 500 K.
3. Setting the initial wall temperature as boundary conditions and running "Rainier" code to calculate the flux ϕ_F^R.
4. Putting the corresponding $\bar{h}$ and this T_{W0} into Eq. 6.2 to see if the equation is satisfied with these parameters. If not, resolving Eq. 6.2 with the flux obtained in step 3 to find another wall temperature T_{Wi}.
5. Using the new temperature T_{Wi} instead of T_{W0} to re-run the step 3 and step 4, until Eq. 6.2 is satisfied, then this T_{Wi} is the actual wall temperature for the cell computed.

Discussion

In fact, with the precedent results $\bar{h}_{max} = 8.64$ for this computation mesh, the value of term $[\bar{h} \cdot (T_W - T_F)]$ (order of magnitude is about $\sim 1.2 \cdot 10^2\ W \cdot m^{-2}$) can be considered to be negligible compared with other term ϕ_F^R (order of magnitude is about $\sim 7 \cdot 10^5\ W \cdot\ m^{-2}$) and ϕ_W^R (order of magnitude is about $\sim 2 \cdot 10^6\ W \cdot m^{-2}$). To conclude, the forced convection term can be neglected in this study. Although with the above algorithm, the actual wall temperature can be obtained. To compare the radiative power with the real wall temperature and the simplified temperature is interesting, it will not be presented in this thesis.

Conclusion

Radiative heat transfer plays an important role in combustion as shown by numerous studies. The difficulties are then how to deal with these physically different phenomena by numerical simulations, taking into account more complex physical characteristics and reducing the modeling cost.

The first part of this thesis is devoted to develop an efficient radiation solver adapted to coupling with a turbulence combustion solver. Additionally, two techniques to improve the code performance have also been presented in this part.

The Monte Carlo statistical method has been chosen here to resolve the radiative transfer equation (RTE). The principal reasons to choose this method is that many complex physical phenomena, such as non-isotropic scattering distributions, complex 3D geometries including obstacles, coupling with turbulent temperature and concentration fields, can be taken into account simultaneously without simplifying assumptions. The only error remaining in this method is the statistical error.

Based on a 3D parallelized radiation solver ASTRE (Approche Statistique des Transferts Radiatifs dans les Ecoulements) developed by Tessé (ONERA & EM2C), three Monte Carlo formulas: Conventional forward Monte Carlo (FM), Emission Reciprocity Method (ERM) and Absorption reciprocity method (ARM) have been compared in the context of combustion processes, applied to a one-dimensional premixed laminar flame propane/air where the gas radiative properties are treated by a correlated-k (CK) model. The reciprocal model, ERM has been found to be more efficient in the isothermal medium than the FM model. Furthermore, compared to the other reciprocal model ARM, ERM requires less computation memory which is an important point for calculation on massively parallel machines. So ERM is considered as the most suitable model for the following computations. Additionally, the influence of some physical or numerical parameters has also been studied here: the influence of the mesh size which shows that a coarser mesh can be applied in zones other than the flame front, and the influence of the thickening factor which shows that when the thickening factor is not equal to 1, a correction factor should be added to perform radiation computations from combustion parameters, otherwise, due to the time limit, this correction has not been carried out in this thesis, it might be performed in a following Ph.D work.

When this radiation solver ASTRE is applied to a complex 3D geometry with a huge number of cells and complex correlated-k (CK) gas radiative properties, the CPU cost and computation memory are not acceptable for coupled calculations. Therefore, two techniques have been developed in this thesis to optimize the performance of ASTRE solver.

The first technique is “Grid merge method”. According to the 1D test, applying a coarser mesh in the homogeneous zone (burnt and unburnt zones) will not change the radiative

results. So a new mesh can be constructed, combing together cells (having similar temperatures and mass fractions of CO_2 and H_2O) after each combustion calculation, and import it in the radiation solver. Two key factors of this technique – maximum number of merged face and temperature criterion have been discussed from a premixed laminar flame case. The precision of the results after merging can be controlled by changing these two factors. Finally, this method is also validated in a 3D swirled gas turbine injector. This validation shows that this technique is very efficient to improve the performance of radiation solver in terms of reducing the CPU usage and memory storage, particularly for computations with large homogeneous area, such as flame in furnaces.

The second technique is "near-range-interaction far-range-interaction" (NIFI) model. Each point in the combustion computation domain has a "near field" (which is composed by the points at a short distance from the target point) and a "far field" (composed by the points at a long distance from the target point). A demonstration carried out on a simple artificial combustion signal in a three dimensional configuration shows that the impact of the "far field" thermodynamic profiles' variation (ex: temperature or mass fraction) on the radiative power of the target point can be neglected, which also means that the impact will be reduced by increasing the distance between the target point and the point in "far field". This characteristic is interesting and useful for our coupled approach between combustion and radiation solvers. Because after each combustion computation, the thermodynamic profiles are changed and will be imported into the radiation solver, if the "far field" variation can be neglected, we need just import the new instantaneous thermodynamic profiles of the "near field" and use the old value for the "far field". In this way, a large number of CPU time and memory storage will be saved.

This technique has then been tested on a three dimensional configuration "$Diedre\_3D$" in this thesis. After several tests, it has been found to work well for hot zones but the results are not very satisfying for cold zones (below 1500 K). On one hand, for hot zones, when the distance is larger than 40 mm (this value may depend on the configuration and should be re-determined for each test case), the field can be considered as "far field" and the error between the precise and the approximate radiative powers (the approximate radiative power is obtained by using the old radiative field in "far field" and the instantaneous radiative field in "near field" instead of using the instantaneous ones for both fields) is lower than 1%. At the same time, it has been shown that about 62% of the optical paths are longer than 40 mm, so applying this model will reduce the computational time efficiently. On the other hand for the cold zone, the error can reach about 10% for a distance about 40 mm, so this model does not work well because the ERM method is difficult to get converged in cold zones.

Even with some numerical techniques to improve ASTRE code performance in terms of CPU time and memory storage, the computation with large mesh still costs too much to be used directly in adapted industrial cases. Therefore, a new Monte Carlo solver "Rainier" has been developed in this work only considering the ERM model, the CK parameters to describe the gas radiative properties and some new algorithms. Firstly, this solver is parallelized by domain. A "master" processor is in charge of transferring the informations among "executing" processors and distributing the tasks and each "executing" processor deals with one part of the computational domain each time. Secondly, it contains a convergence controlling algorithm which can largely improve the numerical performance of the code. Then this code has been validated by the test case "$Diedre\_3D$", giving almost the same

results as that with ASTRE code but taking less CPU time and memory.

Then a comparison between the Monte Carlo Method (Rainier solver) and the Discrete Ordinate Method (DOMASIUM solver) has been performed applied to the three-dimensional configuration "$Diedre\_3D$" (about 3.4 millions tetrahedron cells) in terms of the physical behavior of the flame and the computational aspects (storage requirement, CPU time and parallel efficiency). The AVBP code is used as the LES solver and the mesh for combustion contains about 4.7 millions tetrahedrons cells (there is a connection table between LES and radiation meshes). The results show that these two cases have almost the same radiative power except a small difference near the outlet which probably comes from the boundary conditions leading to an instability. Concerning the computational aspects, Monte Carlo method is estimated to spend less time and takes less memory compared with DOM if both of them take into account an accurate description of the radiation properties. Furthermore, Monte Carlo solver can run well with a machine memory less than 500 MB per processor while DOM needs at least 2GB memory per processor.

In the last part of this thesis, the influence of boundary conditions for the radiative problem has been studied. In a precedent study, in order to simplify the problem, the emissivity of the boundaries has been considered to be unity and wall reflectivity has not been taken into account. Here the actual wall emissivity with has been taken into account to calculate accurately the reflectivity of the boundary. The results show that the impact of the wall emissivity at the outlet of the combustion chamber can be neglected, but the lateral wall emissivity will largely influence the radiative power of the flame in the combustion chamber.

Future works

In this thesis, combustion and radiation solvers have not been fully coupled. The radiation solver (ASTRE or Rainier) only uses the results of the combustion code (AVBP), but radiation source terms and fluxes are not returned to AVBP. So the first future work is to couple them together by the numerical tool CORBA as done in the thesis of Goncalves dos Santos or directly using MPI. Furthermore, as having been studied on 1D tests in this thesis, the correction of radiative transfer should be considered when using the TFLES model. Additionally, the "NIFI" can be improved specially for the application to the cold points and then can be integrated into the coupling code.

Secondly, although Emission Reciprocity Method has been shown to be the most suitable Monte Carlo formulation for coupling from the one dimensional test cases in this thesis, its performance for the cold zone is limited. Improvements should be considered.

Thirdly, changing the algorithm of the merging method might improve its performance and merge much more cells together. For example, beginning merging from one point instead of one edge used in this thesis.

Finally, as mentioned in this thesis, the influence of boundary conditions on radiation is very important and cannot be neglected although taking into account its effect completely and precisely asks for expensive computational sources. Except the lateral wall emissivity and temperature which have been considered in this thesis, other boundary effects are also

interesting to be studied such as taking into account precisely the wall reflection and varying the boundary shape (ex: adding a chimney at the end of the combustion chamber).

Appendix A

Radiative properties model - CK model

A short presentation about radiative properties model - correlated-K (CK) model will be introduced in the part A.1. And the optical path frequency generation method used in the actual version of ASTRE code will be simply presented in the part A.2.

A.1 Correlated-K model

Resolving RTE in the participating media requires an integration over the wave number regarding the gas properties such as absorption, emission, diffusion, etc. Here the specification of the gas absorption coefficient k_ν on function of the wave number (frequency) is important to make the spectral integration. Many spectral models have been developed in recent years (Taine et al. 2003).

Line-by-line model is difficult to be applied directly in 2D and 3D complex systems because of the large calculation time, although it is the most precise method. Then some approximate models have been developed, which can be divided into two groups "band models" which characterize the radiative properties in the discrete spectral bands and "global models" based on a cumulated distribution function of the absorption coefficient over all of the spectrum. Here one kind of "band models" - Correlated-K (CK) model used in this thesis will be detailed. Compared to the "global models", CK model is based on a cumulated distribution function of the absorption coefficient over one band.

In the CK model, the spectrum is divided into sufficiently narrow bands Δk_ν assuming that all the properties are uniform in each band ν (the Planck function, wall properties, etc.) except the absorption coefficient k_ν. Then based on the observation that, over a narrow spectral interval, the radiative transfer is insensitive to the exact placement of spectral lines within the interval, reordering the lines within the interval should not affect the radiative transfer (Siegel and Howell 2002). So a monotonically increasing accumulated function is introduced here to determined the corresponding k_ν.

For an isothermal homogenous medium, defining a probability distribution function $f(k)$ and a cumulated distribution function $g(k)$ depending on the absorption coefficient k_ν over a spectral interval Δk_ν (the center of this interval is ν_0 and its width is $\Delta\nu$). These two

functions can be presented as below:

$$f(k) = \frac{1}{\Delta\nu} \int_{\Delta\nu/k<k_\nu<k+dk} d\nu \tag{A.1}$$

$$g(k) = \frac{1}{\Delta\nu} \int_{\Delta\nu/k_\nu<k} d\nu = \int_0^k f(k\prime)dk\prime \tag{A.2}$$

where $dg = f(k)dk$ represents the probability that k_ν is contained between k and k + dk over $\Delta\nu$. Then all of the average parameters depending on the frequency over $\Delta\nu$ can be written as function of the k or g. For example, the average transmissivity of a column with length l is:

$$\bar{\tau'_\nu}^{\Delta\nu} = \frac{1}{\Delta\nu} \int_{\nu_0-\Delta\nu/2}^{\nu_0+\Delta\nu/2} \tau'_\nu d\nu = \int_0^\infty \tau'_\nu(k) f(k) dk \tag{A.3}$$

Then introducing a monotonically increasing function $k(g)$, the reciprocal function of $g(k)$, and it represents the reordered spectrum on increasing values in function of the dimensionless pseudo-wave number g:

$$\bar{\tau'_\nu}^{\Delta\nu} = \int_0^1 \tau'_\nu[k(g)]dg \tag{A.4}$$

Using the expression of $\bar{\tau'_\nu}^{\Delta\nu}$, the radiation intensity or the flux emitted by homogeneous and isothermal column can be presented by the same way with the assumption that $L^\circ_\nu(T)$ is uniform at ν over the interval $\Delta\nu$.

Generally, with the monotonically increasing function $k(g)$, each function averaged in the interval $\Delta\nu$ (such as $\bar{\tau'_\nu}^{\Delta\nu}$ or $\bar{L'_\nu}^{\Delta\nu}$) can be numerically obtained by using a quadrature of N points ($N \sim 10$) instead of the thousands points needed by the integration of equation A.3.

$$\bar{\tau'_\nu}^{\Delta\nu} = \int_0^\infty \exp(-k_\nu l) f(k) dk = \sum_{j=1}^{7} \omega_j \exp\left(-\sum_{m=1}^{N} k_{mj} l_m\right) \tag{A.5}$$

where the transmissivity is averaged over the interval $\Delta\nu$ discretized into N isothermal and homogeneous elements m of length l_m and a seven-point quadrature is used here. ω_j are the weights associated with the different quadrature points. k_{mj} are the pseudo-absorption coefficients given for each element m. The details about the determination of k_{mj} is presented in Soufiani and Taine (2007).

The parameters of the CK model used here are generated for the temperature range between 300 and 2500 K. And the useful wave number range ($150 - 9200\ cm^{-1}$) is divided into 44 spectral bands for H_2O and CO_2 in only 17 of these bands. Gauss quadratures with 7 points are used for H_2O and CO_2 respectively in their absorption bands, i.e. 49 quadrature points are used in the 17 overlapping bands. Therefore 1022 pseudo-spectral points have to be taken into account here.

A.2 Frequency generation methods

In the actual version of ASTRE solver, the spectral bands weights are determined according to the emission energy of the cell calculated. This method is detailed below:

1. Calculation applied to cell i ($i = 1$, nmail, where nmail is the total number of the cells in the computational domain).
2. The temperature of cell i is used to calculate the parameters which dedicate to the frequency generation, ex: $L^0_\nu(T_i)$.
3. Determination of the spectral bands weights according to the emission energy of cell i. For each small spectral band "i_b", the energy emitted can be written as:

$$P_e(i_b) = k_\nu(i_b) \cdot L^0_\nu(T_i) \cdot \Delta\nu(i_b) \cdot \omega_{gauss}(i_b) \tag{A.6}$$

where ω_{gauss} is the weight associated with the quadrature points, and the total energy emitted of all the small spectral band "i_b" can be written as:

$$P_{eg} = \sum_{i_b} P_e(i_b) \tag{A.7}$$

Then the spectral band weight can be presented as:

$$\omega'(i_b) = P_e(i_b)/P_{eg} \tag{A.8}$$

According to the principe of CK model, this spectral band weight $\omega'(i_b)$ is reordered as a decreasing function $\omega(i_b)$. Then calculating the cumulated spectral band weight as:

$$\omega_g(i_b) = \sum_{m=1}^{i_b} \omega(i_b) \tag{A.9}$$

4. This cumulated spectral band weight ω_g will be used to choose the spectral band randomly in the following computation: a random value $\omega_g \in [0, 1]$ is generated, and the corresponding small spectral band i_b is determined, the absorption $k_\nu(i_b)$ is then fixed.

Of course, the spectral band weight depends on the local emission which is rather limited for the cold zone, then the probability of this random value locates in the suitable interval is small, that is why it does not converge quickly for the volumes with low temperature.

References

Adams, B. and P. Smith (1995). Modeling effects of soot and turbulence-radiation coupling on radiative transfer in turbulent gaseous combustion. *Combustion Science and technology 109*, 121–140.

Barrere, M. and R. Prud'homme (1973). *Equations fondamentales de l'aerothermochimie*. Paris: Masson.

Butler, T. and P. O'Rourke (1977). A numerical method for two-dimensional unsteady reacting flows. *Sixteenth Symposium (International) on Combustion*, 1503–1515.

Cherkaoui.M, Dufresne.JL, Fournier.R, Grandpeix.JY, and Lahellec.A (1996, May). Monte carlo simulation of radiation in gases with a narrow-band model and a net-exchange formulation. *Journal of heat transfer-transactions of the ASME 118*, 401–407.

Cherkaoui.M, Dufresne.JL, Fournier.R, Grandpeix.JY, and Lahellec.A (1998). Radiative net exchange formulation within one-dimensional gas enclosures with reflective surfaces. *Journal of heat transfer-transactions of the ASME 120*, 275–278.

Coelho, P. (2007). Numerical simulation of the interaction between turbulence and radiation in reactive flows. *Progress in Energy and Combustion Science 33*, 311–383.

Coelho, P., O. Terrling, and D. Roekaerts (2003). Spectral radiative effects and turbulence radiation interaction in a non-luminous turbulent jet diffusion flame. *Combustion and Flame 133(1-2)*, 75–91.

Colin, O., F. Ducros, D. Veynante, and T. Poinsot (2000). A thickened flame model for large eddy simulations of turbulent premixed combustion. *Physics of Fluids A12(7)*, 1843–1863.

Colin, O. and M. Rudgyard (2000). Development of high-order taylor-galerkin schemes for les. *Journal of Computational Physics 162*(2), 338–371.

Daguse, T. (1996). *Effets du rayonnement thermique sur la structure de flammes laminaires de diffusion ou de prémélangé en phase gazeuse*. Ph. D. thesis, Ecole Central Paris, Grande voie des vignes, Chatenay-Malabry, France.

De Lataillade, A. (2001). *Modélisation détaillée des transferts radiatifs et couplage avec la cinétique chimique dans des systèmes en combustion*. Ph. D. thesis, Université Paul Sabatier, Toulouse, France.

Desjardin, P. E. and S. H. Frankel (1999). Two-dimensional large eddy simulation of soot formation in the near-field of a strongly radiating nonpremixed acetylene-air turbulent jet flame. *Combustion and Flame 119*(1-2), 121–132.

Dupoirieux, F., L. Tesse, S. Avila, and J. Taine (2006). An optimized reciprocity monte carlo method for the calculation of radiative transfer in media of various optical thickness. *International Journal of Heat and Mass Transfer 49*, 1310–1319.

Farmer, J. and J. Howell (1998). Monte carlo strategies for radiative transfer in participating media. *Advances in Heat Transfer 31*, 1–97.

Galley, D. (2006). Etude de la stabilisation de flammes turbulentes prevaporisees par premelangees paurvres. *Ph.D Dissertation*.

Giordano, P. and D. Lentini (2001). Combustion-radiation-trubulence interaction modeling in absorbing/emitting nonpremixed flames. *Combustion Science and technology 172*, 1–22.

Goncalves Dos Santos, R. (2008). *Large Eddy Simulations of Turbulent Combustion Including Radiative Heat Transfer*. Ph. D. thesis.

Goncalves Dos Santos, R., M. Lecanu, S. Ducruix, O. Gicquel, E. Iacona, and D. Veynante (2008). Coupled large eddy simulations of turbulent combustion and radiative heat transfer. *Combustion and Flame 152*, 387–400.

Gore, J. P. and G. Faeth (1988). Structure and radiation properties of luminous turbulent acetylene/air diffusion flames. *J. Heat Transfer 110*, 173–181.

Gore, J. P., S. Jeng, and G. Faeth (1987). Spectral and total radiation properties of turbulent carbon monoxide/air diffusion flames. *J. AIAA 25*, 339–345.

Hall, R. and A. Vranos (1994). Efficient calculations of gas radiation from turbulent flames. *International Journal of Heat and Mass Transfer 37*, 2745–2750.

Henning, M. and S. Vinoski (1999). *Advanced CORBA programming with C++*. Addison-Wesley.

Hirsch, C. (1989). *Numerical Computation of Internal and External Flows*. Wiley.

Iacona, E. (2000). *Application de l'interférométrie holographique à l'étude de transferts thermiques couplés dans un gaz au sein d'une cavité*. Ph. D. thesis, Ecole Central Paris.

Iacona, E., O. Penanhoat, P. Picot, O. Guignard, and J. Taine (2002). Radiation transfer modeling by a ray-tracing method and a ck or k approach. In Elsevier (Ed.), *12th Int. Heat Transfer Conference*, Volume 1, pp. 657–662.

Jones, W. P. and M. C. Paul (2005). Combination of dom with les in a gas turbine combustor. *International Journal of Engineering Science 43*(5-6), 379–397.

Joseph, D. (2004). Modelisation des transferts radiatifs en combustion par la methode des ordonnees discretes sur des maillages non-structures tridiensionanels. *Ph.D Dissertation, Institut National Polytechnique de Toulouse*.

Joseph, D., P. Coelho, B. Cuenot, and M. El Hafi (2003). Application of the discrete ordinates method to grey media in complex geometries using unstructured meshes. *In Eurotherm73 on Computational Thermal Radiation in Participating Media 11*, 97–106.

Ju, Y., H. Matsumi, K. Takita, and G. Masuya (1999). Combined effects of radiation, flame curvature, and stretch on the extinction and bifurcations of cylindrical ch4/air premixed flame. *Combustion and Flame 116*, 580–592.

Kaplan, C., S. Baek, E. Oran, and J. Ellzey (1994). Dynamics of a strongly radiating unsteady ethylene jet diffusion flame. *Combustion and Flame 96*, 1–21.

Kee, R., G. Dixon-Lewis, J. Warnatz, Coltrin, and Miller (1986). A fortran computer code package for the evaluation of gas-phase multicomponent transport properties. SANDIA Report prepared by SANDIA national laboratory, USA.

Knikker, R., D. Veynante, and C. Meneveau (2002). A priori testing of a similarity model for large eddysimulations of turbulent premixed combustion. *Proceedings of the Combustion Institute 29*(2), 2105–2111.

Knikker, R., D. Veynante, and C. Meneveau (2004). A dynamic flame surface density model for large eddy simulation of turbulent premixed combustion. *PHYSICS OF FLUIDS 16*, 91–94.

Knikker, R., D. Veynante, J. Rolon, and C. Meneveau (2000). Planar lase-induced fluorescence in a turbulent premixed flame to analyze large eddy simulation models. *In 10th International Symposium on Applications of Laser techniques to Fluid Mechanics, Lisbon, Portugal*.

Kobiyama, M. (1989). Reduction of computing time and improvement of convergence stability of the monte carlo method applied to radiative heat transfer with variable properties. *Journal of heat transfer-transactions of the ASME 111*, 135–140.

Kounalakis, M., J. P. Gore, and G. Faeth (1988). Turbulence/radiation interactions in nonpremixed hydrogen/air flames. In T. C. Institute (Ed.), *Twenty-second Symposium on combustion*, pp. 1281–1290.

Kuo, K. (1986). *Principles of Combustion*. New York: John Wiley.

Lataillade, A. D., J. Dufresne, M. E. Hafi, V. Eymet, and R. Fournier (2002). A net-exchange monte carlo approach to radiation in optically thick systems. *Journal of Quantitative Spectroscopy and Radiative Transfer 74*(5), 563–584.

Lecanu, M. (2005). *Couplage multi-physique combustion turbulente - rayonnement - cinetique chimique*. Ph. D. thesis, Ecole Central Paris.

L'Ecuyer, P. (1999). Good parameter sets for combined multiple recuresive random number generators (available from http://www.iro.umontreal.ca/lecuyer/papers.html). *Oper.Res. 47*, 159–164.

Legier, J., D. Veynante, and T. Poinsot (2000). Dynamically thickened flame les model for premixed and non-premixed turbulent combustion. *Proceedings of the summer program, center of turbulence research*.

Li, G. and M. Modest (2003). Importance of turbulence radiation interactions in turbulent diffusion jet flames. *J.Heat Transfer - Transactions of the ASME 125*, 831–838.

Li, G. and M. F. Modest (2002). Application of composition pdf methods in the investigation of turbulence-radiation interactions. *J.Quant. Spectrosc. Radiat. Transfer. 73*, 461–472.

Liu, F., H. Guo, and G. Smallwood (2004). Effects of radiation model on the modeling of a laminar coflow methane/air diffusion flame. *Combustion and Flame 138*, 136–154.

Martin, W. R. and G. C. Pomraning (1990). Monte carlo analysis of the backscattering of radiation from a sphere to a plane. *Journal of Quantitative Spectroscopy and Radiative Transfer 43*(2), 115–126.

Maruyama, S. and T. Aihara (1997). Radiation heat transfer of arbitrary three-dimensional absorbing,emitting and scattering media and specular and diffuse surfaces. *Journal of heat transfer-transactions of the ASME 119*, 129–136.

Mazumder, S. and M. F. Modest (1999). A probability density functions approach to modeling turbulence-radiation interactions in nonluminous flames. *J. Heat Transfer 42*, 971–991.

Metropolis, Nicholas, and Ulam (1949). The monte carlo method. *J.Am.Statistical Assoc. 44*(247), 335–341.

Modest, M. F. (2003). *Radiative heat transfer* (2nd ed.). New York: Academic Press.

Poinsot, T. (1996). Using direct numerical simulations to understand premixed turbulent combustion. In *In Twenty-sixth Symposium (International) on Combustion*, pp. 219–232. The combustion Institute.

Poinsot, T. and S. Lele (1992). Boundary conditions for direct simulations of compressible viscous flows. *Journal of Computational Physics 101*, 104–129.

Poinsot, T., A. Trouve, and S. Candel (1996). Applications of direct simulations of premixed turbulent combustion. *Progress in Energy and Combustion Science 21*, 531–

576.

Poinsot, T. and D. Veynante (2005). *Theoretical and Numerical Combustion* (2nd ed.). Philadelphia USA: R.T.Edwards Inc.

Rivière, P., A. Soufiani, and J. Taine (1992). Correlated-k and fictitious gas methods for h2o near 2.7 [mu]m. *Journal of Quantitative Spectroscopy and Radiative Transfer 48*(2), 187–203.

Schmitt, P. (2005). *Simulation aux grandes echelles de la combustion etagee dans les turbines a gaz et son interaction stabilite-polluants-termique*. Ph. D. thesis, Institut National Polytechnique de Toulouse.

Schoenfeld, T. (2008). The avbp handbook. *http://www.cerfacs.fr/cfd/avbp.html*.

Selle, L., G. Lartigue, T. Poinsot, R. Koch, K. U. Schildmacher, W. Krebs, B. Prade, P. Kaufmann, and D. Veynante (2004). Compressible large eddy simulation of turbulent combustion in complex geometry on unstructured meshes. *Combustion and Flame 137*(4), 489–505.

Shamsundar, N., E. M. Sparrow, and R. P. Heinisch (1973). Monte carlo radiation solutions–effect of energy partitioning and number of rays. *International Journal of Heat and Mass Transfer 16*(3), 690–694.

Siegel, R. and J. Howell (1981). *Thermal radiation heat transfer*. USA: Hemisphere.

Siegel, R. and J. Howell (2002). *Thermal radiation heat transfer*. New York: Taylor and Francis.

Siegel, R. and G. Tate (1936). Heat transfer and pressure drops of liquids in tubes. *Ind. Eng. Chem. 28*, 1429–1436.

Sivathanu, Y. R. and J. P. Gore (1993). A discrete probability function method for the equation of radiative transfer. *Journal of Quantitative Spectroscopy and Radiative Transfer 49*(3), 269–280.

Sivathanu, Y. R. and J. P. Gore (1994). Coupled radiation and soot kinetics calculations in laminar acetylene/air diffusion flames. *Combustion and Flame 97*, 161–172.

Soufiani, A. and J. Taine (1997). High temperature gas radiatie property parameters of statistical narrow-band model for h2o, co2 and co and correlated-k model for h2o and co2. *International Journal of Heat and Mass Transfer 40*, 987–991.

Soufiani, A. and J. Taine (2007, April). High temperature statistical narrow-band parameters for h2o, co2 and co and correlated-k parameters for h2o and co2. Technical report, EM2C Laboratory, Ecole Centrale Paris.

Surzhikov, S. and J. Howell (1998). Monte carlo simulation of radiation in scattering volumes with line structure. *Journal of thermophysics and heat transfer 12*, 278–281.

Taine, J., E. Iacona, and Petit (2003). *Transferts Thermiques* (3 ed.). France: DUNOD.

Tesse, L. (2001). *Modelisation des transferts radiatifs dans les flammes turbulentes par une methode de Monte Carlo*. Ph. D. thesis, Ecole Central Paris, Grande voie des vignes, Chatenay-Malabry, France.

Tesse, L., F. Dupoirieux, and J. Taine (2004). Monte carlo modeling of radiative transfer in a turbulent sooty flame. *International Journal of Heat and Mass Transfer*, 555–572.

Tesse, L., F. Dupoirieux, B. Zamuner, and J. Taine (2002). Radiative transfer in real gases using reciprocal and forward monte carlo methods and a correlated-k approch. *International Journal of Heat and Mass Transfer*.

Vervisch, L. and T. Poinsot (1998). Direct numerical simulation of non-premixed turbulent flame. *Annu. Rev. Fluid Mech. 30*, 655–692.

Walters, D. V. and R. O. Buckius (1992). Rigorous development for radiation heat transfer in nonhomogeneous absorbing, emitting and scattering media. *International Jour-*

nal of Heat and Mass Transfer 35(12), 3323–3333.

Walters, D. V. and R. O. Buckius (1994). Monte carlo methods for radiative heat transfer in scattering media. *Annual Review of Heat Transfer 5*, 131–176.

Williams, F. (1985). *Combustion Theory* (2nd ed.). Addison-Wesley.

Wu, Y., D. C. Haworth, M. F. Modest, and B. Cuenot (2005). Direct numerical simulation of turbulence/radiation interaction in premixed combustion systems. *Proceedings of the Combustion Institute 30*(1), 639–646.

Yang, W., H. Taniguchi, and K. Kudo (1995). Radiative heat transfer by the monte carlo method. *Advances in Heat Transfer 27*, 1–215.

Yoo, C., H. Im, Y. Wang, and A. Trouve (2005). Interaction of turbulence, chemistry, and radiation in strained nonpremixed flames. *Journal of physics conference series 16*, 91–100.

Zhu, X. and J. P. Gore (2005). Radiation effects on combustion and pollutant emissions of high-pressure opposed flow methan/air diffusion flames. *Combustion and Flame 141*, 118–130.